

# REPORT DOCUMENTATION PAGE

Public reporting burden for this collection of information is estimated to average 1 hour per response, including the time for reviewing data needed, and completing and reviewing this collection of information. Send comments regarding this burden estimate or any other aspect of this burden to Department of Defense, Washington Headquarters Services, Directorate for Information Operations and Reports (0704-4302). Respondents should be aware that notwithstanding any other provision of law, no person shall be subject to any penalty for failing to comply with a collection of information that does not have a valid OMB control number. **PLEASE DO NOT RETURN YOUR FORM TO THE ABOVE ADDRESS.**

<b>1. REPORT DATE (DD-MM-YYYY)</b> 07/31/06		<b>2. REPORT TYPE</b> Final Report		<b>3. DATES COVERED (From - To)</b> 09-01-05 to 04-30-06	
<b>4. TITLE AND SUBTITLE</b> New Generation Materials & Structures for Nanophotonics & Nanoelectronics				<b>5a. CONTRACT NUMBER</b>	
				<b>5b. GRANT NUMBER</b> F49620-01-1-0358	
				<b>5c. PROGRAM ELEMENT NUMBER</b>	
<b>6. AUTHOR(S)</b> Paras N. Prasad				<b>5d. PROJECT NUMBER</b>	
				<b>5e. TASK NUMBER</b>	
				<b>5f. WORK UNIT NUMBER</b>	
<b>7. PERFORMING ORGANIZATION NAME(S) AND ADDRESS(ES)</b>  University at Buffalo Natural Sciences Complex North Campus Amherst, NY 14260				<b>8. PERFORMING ORGANIZATION REPORT NUMBER</b>	
<b>9. SPONSORING / MONITORING AGENCY NAME(S) AND ADDRESS(ES)</b> AFOSR/NL 875 N RANDOLPH STREET SUITE 325, RM 3112 ARLINGTON VA 22203-1768				<b>10. SPONSOR/MONITOR'S ACRONYM(S)</b>	
				<b>11. SPONSOR/MONITOR'S REPORT NUMBER(S)</b>	
<b>12. DISTRIBUTION / AVAILABILITY STATEMENT</b>  Approve for Public Release: Distribution Unlimited					
<b>13. SUPPLEMENTARY NOTES</b>					
<b>14. ABSTRACT:</b> This DURINT project produced high impact technical accomplishments. The notable accomplishments include building (i) new nanostructures, (ii) study of optoelectronic and magnetic properties, and (iii) fabrication of polymer based non-linear based photonic crystals and photonic circuitry, and (iv) fabrication of photodetector as well as diffraction grating devices. On the preparation front, a modular colloidal route was devised to produce nano-heterostructures by integrating plasmonic (Au), magnetic (Fe <sub>3</sub> O <sub>4</sub> ) and semiconducting (PbS or PbSe) moieties into a single platform. The properties of each component within the hybrids were strongly modulated by the conjugating component(s), due to the coherent interfaces between them. New ferromagnetic (low temperature) InMnP nanoparticles were synthesized. Far IR and Raman spectroscopies revealed additional vibrational features related to Mn-P vibrations that could help locate the Mn sites in the crystal. For photodetector devices, an organic/inorganic polymeric nanocomposite consisting of poly-N-vinyl carbazole(PVK), lead selenide quantum dots(QDs) as photosensitizer and organic semiconductor pentacene as a conductivity booster, is constructed. The device exhibits dramatic enhancement of infrared photocurrent. Another device consisting of PVK, PbSe QDs conjugated to carbon nanotube also shows a significantly enhanced photodetector efficiency. In further work on the device front, we demonstrated through holographic photopolymerization, the formation of 3-D photonic crystal of exceptionally long range order and high efficiency 1-D reflection gratings. Additionally, we have employed two-photon polymerization technique for defect engineering in 3-D photonic crystals. Moreover, a dramatic increase in third harmonic efficiency was achieved. In addition to a large number of publications, the project also produced a number of inventions.					
<b>15. SUBJECT TERMS</b> Hybrid nanocomposite dots, Two-photon dendrimers, Photofractive materials, Photonic crystals, Magnetic nanoparticles.					
<b>16. SECURITY CLASSIFICATION OF:</b>			<b>17. LIMITATION OF ABSTRACT</b>	<b>18. NUMBER OF PAGES</b>	<b>19a. NAME OF RESPONSIBLE PERSON</b>
<b>a. REPORT</b>	<b>b. ABSTRACT</b>	<b>c. THIS PAGE</b>			<b>19b. TELEPHONE NUMBER (include area code)</b>
			1		

**Final Report**  
**04/30/06**

Prime Contract : F49620-01-1-0358  
Subcontract : 21169-1-1016565

**New Generation Materials & Structures for**  
**Nanophotonics & Nanoelectronics**

Submitted by: Professor Paras N. Prasad  
Institute for Lasers, Photonics and Biophotonics  
State University of New York at Buffalo

**20061016208**

**Objectives:** (List the objectives of the research effort. This may be omitted if there has been no change. State new or revised objectives if they have changed and why.) No change to the objectives.

**Status of effort:** (Brief, under 200 words, of progress towards achieving the research objectives.)

This DURINT project produced high impact technical accomplishments. The notable accomplishments include building (i) new nanostructures, (ii) study of optoelectronic and magnetic properties, and (iii) fabrication of polymer based non-linear based photonic crystals and photonic circuitry, and (iv) fabrication of photodetector as well as diffraction grating devices. A colloidal route was devised to produce nano-heterostructures by integrating plasmonic (Au), magnetic ( $\text{Fe}_3\text{O}_4$ ) and semiconducting (PbS or PbSe) moieties into a single platform. New ferromagnetic (low temperature) InMnP nanoparticles were synthesized and characterized by far IR and Raman spectroscopies. For photodetector devices, an organic/inorganic polymeric nanocomposite consisting of poly-N-vinyl carbazole (PVK), lead selenide quantum dots (QDs) as photosensitizer and organic semiconductor pentacene as a conductivity booster, is constructed. The device exhibits dramatic enhancement of infrared photocurrent. Another device consisting of PVK, PbSe QDs conjugated to carbon nanotube also shows a significantly enhanced photodetector efficiency. In further work on the device front, we demonstrated through holographic photopolymerization, the formation of 3-D photonic crystal of exceptionally long range order and high efficiency 1-D reflection gratings. Additionally, we have employed two-photon polymerization technique for defect engineering in 3-D photonic crystals. Moreover, a dramatic increase in third harmonic efficiency was achieved. In addition to a large number of publications, the project also produced a number of inventions.

## **1. Objectives**

This project has the goal of providing the military with a hybrid technology involving integration of molecular electronics, nanoelectronics, nanophotonics and nano-optoelectronics. It is a materials development program to enable appropriate technology development. The objective of the proposed research is a systematic design, at both molecular and nanoscopic levels, leading to generation-after-next materials and structures, in which electron or photon-mediated processes can be judiciously controlled, not only to enhance the performance of a particular device but also to lead to new capabilities. The objectives for materials development involves: (i) developing novel molecular and supramolecular structures that will allow a judicious tailoring of electronic and photonic interactions and dynamics leading to control of channels for electron and photon (excitation) transfer, and (ii) developing new self-assembly, field driven assembly and processing techniques to enable production of periodic, aperiodic and engineering architectures on the nanoscale, which can lead to co-operative amplification, synergism, new manifestations and broad spectral responses. In this program, we have emphasized the materials development aspects of nanotechnology by pre-tailoring the optoelectronic properties materials for futuristic applications.

## **2. Approaches**

The various tasks of the project require a multidisciplinary approach involving modeling, synthesis, process and characterization. The necessary comprehensive approach involves the following:

- Rational design of molecular structure and precursors based on structure-property relationships.
- Novel chemical synthetic approach using solution chemistry to produce molecular, dendritic and inorganic semiconductor nanostructures.
- New processing schemes to produce inorganic/organic hybrid nanocomposites with direct interfaces.
- Processing of polymer based self-assembled ordered nanostructures and photonic crystals for nonlinear optical functions.
- Use of bioinspired novel supramolecular structures as templates for periodic or aperiodic self-assembling of electronic, photonic and magnetic units.
- Characterization of nanostructures by TEM, SEM, AFM and confocal microscopy as well as by various linear and nonlinear optical spectroscopies.
- Characterization of various electronic, photonic and magnetic functions.
- Interactive feedback between design, synthesis processing and characterization.

Our approach also places a very strong emphasis on utilizing the expertise of various team members in a complementary way. A strong collaboration with the DoD laboratory and interactive feedback with them ensures that the goals of the project are fully compatible with the needs of the military.

## **Accomplishments:**

Significant accomplishments were made under this DURINT program in the tasks originally proposed. A major emphasis was placed on working as a highly collaborative team and interacting with the Air Force Laboratory. Many major accomplishments of this project would not have been realized without this collaborative effort. Constant communication, exchange of information, and interactive feedback were maintained through a number of means including exchange visits by researchers, focused review workshops and organization of symposia at professional societies.

A large number of publications and invited lectures by the DURINT team exemplify the great deal of research accomplished under this program and its broad impact on science and technology, internationally. In addition, a number of patents resulting from these accomplishments have been filed.

### **I. Two-Photon Energy Harvesting Dendritic Systems**

*Collaboration: P. N. Prasad, University at Buffalo;*

*J.M.J. Fréchet, UC Berkeley;*

*L.-S. Tan, AFRL, Dayton*

Two-photon absorption excited intramolecular energy transfer and light harvesting effects are demonstrated for the first time in two types of Dendritic Systems. These systems contain both an antenna structure that strongly absorb two-photon energy at ~800 nm in the near-IR region, and transfer energy efficiently to a core moiety where the energy can be more effectively utilized for performing significantly enhanced photonic function such as lasing or photochemistry. These systems are bio-inspired from nature's photosynthetic systems utilizing chlorophyll antenna, except that our system utilizing nonlinear two-photon absorption that permits photons in the near-IR to IR to be absorbed and transforms efficiently into excitation normally created by a higher energy photon in the visible. In our dendritic system the core moiety emits efficiently at ~590 nm. The two-photon energy absorbed by the antenna structure is resonantly transferred to the core, where the emission intensity of the latter is enhanced by 8, 20, and 34 times for the three dendritic systems, respectively. This type of novel dendrimer structures and intramolecular energy transfer mechanisms can be useful for multi-photon pumped frequency-upconversion lasing, as well as for highly-sensitive optical sensors working at IR spectral ranges.

Another dendritic system harvesting two-photon excitation for photoactivation at the core involves a two-photon chromophore synthesized at AFRL, Dayton (Tan) and a catalytic porphyrin core moiety. The IR photons are strongly absorbed by the two-photon absorbing chromophores, and the energy is efficiently transferred to the porphyrin moiety which generates highly reactive singlet oxygen. This reactive singlet oxygen is very important for a number of useful photo oxidation processes, including the biological applications in photodynamic therapy.

## **II. Band-Gap Engineering and characterization of inorganic quantum dots**

*Collaboration: P. N. Prasad, A. Cartwright, B. Weinstein, B. McCombe and H. Luo,  
University at Buffalo*

### **New Precursor Routes for Quantum Dots:**

Prasad's group has been involved in the development of novel and efficient organic based precursor routes for band gap engineering of quantum dots and core-shell structures, whereby quantum dots absorbing in different spectral range and dispersible in common organic solvents can be produced.

There has been a well focused work on the synthesis of highly luminescent quantum dots using a new precursor route involving a fast reaction of  $\text{In}(\text{Carboxylate})_3$  with  $\text{P}(\text{SiMe}_3)_3$  in octadecene. These reactions are reproducible and result in relatively monodispersed crops (12-13 % relative standard deviation) of quantum dots in as little as 2 hours. This procedure does not need the addition of an external surfactant, because the carboxylate group generated in situ bind on the surface of the nanoparticles. It should be noted that in the conventional route using TOPO as the surfactant, InP quantum dots took up to 6 days to prepare, after which a multi step work-up was required to obtain relatively monodisperse crops.

Along with the preparation of InP quantum dots, we have developed a new method for the preparation of CdSe quantum dots and CdS quantum dots. This method results in high quality particles that are highly monodisperse (less than 8% relative standard deviation). Included in this publication we have also developed a one-pot synthesis of CdSe/CdS quantum dots Core/Shell quantum dots which is completed in less than 3 hours.

A considerable amount of time has been spent on the synthesis of InP/II-VI core/shell quantum dots. We have synthesized InP/CdS, InP/CdSe, InP/ZnS and InP/ZnSe core-shell quantum dots. All of these QDs have been successfully synthesized and characterized by IR, UV-vis, photoluminescence and photoluminescence emission spectroscopy.

### **Highly efficient III-V quantum dots for Imaging:**

Prasad's group has focused on the development faster synthetic routes of highly luminescent quantum dots and their applications. This novel method that uses no externally added surfactant was used for the synthesis of highly monodispersed hydrophilic InP-ZnS nanocrystals and were used as luminescence probes for imaging. Hydrophobic InP-ZnS nanocrystals are prepared by the new method that yields high quality, luminescent core-shell nanocrystals within 6-8 hours of total reaction time. Then by carefully manipulating the surface of these passivated nanocrystals, aqueous dispersions of folate conjugated nanocrystals (folate-QDs) with high photostability are prepared. As an illustration of imaging, we demonstrated, using confocal microscopy,

the receptor mediated delivery of folic acid conjugated quantum dots into folate receptor positive cell lines such as KB cells. These folate-QDs tend to accumulate in

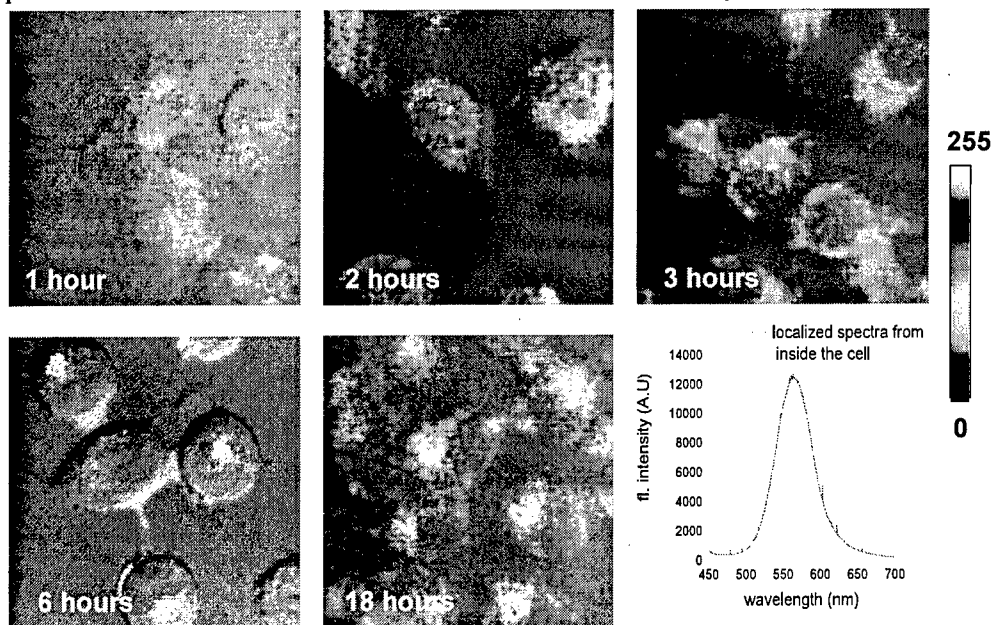


Figure 1. Confocal images showing fluorescence of QD-FA in KB cells and a localized PL emission spectrum. Here green channel shows the transmission images, while the intensity coded (red to white ) channel shows the fluorescence.

multivesicular bodies of KB cells after 6 hours of incubation (Fig. 1). Receptor mediated delivery was confirmed by comparing with the uptake of these particles in folate receptor negative cell lines such as A549. Efficient two-photon excitation of these quantum dot particles was also demonstrated. The use of these InP-ZnS nanoparticles and their

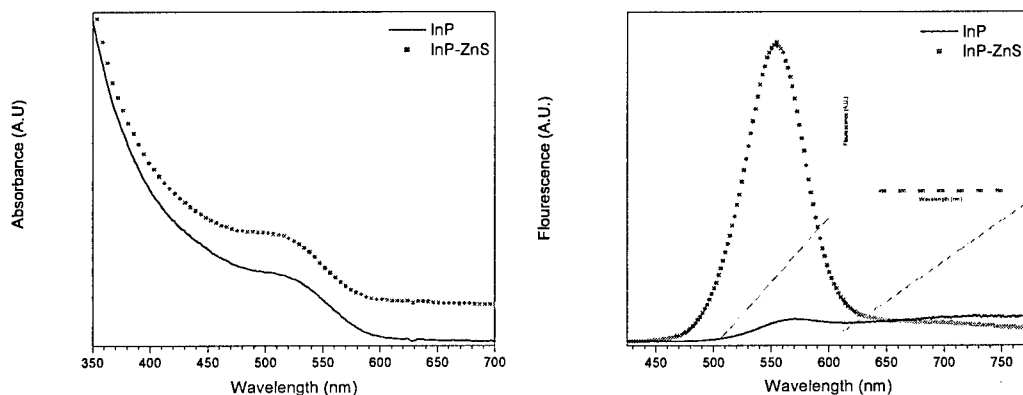


Figure 2. Absorption and emission spectra of  $\text{InP}_{(\text{QD})}$  and  $\text{InP-ZnS}_{(\text{QDs})}$  dispersed in chloroform. The inset in emission spectra, shows the surface state emission from bare InP particles, which is absent in case of ZnS coated core-shell particles.

efficient two-photon excitation can be potentially useful for deep tissue imaging for future in-vivo studies

### Phonon Spectroscopy of Quantum Dots

A collaborative effort with Professors Bruce McCombe and Bernard Weinstein has produced significant progress in understanding the vibrational modes of the InP/II-VI core-shell nanoparticles. This understanding was achieved through a combination of variable temperature IR and Raman measurements and detailed theoretical modeling, making use of a recently published dielectric continuum model. These results allow us to determine the ratio of the radii of the core to the shell, and also in some cases to determine that the chemical processing did not yield just core-shell nanoparticles, but rather a mixture of InP nanoparticles, II-VI nanoparticles and core-shell nanoparticles. A particularly interesting result is an apparent resonant Raman effect that tunes dramatically with temperature in the InP/ZnSe core shell structures. (Fig. 3). At room temperature a very sharp line associated with a ZnSe surface mode ( $\omega_B$ ) is seen; below 100 K this mode disappears and is replaced by two other sharp modes, one associated with the InP core ( $\omega_C$ ) and one with another surface mode in the ZnSe ( $\omega_A$ ). This dramatic behavior, illustrating tunable vibronic couplings to spatially different vibrational modes, is a result of the interesting band structure of the core shell structure with a small valence band offset. These results indicate that the vibronic coupling can be tailored in appropriate core shell structures, and this in turn means that there may be interesting photonic applications.

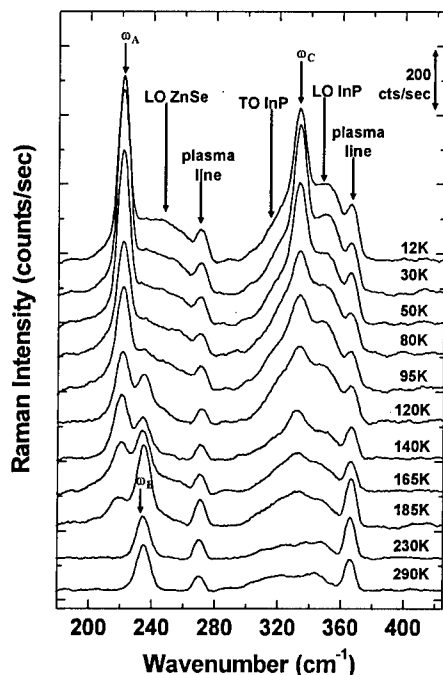


Fig 3. Raman spectra of InP quantum dots



Phonons play an important role in nanophotonics, as they control the dynamics of photon induced processes. We continued analysis of the vibrational modes of the InP/II-VI core-shell nanoparticles determined by IR and Raman studies, and initiated studies of II-VI core shell nanoparticles. These results have allowed us to determine the ratio of the radii of the core to the shell, and also in some cases to determine that the chemical processing did not yield just core-shell nanoparticles, but rather a mixture of InP nanoparticles, II-VI nanoparticles and core-shell nanoparticles.

We have also studied the vibrational modes of II-VI/II-VI core-shell nanoparticles by IR spectroscopy and find good agreement with previous studies. We have investigated the dependence of the absorption strength of these well-characterized core-shell structures on the filling fraction in the CsI matrix. Results show systematic increases in absorption with filling fraction; for a filling fraction of about 6%, the In-P vibrational bands are overabsorbed, demonstrating the possibility of using IR spectroscopy to investigate local Mn-P modes of the interesting ferromagnetic nanoparticle system (InMn)P synthesized by Y. Sahoo of Prasad's group. The Mn-related modes are expected to be much weaker than the In-P modes due to the low concentration (typically a few percent) of Mn replacing In; for filling fractions of 6% or higher, these modes should nevertheless be observable. This could serve as an important characterization tool in understanding the magnetic behavior in this system.

Finally, we have initiated magnet-photoluminescence studies of InSb (a narrow gap semiconductor) nanoparticles produced by D. Lucey of Prasad's group. These nanoparticles luminesce in the IR and are much more amenable to tuning of the emission wavelength by particle size due to the small fundamental energy gap. An example of PL measurements at low temperature is shown in Fig. 4. The main peak appears to be due to the 22 nm nanoparticles, and the low-energy peak is associated with large clusters of nanoparticles giving rise to quasi-bulk emission.

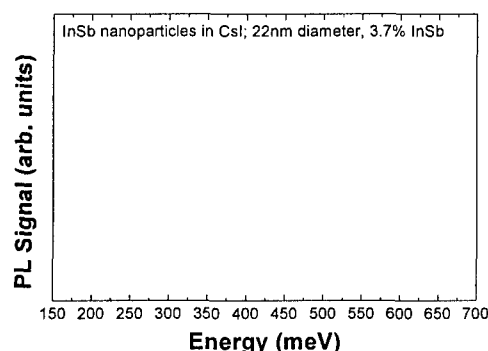


**Figure 4:** PL spectrum at 4.2 K of InSb nanoparticles embedded in a CsI matrix. Data were taken with a BOMEM DA-3 FTIR spectrometer.

### III. Plasmonic Nanoparticles

*Collaboration: P. N. Prasad, M.T. Swihart*

*University at Buffalo*

*Younan Xia, University of Washington*

Metallic nanoparticles and nanostructures form a major thrust area of nanophotonics, called plasmonics. They produce highly confined and significantly enhanced optical responses. We thus placed a significant effort on making multifunctional plasmonic structures

## Plasmonics Nanoparticles

Here our focus is to prepared metallic nanostructures which can be used to enhance photonic response. Gold nanoparticles have been prepared using bifunctional ligands of the type X-R-SH ( $X = -COOH, -OH, -NH_2$ ) so that the surface is terminated with these functionalities. The ligands bind to the gold surface through their thiol ( $-SH$  end). The coverage and binding strength of the surfactant on the gold surface have been investigated using thermogravimetric analysis and FTIR spectroscopy. The nanoparticles appear to have excess surfactants on their surface, but these do not necessarily form a bilayer structure. The surfactant conformation allows enough room for the particles to be bonded to other surfaces, such as those of another nanoparticle, even with some excess surfactant present on their surface.

We synthesized core-shell structures consisting of monodisperse polystyrene latex nanospheres as cores and gold nanoparticles as shells. Use of polystyrene spheres as the core in these structures is advantageous because they are readily available commercially in a wide range of sizes, and with dyes or other molecules doped into them. Gold nanoparticles, ranging in size from 1 to 20 nm, are prepared by reduction of a gold precursor with reducing agents such as sodium citrate, sodium borohydride or tetrakis(hydroxymethyl)phosphonium chloride (THPC). Carboxylate terminated polystyrene spheres are functionalized with 2-aminoethanethiol hydrochloride (AET), which forms a peptide bond with carboxylic acid groups on their surface, resulting in a thiol-terminated surface. Gold nanoparticles then bind to the thiol groups to provide up to about 50% coverage of the surface. These nanoparticles serve as seeds for growth of a continuous gold shell by reduction of additional gold precursor. The shell thickness and the roughness can be controlled by the size of the nanoparticle seeds as well as by the process of their growth into a continuous shell. By variation of the relative sizes of the latex core and the thickness of the gold overlayer, the plasmon resonance of the nanoshell can be tuned to specific wavelengths across the visible and infrared range of the electromagnetic spectrum, for applications ranging from the construction of photonic crystals to biophotonics. The position and width of the plasmon resonance extinction peak are well predicted by extended Mie scattering theory.

### Nanoshells of gold and silver on Dielectric cores:

We present a systematic study of the plasmon resonance absorption spectra of gold nanoshells and silver nanoshells on the surfaces of monodispersed polystyrene microspheres of different sizes as well as of silver nanoshells on free-standing gold nanoparticles. Gold nanoshells were grown on polystyrene microspheres with diameters of 188 and 543 nm. The commercially available, initially carboxylate-terminated polystyrene spheres were reacted with 2-aminoethanethiol hydrochloride (AET) to yield thiol-terminated microspheres whereon preformed gold nanoparticles were anchored and grown further to render a complete shell. Silver nanoshells were grown on polystyrene cores with diameters of 188, 296, and 543 nm. The growth of silver shell required seeding the polystyrene surface first with gold nanoparticles. Reduction of silver nitrate

onto these gold-decorated microspheres resulted in increasing coverage of silver on the polystyrene core. The nanoshells were characterized using transmission electron microscopy (TEM), scanning electron microscopy (SEM) and UV-vis spectroscopy. By varying the core size of the polystyrene particles and the amount of silver reduced onto them, the surface plasmon resonance of the nanoshell could be tuned across the visible and the near-infrared regions of the electromagnetic spectrum. Gold core – silver shell nanoparticles were synthesized by reducing silver nitrate onto free citrate-gold nanoparticles. These core-shell particles formed chain-like structures with a plasmon resonance absorption that could also be tuned across the visible spectrum.

#### **Gold nanorods:**

Seeded growth of gold nanorods(NRs) has been accomplished in a micellar medium. Cetyl trimethylammoniumbromide (CTAB) forms micelles where the growth of rod shaped gold nanoparticles occurs. AgNO<sub>3</sub> is introduced into the growth solution to enhance the population of the NRs. The roles of non ionic surfactants such as Tween and Triton have been examined and ascertained that with their increasing percentages in the growth solution, the length of the NRs increases monotonically to a critical limit, after which it decreases again. The growth pattern of the NRs fits into the soft template model rendered by the mixture of CTAB and non ionic surfactants.

#### **Gold Seeded Semiconductor -Magnetite heterostructures:**

PbSe nanostructures are potentially useful for telecommunication and sensing applications in near IR. While nanoparticles and nanowires of IV-VI semiconductors such as PbSe have been prepared in the past, nanorods of these materials with controlled length and diameter have not previously been reported. Here, PbSe nanorods with controlled lengths and diameters were synthesized using Au and Au-Fe<sub>3</sub>O<sub>4</sub> black-eyed pea-like hybrid nanoparticles as catalytic seeds. PbSe nanostructures with different morphologies (dots, rods and stars) have been prepared by changing the precursor to seed ratio.

### **IV. Silicon Nanoparticles**

*Collaboration: P. N. Prasad, M.T. Swihart  
University at Buffalo*

Nanostructured silicon dispersed in plastics offers another opportunity for hybrid electroluminescent devices. Optically clear and stable dispersions of brightly photoluminescent Si nanoparticles were prepared under the direction of Professor Swihart, by covalent attachment of alkenoic compounds to the particles. Quenching of photoluminescence by ethylamine, diethylamine, triethylamine, pyrazine, and piperazine was investigated. The photoluminescence was quenched by the action of these nitrogenous species, but in some cases could be partially restored by the addition of trifluoroacetic acid. The extent of restoration of photoluminescence, after equilibrium is reached, was independent of the sequence of addition of the amine and the acid. The photoluminescence quenching and recovery are influenced by a combination of basicity, polarity, and steric factors of the quencher molecules. The quenching and subsequent restoration occurs gradually at room temperature and it takes several minutes to reach equilibrium.

## **V. Nanocomposites for efficient optoelectronics and photorefractivity**

*Collaboration: A.N. Cartwright, P.N. Prasad, University at Buffalo;  
M. Durstock, AFRL, Dayton*

Hybrid organic:inorganic materials have emerged as a novel class of electronic and optoelectronic media for a number of potential technological applications, including solar energy conversion, photodetectors, electroluminescent and photorefractives. They offer broadband tunability of the wavelength response, increased photogeneration efficiency and improved charge collection efficiency. We have already shown that semiconductor nanoparticles are efficient photosensitizers for reduced electric field photogeneration in hybrid materials. Now, we have also shown that photoconductive composites obtained by doping of a host polymer with semiconductor nanoparticles exhibit an increase in the effective mobility of charge carriers. This will be of importance for more effective operation of various devices including broadband solar cells. We studied the mobility of holes in a model nanoparticle-sensitized hybrid organic:inorganic system consisting of poly(N-vinylcarbazole) (PVK) doped with quantum dots of cadmium sulfide. We found typical features of the charge carrier transport like strong dependence of the carrier mobility on the field and temperature as well as on sample thickness which is a signature of dispersive transport. However, significant enhancement of the effective carrier mobility is also noticed with the increase of nanoparticle concentration, although it was still well below the percolation limit. A preliminary explanation of this phenomenon assumes an active role played by the nanoparticles in the transport. A simple theoretical model based on time- and mean-free-path dependent mobility was proposed to account for this surprising result. The magnitude of the enhancement is found to be consistent with this model.

In order to produce polymer:quantum-dot nano-composites providing a broad spectral coverage to harvest photons over entire spectral range, we have focused on two areas of synthesis and processing:

- Development of novel and efficient organic based precursor routes for band gap engineering of quantum dots and core-shell structures, whereby quantum dots absorbing in different spectral range and dispersible in common organic solvents can be produced. We have made GaP, InP, silicon, as well as core-shell structures InP/ZnS, InP/CdS, InP/CdSe of different sizes, producing optical absorption and emission over a broad spectral range.
- Processing as nanocomposites in an efficiently hole transporting polymer to create a direct interface between the quantum dots and the polymer for facilitating charge transfer and subsequent migration. For this purpose we are experimenting with different capping organic ligands which can thermally be driven-off from the surface of the quantum dots. Another approach is to use a conjugated structure as the capping agent whereby  $\pi$ -electrons facilitate the charge-transfer and subsequent migration.

Two provisional patents have been filed on the novel synthetic approach to band gap engineering.

### Photoconductivity and Photorefractivity at 1.3 $\mu\text{m}$ Using Quantum Dot: Polymer Nanocomposites:

Due to the relatively large Bohr radius (20 nm) of the exciton, PbS quantum dots offer unique access to the regime of extreme quantum confinement and this property makes them a suitable choice to photosensitize photorefractive (PR) polymeric composites at the technologically important wavelengths of 1.31 and 1.55  $\mu\text{m}$ . PbS nanocrystals were produced by reacting the precursors via a hot colloidal synthetic route. High quality, uniform sized nanocrystals ( $\sim 6\text{-}8\text{ nm}$ ) with highly crystalline phases were obtained (Fig 5).

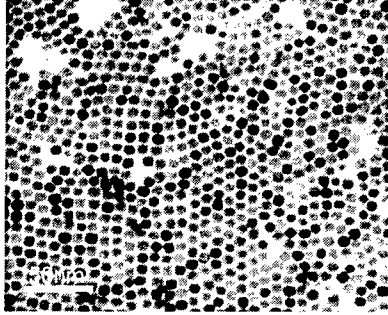


Fig 5. TEM image of the PbS nanocrystals

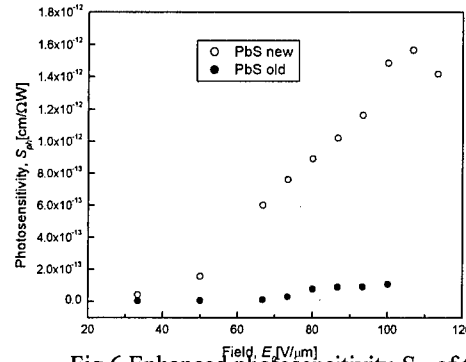


Fig 6. Enhanced photosensitivity  $S_{ph}$  of the nanocrystalline PbS compared to previously reported samples

The photorefractive samples of composition PVK:ECZ:DEANST:PbS (48:15:35:2 wt %) showed greatly enhanced photoconductivity (almost an order of magnitude) at the operational wavelength of 1.34  $\mu\text{m}$  compared to previous results (Fig 3). Pronounced PR two-beam coupling effect at the operation wavelength was observed, leading to very high optical gains (Fig. 4). A response time faster than other hybrid photorefractive nanocomposites is also observed.

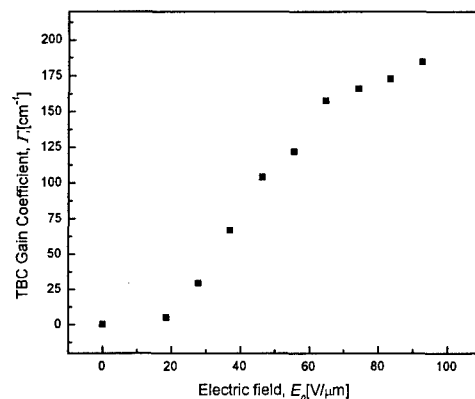


Fig 7. Electric field dependence of the TBC gain coefficient  $\Gamma$  in the PVK:ECZ:DEANST:PbS nanocomposite at 1.34  $\mu\text{m}$ . The highest gain recorded was 184.5  $\text{cm}^{-1}$  at 92.6  $\text{V}/\mu\text{m}$ .

### Photoconductivity and Photorefractivity at 1.55 $\mu\text{m}$ Using Quantum Dot: Polymer Nanocomposites:

#### a. Excellent photoconductivity and narrow luminescence in solution-processed hybrid organic:inorganic nanocomposites at optical communication wavelengths

The photo-response of a polymer composite was extended to the 1.55  $\mu\text{m}$  telecommunications band. Size tunable absorption of the semiconductor quantum dots enabled us to successfully sensitize the hybrid devices and tune their spectral response across the infrared range between 800 nm and 2  $\mu\text{m}$ . The nanocomposites are photoactive at infrared wavelengths with narrow emission bands, tunable with the quantum dot sizes. The photoluminescence spans a wide spectral range in the infrared (Figure 8). Efficient harvesting of infrared photo-generated carriers led to high photocurrents. In particular, we observe for the first time, high photoconductive internal quantum efficiency (among the highest reported so far in this spectral range) in these hybrid devices at the technologically important wavelength of 1.55  $\mu\text{m}$  (Figure 9), achievable by low-power continuous-wave illumination, without the necessity of lock-in techniques.

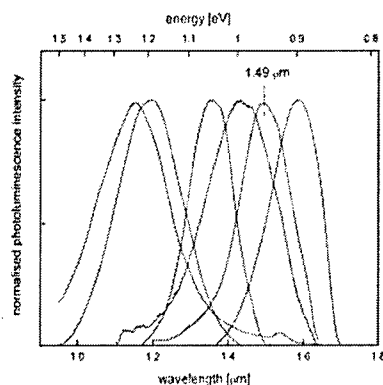


Figure 8. Normalized room-temperature photoluminescence spectra of a series of polymer-NC composites, demonstrating size-tunable emission in the IR.

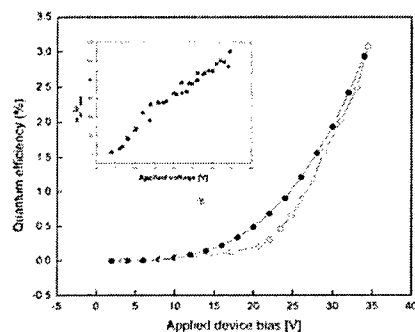


Figure 9. Main Panel: photoconductive quantum efficiency as a function of device bias at excitation wavelengths of 1.34  $\mu\text{m}$  (open circles) and 1.55  $\mu\text{m}$  (filled circles). Inset: the ratio of photo- to dark conductivity for devices as a function of applied voltage, at excitation wavelengths of 1.34  $\mu\text{m}$  (circles) and 1.55  $\mu\text{m}$  (triangles).

b. Photorefractive response of a polymer device to 1.55 $\mu\text{m}$  optical communication wavelength: an organic:inorganic nanocomposite

Using colloiddally-fabricated PbSe quantum dots photosensitization of a polymeric nanocomposite at the optical communication wavelength of 1.55 $\mu\text{m}$  is achieved. Efficient generation of infrared photons lead to high photoconductivity and a significant figure of net gain co-efficient (Figure 10). A steady state diffraction efficiency of  $\sim 40\%$  was obtained in the dynamic refractive-index gratings (Figure 11). The dynamics of the grating build-up was extracted by fitting a biexponential function to the temporal evolution of diffraction efficiency that is correlated to the growth of the internal space-charge field. The modulation amplitude of the refractive index is also computed from the diffraction efficiency data. The first observation of net optical gain and significant diffraction efficiency at this important wavelength, accomplished with low-power continuous-wave laser beams, makes these hybrid nanocrystal-sensitized devices a potential choice for infrared imaging and optical communication applications.

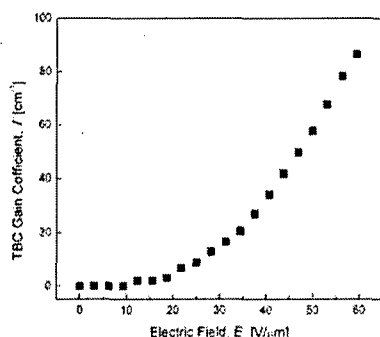


Figure 10. Electric field dependence of the TBC gain coefficient,  $\Gamma$ , in the hybrid nanocomposite at  $1.55 \mu\text{m}$ . The highest gain recorded was  $86.4 \text{ cm}^{-1}$  at  $59.4 \text{ V}\mu\text{m}^{-1}$ .

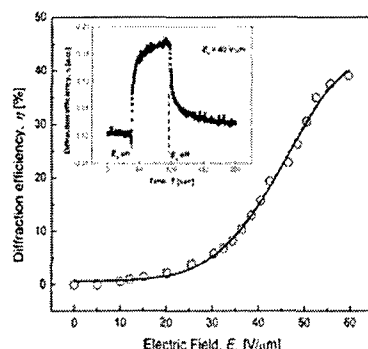


Figure 11. Main panel: Steady state diffraction efficiency,  $\eta$ , as a function of the external electric field in the nanocomposite at  $1.55 \mu\text{m}$ . The solid line is a theoretical fit to the experimental data. Inset: Transient growth of the DFWM diffracted signal at an applied field of  $40 \text{ V}\mu\text{m}^{-1}$ .

### c. Solution processed hybrid polymeric nanocomposite for infrared photodetection

This task was taken to enhance the photosensitivity. An organic/inorganic polymeric nanocomposite, incorporating a soluble precursor to the semiconductor pentacene, poly-N-vinyl carbazole and lead selenide quantum dots as photosensitizer, was fabricated. Thin-film devices were spin coated from the composite solution. Following thermal conversion of the precursor to pentacene, the devices exhibit dramatic enhancement of infrared photocurrent (Figure

12). Efficient generation of carriers coupled with high photoconductance results in the highest quantum efficiency reported to date.

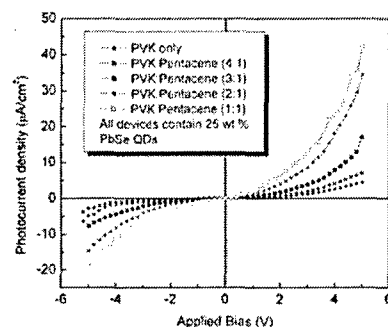


Figure 12. Photocurrent density as a function of applied voltage in devices with the same proportion of PVK: pentacene (3:1) but various amounts of PbSe nanocrystals as indicated in the legend.

## VI. Electroluminescence in Quantum Dot: Polymer Nanocomposites

*Collaboration: A.N. Cartwright, P.N. Prasad, University at Buffalo*

Our DURINT team has successfully demonstrated electroluminescence in PVK doped with quantum dots of CdSe/CdS, prepared by our new precursor route. A three-layer device structure Al/PVK:quantum dot/ITO was used. The results on electroluminescence (EL) and its comparison with photoluminescence (PL) spectral distribution are shown in Figure 13. This redshift from PL to EL is commonly observed in hybrid devices.



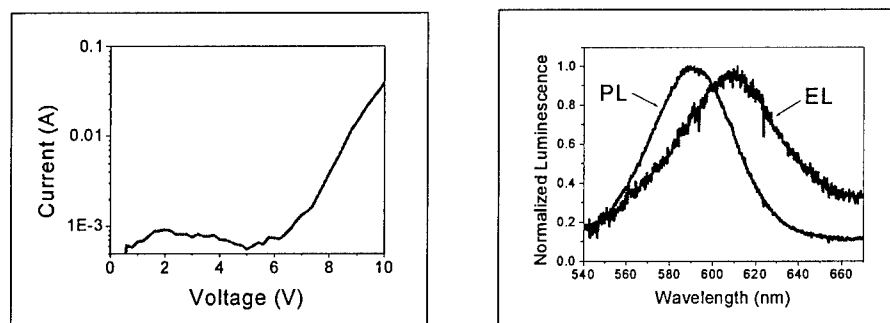


Fig 13. I-V curve (left) for electroluminescence and comparison of electroluminescence and photoluminescence spectra (right) for the CdSe/CdS quantum dot:PVK polymer nanocomposite.

## VII. Polymer Based Magnetic Nanocomposites for Electronics

*Collaboration: P. N. Prasad, H.Luo University at Buffalo  
L. Kempel, Michigan State University  
M. Alexander, AFRL, Dayton*

A major focus has also been to utilize magnetic nanoparticles containing polymers for radar applications in electronics. This is in collaboration with the Air Force Research Laboratory at Dayton. Thus we have utilized nanochemistry to produce magnetic nanoparticles of  $\text{Fe}_3\text{O}_4$ , Ni, and Co. We have also tried to align these  $\text{Fe}_3\text{O}_4$  nanoparticles in the size range of 8-12 nm by self-assembly on GaAs substrates in the presence of strong magnetic fields. A long range ordering is observed in which the particles self-assemble into a distribution of elongated clusters with a predominant orientation lengthwise along the field direction. Hysteresis loops measured parallel and perpendicular to the alignment direction show substantial directional dependence. The coercive fields in the direction parallel to the alignment field are larger than those perpendicular to it by 57% and 136% at 100K and 5K, respectively. A broad peak is observed in magnetization profiles obtained with zero- field-cooling.

We prepared a biocompatible ferrofluid containing dye-functionalized magnetite nanoparticles that can serve as fluorescent markers. This method entails the surface functionalization of magnetite nanoparticles using citric acid to produce a stable aqueous dispersion, and the subsequent binding of fluorescent dyes to the surface of the particles. Several ferrofluid samples were prepared and characterized using Fourier transform infrared spectroscopy (FTIR), x-ray photoelectron spectroscopy (XPS), thermogravimetric analysis (TGA), BET surface area analysis, transmission electron microscopy (TEM), and SQUID magnetometry. In addition, confocal fluorescence microscopy was used to study the response of the fluorescent nanoparticles to an applied magnetic field and their uptake by cells *in vitro*. Results are presented on the distribution

of particle sizes, the fluorescent and magnetic properties of the nanoparticles, and the nature of their surface bonds. Biocompatible ferrofluids with fluorescent nanoparticles enable optical tracking of basic processes at the cellular level combined with magnetophoretic manipulation, and should be of substantial value to researchers engaged in both fundamental and applied biomedical research.

For magnetic force microscopy, we are experimenting with the system itself, so that we can push it to its limit to study single particles. During this process, we have tested the system with magnetic films, and obtained several important findings. For example, we have for the first time discovered interaction between well defined magnetic domains and their subsequent movement. Fig 14 shows a sequence of images as a function of temperature, in which two magnetic domains attract each other, merging into one, eventually disappearing.

We have been able to prepare stable dispersions of metallic and magnetic nanoparticles in compatible solvents so as to blend them homogeneously in polymeric matrices. For example, Au, Pd, Ni, Fe<sub>3</sub>O<sub>4</sub> etc nanoparticles have been successfully incorporated in polymeric matrices. Frequency dependences of capacitive impedance and relative permittivity of these embedded nanoparticles have already been measured. A general enhancement of permittivity and decrease in impedance are detected.

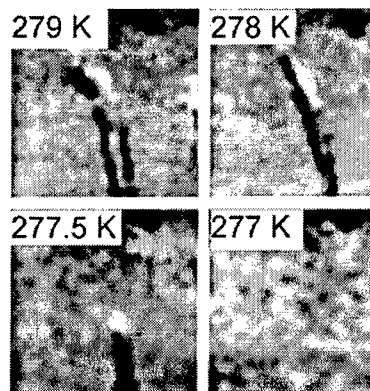


Fig 14. MFM images of two domains (the dark lines), merging together as the sample is cooled.

### VIII. Photonic Crystals with Enhanced Nonlinear Optical Response

*Collaboration: P. N. Prasad and A. N. Cartwright, University at Buffalo;*

*Y. Xia, University of Washington,*

*E. L. Thomas, M.I.T.*

*Non-DURINT Team Collaboration: R. W. Boyd, University of Rochester; J. Haus, University of Dayton.*

Photonic crystals are ordered arrays of dielectric nanostructures which have received considerable attention worldwide. Through a multidisciplinary team effort, we are focussing on novel processing methods to produce nonlinear photonic crystals where the field enhancement as well as anomalous refractive index dispersion near the band gap can be used to produce considerably increased nonlinear response.

The team effort has been directed towards using (i) self-assembling of polymeric nanoparticles on a template (with Y. Xia) and holographic lithography (with Prasad and Thomas) to produce a three-dimensional photonic crystal and (ii) a block-copolymer approach (with E. L. Thomas) to produce a one-dimensional photonic crystal. Another approach utilizes laser-directed ordering of nanoparticles to produce a one-dimensional

photonic crystal (with R. Vaia and T. Bunning at AFRL). This approach and holographic lithography are described separately in the section of "Photonicallly Aligned Nanoarrays" and "Multibeam Holographic Lithography," respectively.

To our knowledge, our team's work on the third-order nonlinear optical processes is the first reported results and show significant enhancement of these processes in photonic crystals. Our work showed that amplification in the two-photon emission, a third-order nonlinear optical process, appeared at the edge of the stop gap of the photonic crystal which was produced by dye solutions infiltrating a polystyrene photonic crystal. The amplification was interpreted as due to the local field enhancements. Our results show promises that a photonic crystal medium can be utilized for low threshold and spectrally narrowed two-photon lasing.

Third-harmonic generation (THG) is a very useful technique that can convert the coherent output of infrared lasers to shorter wavelengths in the visible and near ultraviolet. However, the smallness of the third-order optical susceptibility and the strong natural dispersion of the refractive index of most materials have prevented the practical utilization of one-step third-harmonic generation. Therefore, in practice, one employs a cascaded two-step process to produce the third harmonic with high conversion efficiency.

Having perfect phase matching of the pump and generated signal is essential for efficient nonlinear frequency conversion. One way to achieve this condition for third-harmonic generation is to use an anomalous dispersion region where the refractive index of the medium decreases with the optical frequency. In bulk media, anomalous dispersion is typically accompanied by extremely high absorption which prevents the useful implementation of this idea. However, in a photonic crystal anomalous dispersion created by the periodic structure is not accompanied by loss and strong third-harmonic generation can be obtained.

We observed a dramatic enhancement in the efficiency of third-harmonic generation using a three-dimensional (3-D) polystyrene photonic crystal medium. When an ultrashort laser pulse with the proper wavelength passes through a 3-D polystyrene-air photonic crystal, an enhancement (~25X) of single-step third-harmonic generation is observed at the short-wavelength edge of the photonic bandgap. The origin of the enhancement is due to the phase matching provided by the periodic structure of the photonic crystals.

We have also utilized a one-dimensional photonic crystal fabricated by laser-directed ordering of liquid crystal nanodroplets, to produce dramatic enhancement of third-harmonic generation near the stop-gap at the fundamental wavelengths. Our theoretical model predicts that the third-harmonic enhancement was due to both the phase matching and the pump-field localization within the structure.

Moreover, we have demonstrated electrically switchable third-harmonic generation in low refractive index contrast one-dimensional photonic crystals pumped by a near-infrared laser beam. The observed phenomenon of switching is described separately in the section of "Electrically Switchable Nonlinear Photonic Crystals."

Even though polymers, used in our experiments, possess only a weak third-order nonlinear susceptibility, we observed a strong third-harmonic generated beam. These circumstances suggest that a photonic crystal composed of a conjugated polymer, which possesses a much larger third-order nonlinearity, could produce more efficient frequency conversion, because strong nonlinear material properties and phase-matching conditions can be provided separately. Even thin layers of such photonic crystal medium could be used to fabricate infrared visualizing cards that operate at a practically important wavelength of  $1.5\ \mu\text{m}$ . Once the technology of fabrication is developed to produce photonic crystals of high optical quality and of appreciable thickness (a few millimeters), highly efficient frequency conversion of the output of coherent infrared light sources to the short-wavelength range of visible light and the ultra violet will be possible.

### Electrically Switchable Nonlinear Photonic Crystals

One-dimensional photonic crystals, which are formed by light-driven photonic alignment of liquid crystal droplets in a polymer host, can provide a medium for electrically switchable third-harmonic generation. The strong enhancement was observed in the reflection as well as in the transmission geometries; in both cases at the high-frequency band edge. The observed phenomenon of enhancement was explained theoretically with a coupled-mode model. The enhancement of the third-harmonic generation disappeared when an electric field was applied, revealing the electrical switchability of the third-harmonic generation (Fig 15). The strong switching properties were supported in the crystal up to a modulation frequency of 10 kHz but started to deteriorate at frequencies higher than 3kHz.

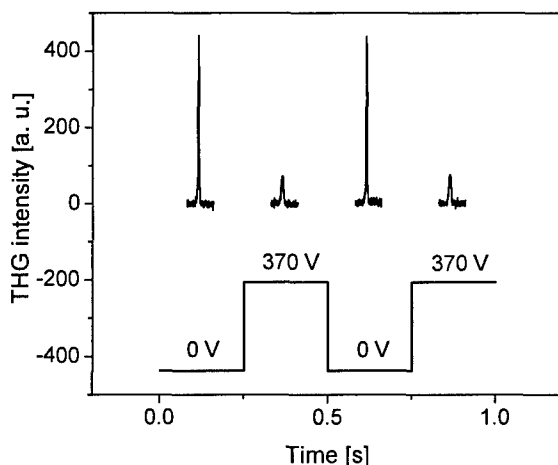
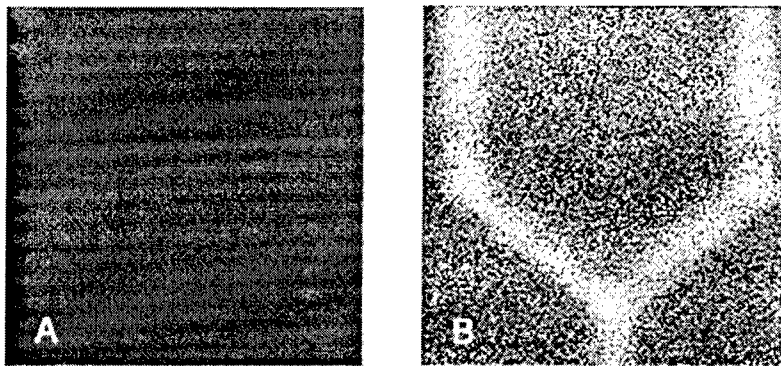


Fig. 15. Intensity of the third-harmonic signal measured in transmission geometry and plotted as a function of time (applied voltage). The lower curve indicates how the applied voltage was changing.

## Photonic Crystal Defect Engineering

The existence of periodic variation in the dielectric constant in one, two or three dimensions may cause the formation of a photonic bandgap. This bandgap forbids the propagation of light in certain range of frequencies, through the photonic crystal and gives rise to a range of interesting effects not achievable in homogeneous media. By addition or removal of some dielectric material in the photonic crystal structure one can introduce defects inside the crystal which disrupt the discrete symmetry of the lattice and create localized modes within the photonic bandgap. As a result, when light of frequency within the bandgap propagates into the defect, it becomes confined within the defect, as the crystal does not allow extended states at this frequency.

Recently we have conducted systematic studies of the two-photon polymerization technique for defect engineering in 3D polymer (polystyrene) photonic crystals. Highly controlled defect structures of different types were created inside three-dimensional polymeric photonic crystals with gaps centered in the visible region. Two of these structures are presented in Figure ....



**Figure 17.** A illustrates gratings with a resolution of  $1\mu\text{m}$ , fabricated using two photon lithography,  $10\mu\text{m}$  below the surface of the crystal made using the vertical deposition method. Figure 2B shows a beam splitter with a resolution of  $1\mu\text{m}$ , fabricated  $3\mu\text{m}$  below the surface of the crystal.

The main purpose of this investigation was to determine the optical properties of samples containing intentional defects.

In our experiments we used two methods to prepare photonic crystals: the vertical deposition method and the cell method. Comparing these two

types of colloidal photonic crystals we found that after washing away the unpolymerized parts of the resin subsequent to the lithographic process, the quality and the stability of the photonic crystal made using the cell method were much better. Our fabricated structures were of high enough quality to guide light with the losses during guiding of the fluorescence emission through the defect of about  $0.06\text{dB}/\mu\text{m}$ . Better matching of refractive index of the polymerized resin to that of the polymer spheres forming the photonic crystal and improvements in the lithographic process should lead to lowering the losses.

## IX. Multibeam Holographic Lithography

*Collaboration: P. N. Prasad,, University at Buffalo;*

*E. Thomas, MIT, Boston*

Holographic lithography is a method to fabricate periodic structures by exposing a photosensitive precursor to a defined microstructure obtained by interference of coherent light. Utilizing holographic lithography as a technique for the fabrication of photonic crystals has some advantages over the other proposed methodologies. For instance, colloidal crystals, and structures made by using colloidal crystals as templates are relatively cheap route to obtain photonic crystals. However, the growth time is relatively longer and the structures have intrinsic defects such as stacking faults, vacancies etc. More importantly they are only suitable for the fabrication of photonic crystals with face-centered-cubic (fcc) symmetry. In holographic lithography, however, various geometries with sub-micron resolution can be defined easily and written on a photo-polymerizable resin, which makes this method very suitable for the growth of photonic band gap materials.

Our team (Prasad, Thomas) has developed a procedure for fabricating excellent quality photonic crystals, in high refractive index photo-polmerizable materials by using four-beam interference lithography. We used an “umbrella” configuration with two different polarizations of the recording beams to fabricate photonic crystal structures in a photosensitive resins. In the umbrella geometry, three side beams form a tetrahedron whose base is parallel to xy plane in local xyz Cartesian coordinates. The fourth, central beam, is the tetrahedron’s height and intersects with all three other beams 1, 2 and 3 at the tetrahedron’s apex point.

Holographis lithography was used to record 3D photonic crystal structures in two different resins: ORMOCER and SU-8.

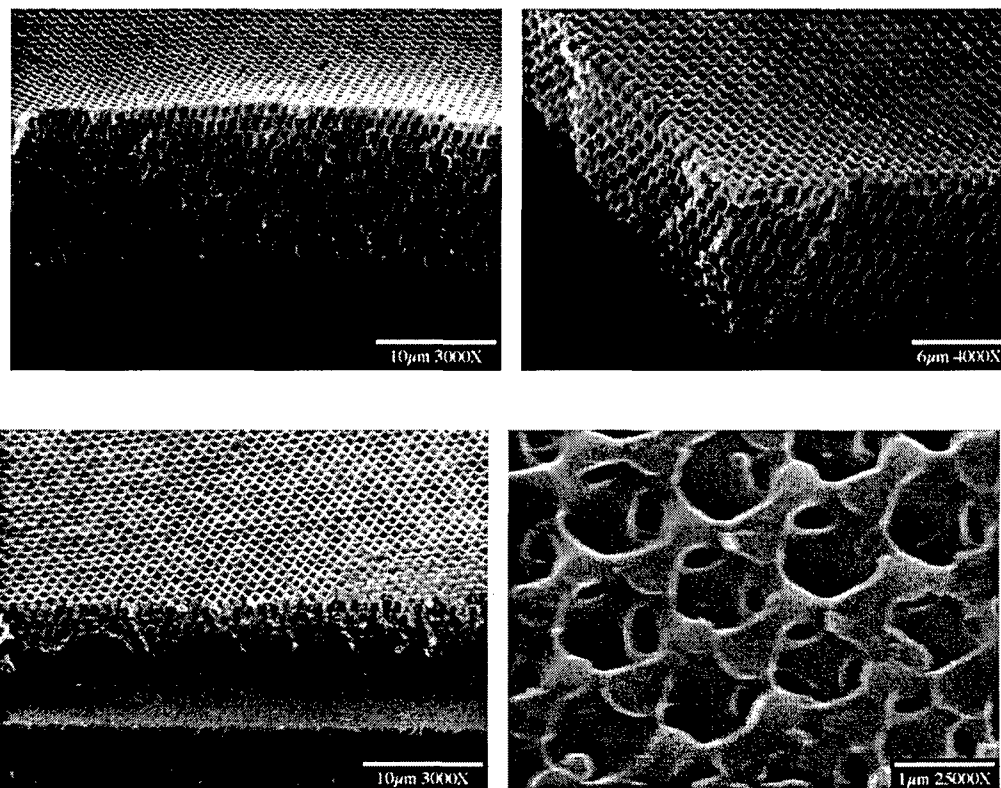


**Figure 18** .Representative SEM images of photonic crystal structures produced in SU8 resin using the umbrella configuration.

As can be seen from figure 18, crystalline structures with a very long range order can be fabricated by holographic lithography. The crystals prepared by this method showed high structural qualities. Combination of ability to produce desirable geometries and to fabricate single crystalline structures with no defects makes this method a very suitable route for the fabrication of photonic crystals.

#### **X. Photonically Aligned Nanoarray**

*Collaboration: P. N. Prasad, A. N. Cartwright, University at Buffalo;  
R. Vaia and T. Bunning, AFRL, Dayton*

A novel promising photonic approach for nanofabrication is ordering of nanoparticles that is produced by light-driven migration of nanoparticles. This method was developed at AFRL, Dayton by Bunning and Vaia. Their collaboration with us has been instrumental in utilizing this method for achieving enhanced performance in a variety of photonic functions.

This method utilizes randomly distributed nanoparticles in a matrix which can be a monomer of appropriate structure or a polymer. In a holographic approach, when two beams are crossed to generate an intensity grating, intensity modulation producing alternate bright and dark regions occur. A photoprocess induced by this intensity modulation pattern could be started with a monomer which photopolymerizes. Where there is a bright light it forms a polymer and where there is dark, it remains as a monomer. One can cross-link a polymer in the bright light, whereas in the dark region, no cross-link of the polymer occurs. If the nanoparticles do not like what is being formed, they will be squeezed out and go to the dark region. A spatial movement of the nanoparticles will occur to align them in the dark regions, producing an array of nanoparticles.

One can utilize this approach to align an array of Q-dots and metallic nanoparticles or to produce photonics crystals where the lined nanodots with high refractive index produce a high refractive index contrast. Alternatively, one can utilize the polymer-dispersed liquid crystal to align liquid crystal nanodroplets.

In collaboration with AFRL, we utilized the holographically aligned polymer dispersed liquid-crystal (H-PDLC) grating film as an angle-dependent and narrow spectral-band feedback control element for two-photon pumped lasing in a dye solution (APSS in DMSO). The grating film contained an  $\sim 15\text{ }\mu\text{m}$  thick polymer film, featuring a maximum reflectance of 75% at 561-nm position with an  $\sim 9\text{-nm}$  spectral bandwidth. The output lasing wavelength could be tuned from 561.5 to 548.5 nm and the lasing bandwidth changed from 5 to 3 nm when the incidence angle on the grating film varied from  $0^\circ$  to  $22^\circ$ . The overall lasing efficiency was measured to be 10%. The major advantages of using a H-PDLC film grating are (i) the possibility of integrating the lasing medium with the cavity feedback and spectral tunable element together to form a compact waveguide or integrated micro-lasing device, (ii) the lasing tunability by applying an external electric field.

More recently, we have used a grating, produced holographically by this method, as a one-dimensional photonic crystal and demonstrated dramatic enhancement of third-

harmonic generation in cases where the fundamental wavelength is near the stop-gap or when the third-harmonic wavelength is near the stop-gap. This is a considerably significant achievement in combining both these features to achieve practically viable third-harmonic generation.

#### **XI. Nanostructured Multicomponent Erbium Doped Glass for Significantly Enhanced Optical Amplification**

*Collaboration: P. N. Prasad, A. N. Cartwright and H. Luo,  
University at Buffalo*

*Non-DURINT Team Member: Dr. J. O'Reilly, University at Buffalo;  
T. Smith, Rochester Institute of Technology*

Silica glass is a highly attractive matrix for optical amplification due to its favorable thermal and mechanical properties. Rare earth doped silica glasses are potential materials for solid state fiber lasers, amplifiers, and upconversion lasers. At the Institute for Lasers, Photonics and Biophotonics, a process has been developed to control and modify the local environment of the doped rare earth ions. Nanostructure control was successfully used for two purposes: 1) to reduce the non-radiative quenching due to hydroxyl groups; and 2) to allow a high number density of erbium without aggregation and concentration quenching. These advances have produced an enhanced emission. Another major advancement from these procedures is a longer lifetime and greatly enhanced calculated gain at 1.5  $\mu\text{m}$ . A provisional patent has been filed for this process.

More recently, we have concentrated on developing Er doped nanostructured tellurite glasses which have high refractive index and lower frequency phonons to further enhance amplification properties and, at the same time, increase band width. We have used a novel sol-gel precursor route for producing tellurite glasses and already have some initial success in producing films of tellurite glasses.

#### **XII. Optical Microfabrication of Highly Reflective Volume Bragg Gratings using Polymer Nanocomposites**

*A.N. Cartwright, P.N. Prasad, University at Buffalo  
T. Bunning, R. Vaia, AFRL, Dayton*

This task was aimed towards developing highly efficient and simple methods of producing reflection grating using nanocomposites. Recently, in collaboration with Tim Bunning at Wright Patterson Air Force Base, we demonstrated that organic polymeric materials can yield high efficiency reflection gratings through a fast and inexpensive holographic photopolymerization technique. Specifically, multi-layer grating structures were prepared by a holographic technique using photopolymer syrups (60wt %) composed of monomer (Dipentaerythritol hydroxypentaacrylate), photoinitiator (Rose Bengal), co-initiator (N-phenylglycine), cross-linking monomer (N-vinylpyrrolidinone), liquid crystal (TL213) and non-reactive solvent (toluene) (20wt %). For the sample with



silane incorporated, toluene contains 1.5wt % 3-aminopropyltriethoxysilane. The liquid crystal is commercially available from Merck, the photoinitiator was obtained from Spectra Group Limited, and all other chemicals were obtained from Aldrich. The prepolymer syrup was mixed to ensure homogeneity with a mixer and a sonicator and then sandwiched between two glass slides. Holography was performed using the 514 nm line of an Ar ion laser with 100 mW of power; with an exposure time was 30 seconds. After laser exposure, the sandwiched cell was post-cured under a 75 W lamp for 24 hrs. The reflection notch could be observed after removing the cover glass slide from the cell and allowing the incorporated solvent to evaporate. Within the past six months, we have demonstrated that it is possible to create porous polymeric gratings without using liquid crystals. Specifically, we have demonstrated that a mixture of monomer, photoinitiator, co-initiator and formamide provides results that are almost identical to the case described in detail above (formamide replaces the liquid crystal and acetone combination). This improved technique provides a much simple fabrication method for producing 2D transmission and 1D reflection gratings.

In addition, we have demonstrated that chemical vapors can easily permeate into the voids in the grating film and consequently change the average RI and the corresponding reflective wavelength. These changes in optical response can be readily observed due to the large index difference between the air voids ( $n_{\text{air}}=1$ ) and the chemical vapor (normally  $>1.36$ ). Thus, these holographic porous polymer gratings can act as colorimetric vapor sensors. The wavelength shifts observed in these structures are far too large to be explained simply by the displacement of air in the pores by condensed acetone, as occurs in analogous porous silicon vapor sensors. According to the Bragg equation, and assuming a polymer refractive index of about 1.5, a structure with 200 nm grating spacing and 40% porosity would exhibit a wavelength shift of only about 60 nm if the pores were completely filled with liquid acetone (index = 1.36). This suggests that there is another reversible mechanism occurring that affects the optical thickness  $n_{\text{ave}}\Lambda$  of the gratings. One possible cause for this could be absorption of acetone solvent by the polymer, which would cause the grating to swell, increasing the physical grating spacing. Liquid acetone uptake has been shown to substantially swell photochemically crosslinked poly(n-butylacrylate), increasing the diameter of the polymer network by about 80%. The long-term instability of the porous polymer is significantly enhanced by adding a small amount of the silane compound, 3-aminopropyltriethoxysilane, to the prepolymer syrup. This strongly enhances the contact between the polymer and the glass, while not adversely affecting grating formation. In contrast, without the silane compound present, the sample would easily delaminate from the glass substrate, when immersed in the water. It should be noted that 3-aminopropyltriethoxysilane is commonly used for preparing amino functional surfaces on glass and silica. This suggests that the use of this compound could aid in producing porous polymer gratings useful for biosensing applications, both by rendering such devices hydrophobic and by providing an amino functional group within the porous composite which could potentially be used to target protein analytes.

## Optical Microfabrication of Highly Reflective Volume Bragg Gratings using Polymer Nanocomposites

In collaboration with the Air Force Research Laboratory at Dayton, a novel approach for fabricating wide bandwidth and highly reflective Bragg grating structures (photonic bandgap) using the technique of holographic photopolymerization of liquid crystal polymer nanocomposites was developed. The key to this fabrication method that distinguishes it from previous methods is the use of a non-reactive solvent, acetone, to dissolve the photoinitiator and cointiator in an acrylate monomer/liquid crystal (LC) mixture. The addition of acetone results in the creation of controllable periodic voids inside the thin film after the acetone evaporates. The transmission spectra of this grating together with an SEM image are shown in Figure 19. Peak reflectivity as high as 80% and a broad reflection bandwidth of 80 nm were observed in the reflection gratings formed with acetone present in the starting mixture. It was estimated from a fit to the experimental data that the resulting index mismatch was approximately 0.2 which is consistent with the presence of air voids. This index mismatch is very high when compared to the standard photopolymer system for grating formation. By backfilling with various refractive index fluids, tunable wavelength, diffraction efficiency, and bandwidth reflection notches can be formed. A provisional patent application has been filed for this technology.

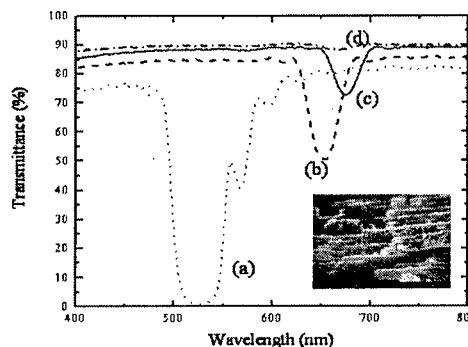


Fig 19. The spectra of the acetone sample of backfilling with different materials (a) air voids  $n_{air}=1$  (b) acetone,  $n_a=1.36$  (c) chloroform  $n_c=1.45$  and (d) toluene  $n_t=1.50$ . The inset shows SEM of the grating structure obtained using acetone in the

**Publications All of UB:**

1. F.S. Manciu, R.E. Tallman, B.D. McCombe, B.A. Weinstein, D.W. Lucey, Y. Sahoo and P.N. Prasad, "Infrared and Raman Spectroscopies of InP/II-VI Core-Shell Nanoparticles," Third International Conference on the Physics and Chemistry of Quantum Dots (QD2004), Banff, Alberta, Canada, May 10 - 13, 2004, *Physica E*
2. G.S. He, T.-C. Lin, V.K.S. Hsiao, A.N. Cartwright, P.N. Prasad, L.V. Natarajan, V.P. Tondiglia, R. Jakubiak, R.A. Vaia, T.J. Bunning, "Tunable two-photon pumped lasing using a holographic polymer-dispersed liquid-crystal grating as a distributed feedback element," *Applied Physics Letters*, 83 (14) 2733-2735, (2003).
3. A.A. Kachynski, A.N. Kuzmin, H. Pudavar, D. Kaputa, A.N. Cartwright, P.N. Prasad, "Measurement of optical trapping forces by use of the two-photon fluorescence of microspheres," *Optics Letters*, 28 (23) 2288-2290 (2003).
4. M. Furis, A.N. Cartwright, Y. Sahoo, D.J. MacRae, and P.N. Prasad, "Challenges in the optical characterization of semiconductor nanocrystals grown by colloidal chemistry," accepted for publication in *J. Phys. Chem.*, 107 (42), 11622-11625 (2003).
5. V.K.S. Hsiao, T.-C. Lin, G.S. He, A.N. Cartwright, and P.N. Prasad; L.V. Natarajan, V.P. Tondiglia and T.J. Bunning, "Optical Microfabrication of Highly Reflective Volume Bragg Gratings," submitted to *Applied Physics Letters* (APL).
6. F.S. Manciu, Y. Sahoo, D.J. MacRae, N. Furis, B.D. McCombe, P.N. Prasad, "Optical phonon spectra of GaP nanoparticles prepared by nanochemistry," *Applied Physics Letters*, 82 (23): 4059-4061 (2003).
7. M.T. Swihart, X. Li, Y. He, W.D. Kirkey, A.N. Cartwright, Y. Sahoo and P.N. Prasad, "High-rate synthesis and characterization of brightly luminescent silicon nanoparticles with applications in hybrid materials for photonics and biophotonics," *Proceedings of SPIE-The International Society for Optical Engineering* 5222, 108-117 (2003).
8. M. Furis, Y. Sahoo, D.J. MacRae, F.S. Manciu, A.N. Cartwright and P.N. Prasad, "Surfactant-Imposed Interference in the Optical Characterization of GaP Nanocrystals," *J. Phys. Chem. B*, 107, 11622-11625 (2003).
9. A.N. Cartwright, W.D. Kirkey, M.L. Furis, X. Li, Y. He, D. MacRae, Y. Sahoo, M.T. Swihart, and P.N. Prasad, "Ultrafast dynamics in nanostructured materials," *Proceedings of SPIE-The International Society for Optical Engineering* 5222, 134-139 (2003).

10. A. Goodarzi, Y. Sahoo, M.T. Swihart and P.N. Prasad, "Aqueous ferrofluid of citric acid coated magnetite particles, *Materials Research Society Symposium Proceedings* (2004), 789 (Quantum Dots, Nanoparticles and Nanowires), 129-134, 2003.
11. M. Furis, D.J. MacRae, D.W. Lucey, Y. Sahoo, A.N. Cartwright and P.N. Prasad, "Spectroscopy studies of InP nanocrystals synthesized through a fast reaction," *Materials Research Society Symposium Proceedings* (2004), 789 (Quantum Dots, Nanoparticles and Nanowires), 89-94 (2003).
12. W.D. Kirkey, A.N. Cartwright, X. Li, Y. He, M.T. Swihart, Y. Sahoo and P.N. Prasad, "Optical properties of polymer-embedded silicon nanoparticles," *Materials Research Society Symposium Proceedings* (2004), 789 (Quantum Dots, Nanoparticles and Nanowires), 357-361 (2003).
13. Y. Sahoo, M. Cheon, S. Wang, H. Luo, E.P. Furlani and P.N. Prasad, "Field-directed self-assembly of magnetic nanoparticles," *J. Phys. Chem B*, 108, 3380-3383 (2004).
14. W. Shi, Y. Sahoo and M.T. Swihart, "Gold nanoparticles surface-terminated with bifunctional ligands," *Colloids and Surfaces A*, 2004.
15. W. Shi, Y. Sahoo, M.T. Swihart and P.N. Prasad, "Preparation of Gold Nanoshells on Polystyrene Cores for Control of Surface Plasmon Resonance Absorption," to be submitted to *Langmuir*.
16. Y. Sahoo, A. Goodarzi, M.T. Swihart, T.Y. Ohulchanskyy, N. Kaur, E.P. Furlani and P.N. Prasad, "aqueous ferrofluid of magnetite nanoparticles: Fluorescence labeling and magnetophoretic control," Submitted to *J. Amer. Chem. Soc.*
17. D.W. Lucey, D.J. MacRae, M. Furis, Y. Sahoo, A.N. Cartwright and P.N. Prasad, "A Novel Organometallic Approach to the Synthesis of Monodisperse Crops of InP<sub>(QDs)</sub> in Noncoordinating Solvents," Submitted to *J. Am. Chem. Soc.*
18. H. Tiryaki, K. Baba, P.P. Markowicz and P.N. Prasad, "Linear and nonlinear optical studies in photonic crystal alloys," *Optics Letters*, V29 (19), Oct. 1 (2004).
19. P. P. Markowicz, H. Tiryaki, P.N. Prasad, V.P. Tondiglia, L.V. Natarajan, T.J. Bunning and J.W. Haus, "Electrically Switchable Third-Harmonic Generation in Photonic Crystals," submitted to *Applied Physics Letters*.
20. Y. Shen, T.-C. Lin, J. Dai, P. Markowicz and P. N. Prasad, "Near-Field Optical Imaging of Transient Absorption Dynamics in Organic Nanocrystals," *J. Phys. Chem. B* 107, 13551-13553 (2003).

21. K. Roy Choudhury, M. Samoc, A. Patra and P.N. Prasad, "Charge Carrier Transport in Poly(N-vinylcarbazole):CdS Quantum Dot Hybrid Nanocomposite," *J. Phys. Chem. B* **108**, 1556-1562 (2004).
22. P.P. Markowicz, H. Tiriyaki, H. Pudavar, P.N. Prasad, N. Lepeshkin and R.W. Boyd, "Dramatic Enhancement of Third-Harmonic Generation in 3-D-Photonic Crystals," *Phys. Rev. Lett.* **92**, 083903-1 – 083903-4 (2004).
23. A.N. Kuzmin, A.V. Kachynski, T.Y. Ohulchanskyy, I. Roy, P.N. Prasad and S. Bruckenstein, "Two-Photon Fluorescence-Guided Laser Tweezers for Study of Cluster Growth and Gelation Process," *Appl. Phys. Lett.* **84**, 2454-2456 (2004).
24. W.R. Dichtel, J.M. Serin, C. Edder, J.M.J. Frechet, M. Matuszewski, L.-S. Tan, T.Y. Ohulchanskyy and P.N. Prasad, "Singlet Oxygen Generation via Two Photon Excited FRET," *J. Am. Chem. Soc.* **126**, 5380-5381 (2004).
25. D.W. Brusmiche, J.M. Serin, J.M.J. Frechet, G.S. He, T.-S. Lin and P.N. Prasad, "Fluorescence Resonance Energy Transfer in Novel Multi-Photon Absorbing Dendritic Structures," *J. Phys. Chem. B* **108**, 8592-8600 (2004).
26. I.I. Smalyukh, A.N. Kuzmin, A.A. Kachynski, P.N. Prasad and O.D. Lavrentovich, "Optical Trapping of Colloidal Particles and Measurement of the Defect Line Tension and Colloidal Forces in a Thermotropic Nematic Liquid Crystal," submitted to *Appl. Phys. Lett.*
27. P.P. Markowicz, V.K.S. Hsiao, H. Tiriyaki, A.N. Cartwright, P.N. Prasad, K. Dolgaleva, N.N. Lepeshkin and R.W. Boyd, "Strong Enhancement of Third-Harmonic Generation at Low Energy Edge of Photonic Band Gap," in preparation.
28. "A Novel Organometallic Approach to the Synthesis of Monodisperse Crops of InP(QDs) in Noncoordinating Solvents" Derrick W. Lucey, David J. MacRae, Madalina Furis, Yudhisthira Sahoo, Alexander N. Cartwright, Paras N. Prasad *CHEMISTRY OF MATERIALS*, **17**(2005) 3754-3762.
29. "Infrared and Raman Spectroscopies of InP/II-VI Core-Shell Nanoparticles" F. S. Manciu, R. E. Tallman, B. D. McCombe, B. A. Weinstein, D. W. Lucey, Y. Sahoo and P. N. Prasad *PHYSICA E* **26** (2005) 14-18.
30. "Quasi-Reversible Photoluminescence Quenching of Stable Dispersions of Silicon Nanoparticles" William D. Kirkey, Yudhisthira Sahoo, Xuegeng Li, Yuanqing He, Mark T. Swihart, Alexander N. Cartwright, Stanley Bruckenstein, Paras N. Prasad *J. Mater. Chem.* **15** (2005) 2028-2034.
31. "Efficient Photosensitization and High Optical Gain in a Novel Quantum Dot

- Sensitized Hybrid Photorefractive Nanocomposite at Communication Wavelength” Kaushik Roy Choudhury, Yudhisthira Sahoo, Seongjin Jang, Paras N. Prasad, *ADVANCED FUNC. MATERIALS* 15(2005) 751-756.
32. “Laser-Driven Synthesis and Magnetic Properties of Iron Nanoparticles” Yuanqing He, Yudhisthira Sahoo, Shumin Wang, Hong Luo, Paras N. Prasad, and Mark T. Swihart, *JOURNAL OF NANOTECHNOLOGY*, 2005 (in press)
  33. “Chemically Fabricated Magnetic Quantum Dots of In P:Mn. Y. Sahoo, P. Poddar, H. Srikanth, D.W. Lucey, P.N. Prasad *J. PHYS. CHEM. B* (2005), 109, 15221-15225
  34. ”Ferromagnetic ordering in Mn doped InP quantum dots” P. Poddar, Y. Sahoo, H. Srikanth, P.N. Prasad, *APPLIED PHYSICS LETTERS*, 87, (2005)062506.
  35. “Ultra Efficient Photoconductive Device at Mid-IR Wavelengths From Qunatum Dot-Polymer Nanocomposites” K. RoyChoudhury, Y. Sahoo, T. Y. Ohulchansky and P. N. Prasad *APPL. PHYS. LETT*, 2005, 87, 073110.
  36. “Silver Nanoshells and Their Plasmonic Properties” Ken-Tye Yong, Yudhisthira Sahoo, Mark T. Swihart and Paras N. Prasad Submitted in *CHEMISTRY OF MATERIALS* 2005.
  37. “An Aerosol Mediated Magnetic Colloid: Study of Nickel Nanoparticles” Y. Sahoo, Y. He, M. T. Swihart, S. Wang, H. Luo, E. P. Furlani, P. N. Prasad *J. APPL. PHYS.*, 2005 98, (2005)054308.
  38. “Polyelectrolyte Adsorption on Magnetite Nanoparticles and Formation of Supraparticle Structures” Roman Sheparovych, Yudhisthira Sahoo, Paras N. Prasad, S. Wang, H. Luo, Mikhail Motornov and Sergiy Minko, Submitted to *Chem. Mater.*
  39. Theory of Magnetic Particle Capture in a Microfluidic Bioseparator E. P. Furlani, Y. Sahoo, K. Ng, J. C. Wortman, and T. E. Monk Submitted to *J. APPL. PHYS.*
  40. Hybrid quantum dot-polymer nanocomposites for infrared photorefractivity at an optical communication wavelength Kaushik Roy Choudhury, Yudhisthira Sahoo and Paras N. Prasad *ADVANCED MATERIALS* (in press).
  41. Magnetic Nanoparticles: Structure and Bioapplications Yudhisthira Sahoo, Edward Furlani, Earl Bergey Accepted as an Encyclopaedia chapter to Marcell and Dekker, NY
  42. “Solution processed pentacene-PbSe quantum dot polymeric nanocomposite for infrared photodetection” , Kaushik Roy Choudhury, Won Jin Kim, Yudhisthira Sahoo, Kwang-Sup Lee and Paras N. Prasad, Sumitted to *J. Amer. Chem. Soc.*

43. Growth of CdSe Quantum Rods and Multipods Using Noble Metal Seed Particles  
Ken-Tye Yong, Yudhisthira Sahoo, Mark T. Swihart and Paras N. Prasad  
Under submission
44. Vincent K. S. Hsiao, William D. Kirkey, Fei Chen, Alexander N. Cartwright,  
Paras N. Prasad and Timothy J. Bunning, "Organic Solvent Vapor Detection  
using Holographic Photopolymer Reflection Gratings," accepted for publication  
*Advanced Materials*, 2005.
45. K. S. Hsiao, T.-C. Lin, G. S. He, A. N. Cartwright, P. N. Prasad, L. V. Natarajan,  
V. P. Tondiglia, and T. J. Bunning, "Optical microfabrication of highly reflective  
volume Bragg gratings," *Applied Physics Letters*, **86**(1), 131113 (2005).
46. Khakimov, Z.M., P.L. Tereshchuk, F.T. Umarova, M.T. Swihart, "Non-  
conventional tight-binding method for calculation of total energy and  
spectroscopic energies of atomic clusters. Transferable parameters for silicon",  
*Physical Review B*, **72** 115335 (2005).
47. Hua, Fengjun, Mark T. Swihart, and Eli Ruckenstein, "Efficient surface grafting  
of luminescent silicon quantum dots by photoinitiated hydrosilylation", *Langmuir*,  
**21**, 6054-6062 (2005).
48. He, Yuanqing, Xuegeng Li, and Mark T. Swihart, "Laser-Driven Aerosol  
Synthesis of Nickel Nanoparticles", *Chemistry of Materials*, **17**, 1017-1026  
(2005).
49. Shi, Weili, Yudhisthira Sahoo, Mark T. Swihart, and Paras N. Prasad, "Gold  
Nanoshells on Polystyrene Cores for Control of Surface Plasmon Resonance",  
*Langmuir*, **21**, 1610-1617 (2005).
50. Sahoo, Yudhisthira, Alireza Goodarzi, Mark T. Swihart, Tymish Y.  
Ohulchansky, Navjot Kaur, Edward P. Furlani, and Paras N. Prasad, "Aqueous  
ferrofluid of magnetite nanoparticles: Fluorescence labeling and magnetophoretic  
control", *The Journal of Physical Chemistry B*, **109**, 3879-3885 (2005).
51. Liu, Gang, Mark T. Swihart, and Sriram Neelamegham, "Sensitivity, principal  
component and flux analysis applied to signal transduction: The case of epidermal  
growth factor mediated signaling", *Bioinformatics*, **21**, 1194-1202 (2005).
52. Wong, Hsi-Wu, Xuegeng Li, Mark T. Swihart, and Linda J. Broadbelt, "Detailed  
Kinetic Modeling of Silicon Nanoparticle Formation Chemistry via Automated  
Mechanism Generation", *Journal of Physical Chemistry A*, **108**, 10122-10132  
(2004).
53. Shi, Weili, Y. Sahoo, and Mark T. Swihart, "Gold nanoparticles surface-  
terminated with bifunctional ligands", *Colloids and Surfaces, A: Physicochemical*

*and Engineering Aspects*, **246**, 109-113 (2004).

54. Talukdar, Suddha S., and Mark T. Swihart, "Aerosol dynamics modeling of silicon nanoparticle formation during silane pyrolysis: a comparison of three solution methods", *Journal of Aerosol Science*, **35**, 889-908 (2004).
55. Li, Xuegeng, Yuanqing He, and Mark T. Swihart, "Surface Functionalization of Silicon Nanoparticles Produced by Laser-Driven Pyrolysis of Silane followed by HF-HNO<sub>3</sub> Etching", *Langmuir*, **20**, 4720-4727 (2004).
56. Li, Zhifeng, Mark T. Swihart, and Eli Ruckenstein, "Luminescent Silicon Nanoparticles Capped by Conductive Polyaniline through the Self-assembly Method", *Langmuir*, **20**, 1963-1971, (2004).
57. Wong, Hsi-Wu, Juan Carlos Alva Nieto, Mark T. Swihart, and Linda J. Broadbelt, "Thermochemistry of Silicon-Hydrogen Compounds Generalized from Quantum Chemical Calculations", *The Journal of Physical Chemistry A*, **108**, 874-897, (2004).
58. "Two-, Three-, and Four-Photon Pumped Stimulated Emission Properties of Ten Stilbazolium-Dyes Solutions," G. S. He, T-C. Lin, S-J. Chung, Q. Zheng, C. Lu, Y. Cui, and P. N. Prasad, *J. Opt. Soc. Amer. B* **22** (10), 2219-2228 (2005).
59. "Chemically Fabricated Magnetic Quantum Dots of InP:Mn," Y. Sahoo, P. Poddar, H. Srikanth, D. W. Lucey, and P. N. Prasad, *J. Phys. Chem. B* **109**, 15221-15225 (2005).
60. "Ultra Efficient Photoconductive Device at Mid-IR Wavelengths from Quantum Dot-Polymer Nanocomposites," K. RoyChoudhury, Y. Sahoo, T. Y. Ohulchansky, and P. N. Prasad, *Appl. Phys. Lett.* **87**, 073110-1 – 073110-3 (2005).
61. "Folate Receptor Mediated Delivery of InP Quantum Dots for Bioimaging," D. J. Bharali, D. W. Lucey, H. Jayakumar, H. E. Pudavar, and P. N. Prasad, *J. Am. Chem. Soc.* **127**, 11364-11371 (2005).
62. "Three-Dimensional Confocal Thermal Imaging Using Anti-Stokes Luminescence," A. V. Kachynski, A. N. Kuzmin, H. E. Pudavar, and P. N. Prasad, *Appl. Phys. Lett.* **87**: 023901/1 – 023901/3 (2005).
63. "Highly Efficient Photoductive Devices at Infrared Wavelengths Using Quantum Dot-polymer Nanocomposites," K. R. Choudhury, Y. Sahoo, T. Ohulchansky, and P. N. Prasad, *Appl. Phys. Lett.* **87**, 073110 (2005).
64. "An Aerosol Mediated Magnetic Colloid: Study of Nickel Nanoparticles," Y. Sahoo, Y. He, M. T. Swihart, S. Wang, H. Luo, E. P. Furlani, and P. N. Prasad, *J.*



Appl. Phys. 98, 054308/1 – 054308/6 (2005).

65. "Elasticity-Mediated Self-Organization and Colloidal Interactions of Solid Spheres with Tangential Anchoring in a Nematic Liquid Crystal," I. I. Smalyukh, O. D. Lavrentovich, A. N. Kuzmin, A. V. Kachynski, and P. N. Prasad, Phys. Rev. Lett. 95, 157801/1 – 157801/4 (2005).
66. "Hybrid Quantum Dot-Polymer Nanocomposite for Infrared Photorefractivity at the Optical Communication Wavelength of 1,550 nm," K. Roy Choudhury, Y. Sahoo, and P. N. Prasad, Adv. Mater. 17(23), (2005) 2877-2881.
67. "Ferromagnetic Ordering in Mn Doped InP Quantum Dots," P. Poddar, Y. Sahoo, H. Srikanth, and P. N. Prasad, Appl. Phys. Lett. 87, 062506/1 – 062506/3 (2005).
68. "Developments and Opportunities in Polymer-Based New Frontiers of Nanophotonics and Biophotonics," P. N. Prasad in New Polymeric Materials, eds. L. S. Korugic-Karasz, W. J. MacKnight, and E. Martuscelli, ACS Symposium Series 916, pp. 6-17 (2005).
69. "A  $\pi$ -Conjugated Dendritic Nano-Sized Chromophore with Enhanced Two-Photon Absorption," Q. Zheng, G. S. He, and P. N. Prasad, Chem. Mater. 7-(24) 6004-6011 (2005) ACS on SciFinder (R).
70. "Dynamics of Multiple Trapping by a Single-Beam Laser Tweezer," D. S. Kaputa, A. N. Kuzmin, A. V. Kachynski, A. N. Cartwright and P. N. Prasad, Appl. Optics 44(19) 3963-8 (2005).
71. "Shape and Structure Control of PbSe Nanocrystals Using Noble Metal Seed Particles," K-T. Yong, Y. Sahoo, K. R. Choudhury, M. T. Swihart, J. R. Minter, and P. N. Prasad, Nano Lett. 6(4), 709-714 (2006).
72. "A General Approach to Binary and Ternary Hybrid Nanocrystals," W. Shi, H. Zeng, Y. Sahoo, T. Y. Ohulchanskyy, Y. Ding, Z. L. Wang, M. Swihart, and P. N. Prasad, Nano Lett. 6(4), 875-881 (2006).
73. "Polyelectrolyte Stabilized Nanowires From Fe<sub>3</sub>O<sub>4</sub> Nanoparticles via Magnetic Field Induced Self Assembly," R. Sheparovych, Y. Sahoo, M. Motornov, S. Wang, H. Luo, P. N. Prasad, I. Sokolov, and S. Minko, Chem. Mater. (Communication) 18(3), 591-593 (2006).
74. "Colorimetric Porous Photonic Bandgap Sensors with Integrated CMOS Color Detectors," X. Y. Fang, V. K. S. Hsaio, V. P. Chodavarapu, A. H. Titus, A. N. Cartwright, P. N. Prasad, and F. V. Bright, IEEE Sensors Journal (2006).
75. "Experimental Verification of the Applicability of the Homogenization Approximation to Rough One-Dimensional Photonic Crystals Using a

- Holographically Fabricated Reflection Grating,” K. R. Maskaly, V. K. S. Hsiao, A. N. Cartwright, P. N. Prasad, P. F. Lloyd, T. J. Bunning, and W. C. Carter, publication in the Journal of Applied Physics (2006).
76. “Laser-Driven Synthesis and Magnetic Properties of Iron Nanoparticles,” Y. He, Y. Sahoo, S. Wang, H. Luo, P. N. Prasad, and M. T. Swihart, J. Nanoparticle Research (published on line) (2006).
  77. “Aggregation-Enhanced Fluorescence and Two-Photon Absorption in Nanoaggregate and Organically Modified Silica Nanoparticles of Novel 9,10-Bis[4-(4'-amino styryl)styryl] anthrolene Derivatives,” S. Kim, Q. Zheng, G. S. He, D. J. Bharali, H. E. Pudavar, A. Baev, and P. N. Prasad, Adv. Func. Mat., 2006 ACS on SciFinder.
  78. “Synthesis, Two- and Three-Photon Absorption and Optical Limiting Properties of Fluorene-Containing Ferrocene Derivatives,” Q. Zheng, G. S. He, C. Lu, and P. N. Prasad, (C) 2006 ACS on SciFinder (R).
  79. “Solution-Processed Pentacene-PbSe Quantum Dots: Polymeric Nanocomposite as Efficient Infrared Photodetectors,” K. Roy Choudhury, W. Jin, Y. Sahoo, K.-S. Lee, and P. N. Prasad, Appl. Phys. Lett. (in Press).
  80. “DNA-Ormocer Nanocomposite – A New Biocomposite for Fabrication of Photonic Structures,” P. Gupta, P. P. Markowicz, K. Baba, J. O'Reilly, M. Samoc, and P. N. Prasad, Appl. Phys. Lett. (in Press).
  81. “Anisotropic Growth of PbSe Nanocrystals on Au-Fe<sub>3</sub>O<sub>4</sub> Hybrid Nanoparticles,” W. Shi, Y. Sahoo, H. Zeng, Y. Ding, M. Swihart, and P. N. Prasad, Adv. Mater. (in Press).
  82. “Efficient Photodetection at Infrared Wavelengths by Incorporation of PbSe-Carbon-Nanotube Conjugate in a Polymeric Nanocomposite,” N. Cho, K. Roy Choudhury, Y. Sahoo, T. Ohulchanskyy, K.-S. Lee, and P. N. Prasad, Adv. Mater. (2006) (*in press*).
  83. “Tuning Plasmonic Resonances by Multi Curvature Gold and Silver Nanoshells,” K.-T. Yong, Y. Sahoo, M. T. Swihart, and P. N. Prasad, submitted to Colloids and Surfaces, (2006)
  84. “Controllable One-Dimensional Photonic Bandgap (PBG) Structure Based on Photopolymer Systems,” V. K. S. Hsiao, A. N. Cartwright, P. N. Prasad, P. F. Lloyd, and T. J. Bunning, manuscript under preparation.
  85. “Three Color Reflector Fabricated with Holographic Photopolymers,” V. K. S. Hsiao, A. N. Cartwright, P. N. Prasad, K. R. Maskaly, and E. L. Thomas, manuscript under preparation.

### **Invited Talks and Lectures:**

1. Key Note Lecture, SPIE Annual Meeting, San Diego, August 4, 2003.  
"Future Opportunities in Nanophotonics".
2. Half-day Short Course on Nanophotonics, SPIE Annual Meeting, San Diego, CA, August 4, 2003.
3. Plenary Lecture, INAOE (School of OPTICS Conference), Pueblo, MEXICO, September 8-10, 2003.  
"Emerging Opportunities at the Interface of Photonics, Nanotechnology and Biotechnology".
4. Invited Lecture, Symposium in honor of Oesper Awardee, Nobel Laureate Professor A. MacDiarmid, Cincinnati, OH, October 11, 2003.  
"Emerging Opportunities at the Interface of Photonics, Nanoscience and Biology".
5. Invited Lecture, Caprice, ITALY, International Symposium Honoring Professor Frank E. Karasz, October 23, 2003.  
"Opportunities for Polymers in the New Frontiers of Nanophotonics and Biophotonics".
6. Invited Lecture, ICONO '7, Sorak, KOREA, November 5, 2003.  
"NanoBiophotonics: An Exciting Fusion of Biophotonics and Nanophotonics".
7. Keynote Lecture, SPIE, San Jose Conference, January 26, 2004.  
"Emerging Opportunities at the Interface of Nanotechnology, Photonics and Life Sciences".
8. Lecture Series on Biophotonics, Vitese, Ottawa, CA, February 24-27, 2004.  
"Three Lectures on "Biophotonics".
9. Invited Lecture, American Chemical Society, National Meeting, Anaheim, CA, March 28, 2004.  
"Nanoscopic Nonlinear Optical Interactions".
10. Morley Medal Lecture, The Cleveland Section of the American Chemical Society, Cleveland, OH, May 26, 2004.  
"Emerging Opportunities at the Interface of Nanochemistry, Photonics and Biomedical Sciences".
11. Plenary Lecture, Great Lakes Photonics Symposium, SPIE, Cleveland, OH, June 7, 2004.  
"Emerging Opportunities at the Interface of Photonics, Nanotechnology and Biomedical Sciences".

12. Opening Lecture, International Workshop on Photonic and Electronic Materials, Donostia (San Sebastian), Spain, June 14, 2004.  
"Emerging Opportunities in Nanophotonics and Biophotonics".
13. Opening Lecture, Workshop on Multiphoton Processes and Materials, Stockholm, Sweden, June 21, 2004.  
"Multiphoton Processes: Materials and Applications".
14. Keynote Lecture, Biophotonics 2004, Stockholm, Sweden, June 22, 2004.  
"Emerging Opportunities at the Interface of Biomedical Sciences, Photonics and Nanotechnology".
15. Keynote Lecture, SPIE Annual Meeting, Denver, CO, August 5, 2004.  
"New Opportunities in Multiphoton Science and Technology".
16. Half-Day Short Course on "Nanophotonics", SPIE Photonics East Meeting, Philadelphia, PA, October 25, 2004
17. Invited Lecture, TOBINSTOCK, Evanston, IL, November 6, 2004.  
"Nanophotonics and Nanomedicine".
18. Invited Lecture, IEEE, LEOS 2004 Conference, Rio Grande, Puerto Rico, November 9, 2004.  
"Emerging Opportunities in Nanophotonics and Biophotonics".
19. Opening Lecture, Croucher Advanced Study Institute, Hong Kong, December 6, 2004.  
"Emerging Opportunities in New Directions of Photonics: Nanophotonics and Biophotonics".
20. Plenary Lecture, MACRO 2004, Trivandrum, India, December 15, 2004.  
Polymers for Nanotechnology and Biomedical Applications".
21. 6. Invited Lecture, International Conference on Organic Photonics and Electronics 2005 & the 8<sup>th</sup> International Conference on Organic Nonlinear Optics, Matsushima, Japan, March 8, 2005.  
"Biophotonics and Nanophotonics for Nanomedicine".
22. Invited Lecture, International Workshop on DNA Photonics, Hawaii, March 28, 2005.  
"DNA Based Nano/biophotonics".
23. Invited Lecture, International Conference on Materials Research and Education: Future Trends and Opportunities, Doha, Qatar, April 4, 2005.

“Multifunctional Advanced Materials”.

24. Opening Key Note Lecture, International Conference on Frontiers of Polymers and Advanced Materials, Cancun, Mexico, April 22, 2005.  
“Emerging Opportunities at the Interface of Photonics, Nanotechnology and Biotechnologies”.
25. 10. Invited Lecture, IT Collaboratory 2005 Symposium, Rochester Institute of Technology, Rochester, New York, May 4, 2005.  
“Opportunities at the Interface of Nanotechnology and Photonics”
26. 11. International Symposium on Photonics, Biophotonics and Nanophotonics 2005, Nanjing, China, Three Main Lectures:  
Opening Key Note Lecture: “Emerging Opportunities in Photonics” May 15, 2005.  
Tutorial Lecture: “Introduction to Nanophotonics”, May 16, 2005.  
Tutorial Lecture: “Introduction to Biophotonics”, May 17, 2005.
27. Invited Lecture, East China University of Science and Technology, Shanghai, China, May 20, 2005.  
“Emerging Opportunities at the Interface of Photonics, Nanotechnology and Biotechnology”.
28. 13. Invited Lecture, Zhejiang University, Hong Zhou, China, May 22, 2005.  
“Emerging Opportunities at the Interface of Photonics, Nanotechnology, and Biotechnology”.
29. Photonics 2005, Nanophotonics, Biophotonics and Optoelectronic Polymer Systems, (ACS), Orlando, Florida June 5-8<sup>th</sup> 2005 “New Opportunities for Polymers at the Interface of Photonics, Nanotechnology and Biotechnology”
30. SPIE Optics & Photonics Meeting, San Diego California July 31-August 4  
“New Generation Photonics Materials: Design, Development, Characterization, and Applications” and New Generation Materials and Structures for Nanophotonics and Nanoelectronics”
31. Conference ESP 2005-Excited State Processes in Electronic and Bio Nanomaterials, Los Alamos National Laboratory, New Mexico, August 8-11, 2005. “Role of Excited Processes at the Nano:Bio Interface”
32. ASI on Photon Based Nanoscience and Technology, Orford Quebec, Canada, Sept 19- 24, 2005.  
“*Introduction to Nanophotonics*”
33. SPIE Optics & Photonics Meeting, San Diego California July 31-August 4  
“New Generation Photonics Materials: Design, Development, Characterization,

and Applications” and “New Generation Materials and Structures for Nanophotonics and Nanoelectronics”

34. Conference ESP 2005-Excited State Processes in Electronic and Bio Nanomaterials, Los Alamos National Laboratory, New Mexico, August 8-11, 2005. “Role of Excited Processes at the Nano:Bio Interface”
35. ACS 230<sup>th</sup> National Meeting & Exposition, Washington, D.C. August 28-Sept 1<sup>st</sup>, 2005  
“Multifunctional Nanoparticles and assemblies for nanomedicine”
36. ASI on Photon Based Nanoscience and Technology, Orford Quebec, Canada, Sept 19- 24, 2005. “Introduction to Nanophotonics”
37. Photonics West, SPIE, San Jose, Ca Jan21-25, 2006  
“Nanocontrol of Excitation & Dynamics for Nanobiophotonics”
38. Pittcon Conference, Tampa Florida, March 11-17<sup>th</sup> 2006  
“Nanomedicine Approach for Diagnostics: Real Time Monitoring and Externally Activated Targeted Therapy”

#### **Patents:**

1. “Holographic formation of periodic polymeric photonic bandgap structures for visible to IR wavelengths,” K-S Hsiao, A. N. Cartwright and P. Prasad, Disclosed to the University at Buffalo STOR May 2004, provisional patent filed July 2004.
2. Derrick W. Lucey, David J. MacRae, Paras N. Prasad, Orville T. Beachley Jr. “Process for Producing Semiconductor Nanocrystal Cores, Core-Shell, Core-Buffer-Shell and Multiple Layer Systems in a Non-Coordinating Solvent Utilizing *in-situ* Surfactant Generation” *U.S. Patent Application* 10/804,629 March 19, 2004.
3. “Holographic formation of periodic polymeric photonic bandgap structures for visible to IR wavelengths,” K-S Hsiao, A. N. Cartwright and P. Prasad, Disclosed to the University at Buffalo STOR May 2004, provisional patent filed July 2004.
4. High Density Coupling of Quantum Dots to Carbon Nanotube Surface for Efficient Photodetection  
Namchul Cho, Kaushik Roy Choudhury, Yudhisthira Sahoo, Kwang Sup Lee, and Paras N. Prasad (Filed)
5. Facile High-Yield Production of Semiconductor Quantum Rods and Multipods using Noble Metal Nanoparticles

Ken-Tye Yong, Yudhisthira Sahoo, Mark T. Swihart, and Paras N. Prasad (Filed)

6. Solution-processed pentacene quantum-dot polymeric hybrid nanocomposite photodetector  
Kaushik Roy Choudhury, Won Jin Kim, Yudhisthira Sahoo, Kwang Sup Lee, and Paras N. Prasad (Filed)

**Personnel Supported:**

PI and Co-PI involved:

Paras N. Prasad (UB); (CoPI's: Frechet, Dalton, Robinson, Xia, Thomas, Reed, McCombe)

Post-Doc's:

Koichi Baba  
Dhruba Bharali  
Nam Chul Cho  
Heng Huang  
Won Jin Kim  
Sehoon Kim  
Jia Liu  
Derrick Lucey  
Tymish Ohulchanskyy  
Haridas Pudavar  
Yudhisthira Sahoo  
Zhu Yuan Wang

Graduate Students:

Miyeon Cheon  
Preeti Gupta  
Kuei-Sen Hsiao  
Harishankar Jayakumar  
Kaushik Roy Choudhury  
Weili Shi  
Chinmay Sikdar  
Ram Thapa  
Hanify Tiryaki  
Shumin Wang  
Ken-Tye Yong

Other Researchers:

Purnendu Dutta  
Guang-Sheng He  
Gen-Chuan Xu

## **Awards and Honors:**

### **Prasad:**

Executive Director, Institute for Lasers, Photonics, and Biophotonics, State University of New York at Buffalo (9/23/99 -present).  
Professor of Medicine, State University of New York at Buffalo (9/1/99 - ).  
Samuel P. Capen Chair of Chemistry, State University of New York at Buffalo (9/1/97 - ).  
Distinguished Professor, State University of New York at Buffalo (3/15/97 - ).  
Professor and Director of Photonics Research Laboratory, Department of Chemistry, State University of New York at Buffalo (9/1/82 - 5/31/91).  
Associate Professor, Department of Chemistry, State University of New York at Buffalo (9/1/78 - 8/31/82).  
Assistant Professor, Department of Chemistry, State University of New York at Buffalo (9/1/74 -8/31/78).  
Postdoctoral Fellow, Department of Chemistry, University of Michigan, Ann Arbor (4/15/71 - 8/31/74).

Scientific American's Top 50 (2005)

Fellow of SPIE (2005).

Morley Award Recipient, Cleveland Section of the American Chemical Society (2004)

Technology/Discovery Award of Western New York Health Care Industries (2000).

Western New York American Chemical Society Schoellkopf Award (1999).

John Simon Guggenheim Fellow (1997).

SUNY Distinguished Professor (1997).

Fellow of the American Physical Society (1995).

Fellow of the Optical Society of America (1994).

### **McCombe:**

SUNY Distinguished Professor

Professor of Physics

Director of CAPEM at SUNY Buffalo

### **Cartwright:**

Director- Lasers and Photonics, Institute for Lasers, Photonics & Biophotonics  
SUNY at Buffalo

Associate Professor, Department of Electrical Engineering, SUNY at Buffalo  
International Workshop on Indium Nitride Most Valuable Contribution Award  
SUNY Chancellor's Award for Excellence in Teaching

Department of Defense, Office of Naval Research Young Investigator Award

National Science Foundation CAREER Award

University at Buffalo Reifler Award

NATO Advanced Studies Institute Travel Award



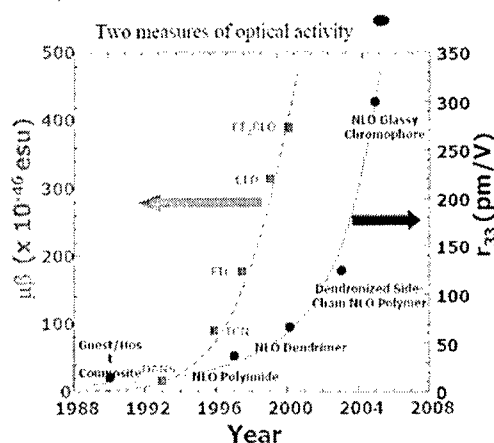
The combined Dalton and Robinson final report for the DURINT ending 2006:  
 AFOSR supported one post doc for the work describe below.  
 The funding resulted in 9 papers published in 2004 to 2006. They are listed below.  
 There are three more papers in preparation that will acknowledge AFOSR funding.

#### Prologue:

Making electro-optic (EO) modulators and other EO based components requires organizing the active component of the material to be in an acentric order. The individual components should have as large an EO activity and be as well ordered as possible to make the best device. EO activity is best summarized by the EO coefficient,  $r_{33}$ , which is related to the molecular hyperpolarizability,  $\beta_{zzz}$ , the number density,  $N$ , and the overall acentric order average (or parameter)  $\langle \cos^3 \theta \rangle$  by the relation:

$$r_{33} \propto \beta_{zzz} N \langle \cos^3 \theta \rangle$$

Therefore, theoretical understanding of the active components and the nature of the energetics of organization of those components under poling fields are necessary to design devices with the highest EO activity. Two figures of merit for optical activity are plotted as a function of time, and show a Moore's Law type increase. This type of progress in devices has been accompanied by theoretical guidance and input in choosing optimal components. The supporting theoretical efforts, which have aided in designing and developing novel materials, are detailed below.



#### Goals of this Durint:

The goal of this work has been to fully characterize the nature of organic-based nonlinear optical (ONLO) materials. This consists of two parts. The first is to calculate the hyperpolarizability of organic chromophores, which are the individual molecules that are the active constituents of ONLO materials. The second is to determine the net order of the chromophores when incorporated into the material (as a condensed matter system). In particular the computation of order is done as a function of the number density of the chromophores. The work, described below, has succeeded in meeting both of these goals.

#### Supporting Material that demonstrates program success:

The articles, cited below, most of which are now in the literature, document the success of the effort devoted to this project. One very important result has been to compare

methods of computing hyperpolarizability. Many literature discussions would give the impression that Density Function Theory (DFT) approaches to computation do not give valid results. The following paper shows that current methods using either DFT or HF methods will give accurate estimates of molecular hyperpolarizability:

E. R. Davidson, B. E. Eichinger, B. H. Robinson, "Hyperpolarizability: Calibration of Theoretical Methods for Chloroform, Water, Acetonitrile, and p-Nitroaniline"; *Optical Materials, In Press, Corrected Proof, Available online 8 May 2006*

Fundamentally, these calculations demonstrate that the current computational methods are indeed able to quantitatively and accurately (to within experimental error) predict the hyperpolarizability of ONLO chromophores, when in the gas phase.

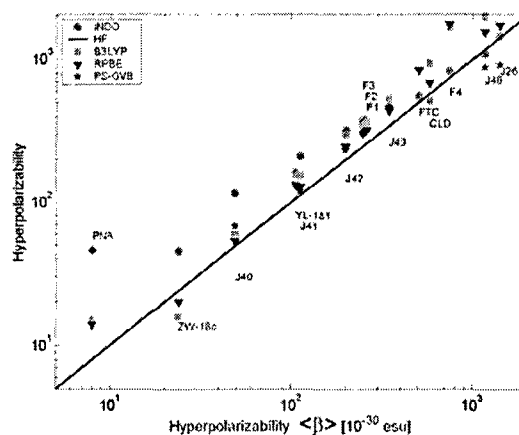
The following article makes a comparison among five different established quantum mechanical codes to determine the relative accuracy of the methods. A test set of 16 ONLO chromophores were studied. The relative rank order of the results was independent of method. Some disagreements in hyperpolarizability were found among the methods but they were considered to be rather modest. The conclusion of the study is that one may choose any standard method to compute the complete molecular hyperpolarizability tensor of individual molecules and the relative results will be consistent with other methods.

C. Isborn, A. LeClercq, F. D. Vila, J. L. Brédas, B. E. Eichinger B. H. Robinson, "Comparison of Hyperpolarizabilities Calculated with Various Quantum Mechanical Methods". Under Review J. Phys. Chem. A.

Because this article is still under review, one of the most important figures in it is reproduced here: The

hyperpolarizabilities are computed for 16 different chromophores of interest to experimentalists. The plot is a correlation plot for the different molecules. Five different techniques were used, including one Hartree-Fock (HF) method and one Density Functional Theory (DFT) method (from the Gaussian package), one method from the Goddard group, one DFT method

from Accelrys, and one semi-empirical Intermediate Neglect of Differential Overlap (INDO) method from the laboratory of J.L.Bredas. As a correlation plot, the HF method is taken as the standard and plotted along the diagonal. The results from the different methods are plotted on the ordinate for the corresponding value determined by HF method along the abscissa. The hyperpolarizability spans three decades in values. The general conclusion is that all methods follow the diagonal quite well; any method, if used consistently will give relative results that can be used to predict better performance.

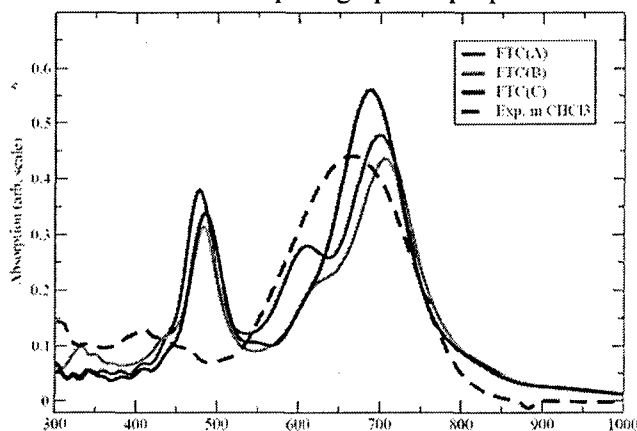


A collaboration between the Robinson and Rehr groups at the University of Washington has resulted in a paper that documents a new method for computing optical properties of ONLO chromophores with improved accuracy:

“Real time approach for non-linear optical response of photonic molecules”, Y. Takimoto, J. J. Rehr, F. D. Vila, and B. E. Eichinger, Phys. Rev. B 2006, in preparation.

The method uses Time Domain DFT. This results in more accurate estimators for optical responses. The absorption spectra shown here for a typical chromophore (FTC),

compared with the experimental spectrum, are computed as Fourier Transforms of the appropriate time domain optical function. The work was done for several rotameric forms of FTC. Quantum mechanical calculations of the effect of solvents and varied rotameric states of the ONLO chromophores have been carried out and are documented in the following articles:

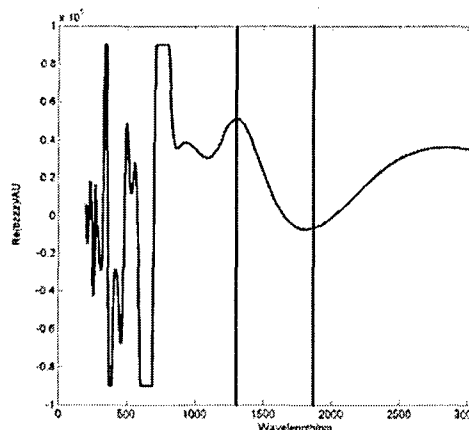


Kinnibrugh, T.; Bhattacharjee, S.; Sullivan, P.; Isborn, C.; Robinson, B. H.; Eichinger, B. E., “Influence of Isomerization on Nonlinear Optical Properties of Molecules”, J. Phys. Chem. B.; (Article); 2006; 110(27); 13512-13522.

Liao, Y.; Eichinger, B. E.; Firestone, K. A.; Haller, M.; Luo, J.; Kaminsky, W.; Benedict, J. B.; Reid, P. J.; Jen, A. K.-Y.; Dalton, L. R.; Robinson, B. H. “Systematic Study of the Structure-Property Relationship of a Series of Ferrocenyl Nonlinear Optical Chromophores”. J. Am. Chem. Soc.; (Article); 2005; 127(8); 2758-2766.

Liao, Y.; Bhattacharjee, S.; Firestone, K. A.; Eichinger, B. E.; Paranj, R.; Anderson, C. A.; Robinson, B. H.; Reid, P. J.; Dalton, L. R., “Antiparallel-Aligned Neutral-Ground-State and Zwitterionic Chromophores as a Nonlinear Optical Material”, J. Am. Chem. Soc.; (Article); 2006; 128(21); 6847-6853.

In addition to the optical spectrum of FTC, other optical properties can also be computed as a function of the wavelength of the light field. Here is the hyperpolarizability (along the molecular z axis) as a function of the wavelength of light. The vertical lines represent two important telecom wavelengths. Notice that the hyperpolarizability nearly vanishes at one of the telecom wavelengths and it close to the long wavelength limit at the other telecom wavelength. This underscores the need to

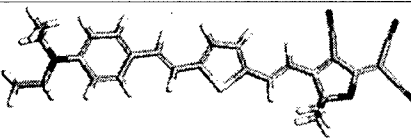
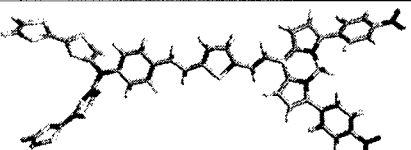


understand the wavelength dependence of the full hyperpolarizability tensor.

Marks and Ratner have suggested that a point of instability in a chromophore can lead to exceedingly large molecular hyperpolarizability. They used a Multi-Reference (MR) INDO type method to show that a twisting about a double bond at nearly 90° may lead to considerable increase in hyperpolarizability. A concept of this potential import deserves to be treated theoretically with the best possible methods. Therefore, we undertook to determine whether more exacting quantum mechanical calculations would support this conclusion. We used HF (CSS, MP2 and MP4) and DFT (several functionals and broken spin) methods and found almost no evidence to support the original claim of Marks and Ratner. We hope to be proven incorrect by experiment.

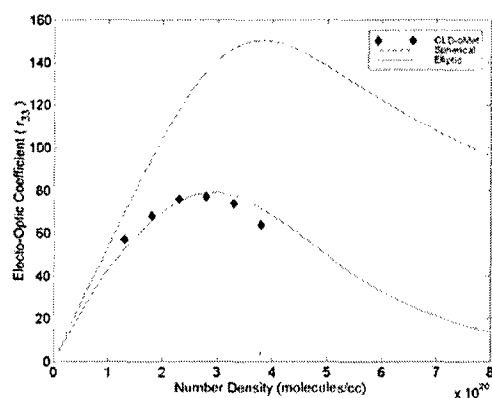
Christine M. Isborn, Ernest R. Davidson, Bruce H. Robinson, "Ab Initio Diradical/Zwitterionic Polarizabilities and Hyperpolarizabilities in Twisted Double Bonds". J. Phys. Chem. A.; (Article); 2006; 110(22); 7189-7196

More recently we have examined whether or not different donor and acceptor groups would improve hyperpolarizability. Below we illustrate that a potential 40 fold improvement over the currently used chromophore, FTC, in hyperpolarizability is possible theoretically, with some red-shift in the absorbance band. Working with experimentalists, we are now synthesizing several of these compounds. This work has not been published as it is in the preliminary stages and remains to be seen whether DFT has any predictive power here.

Designation/ HOMO-LUMO Gap	Structure	$\chi/D$	$\chi_{HRS}^{(2)}/10^{-30}$ esu	$\chi_{zzz}^{(3)}/10^{-30}$ esu
FTC 1.164 eV		26.02	168	370
BDY55 0.333 eV		27.58	6479	14951

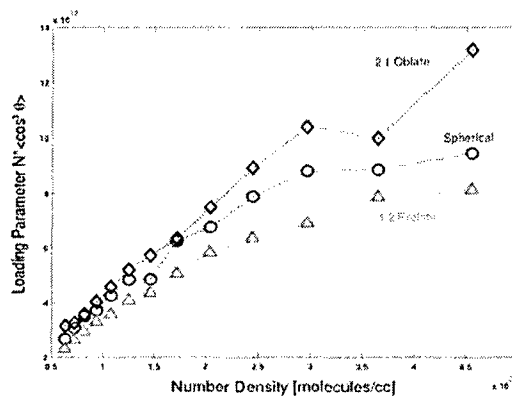
The second major thrust has been to understand the energetics of the organization of the chromophores in condensed phases. The need for this is illustrated and underscored by the now well known observation that the EO response (or activity) depends very strongly on the number density of chromophores, when the chromophores are contained in a host

material. The figure (to the right) shows that the EO activity increases with chromophore number density but then drops off. We attribute the fall-off to intermolecular electrostatics. The large dipolar interactions between chromophores tend to generate an interaction that mitigates against alignment with the poling field. The fit to the data in this figure is done with a model that takes into account the intermolecular electrostatic interactions as well as the interactions of the individual chromophores with the poling field, as well as the prolate shape of the chromophores. The model considers only the simplest phenomenological theory. However, many of the features of the model have been verified and amplified on by detailed Monte Carlo simulations of systems containing many ellipsoids. The following paper documents this effect for chromophores represented by simple ellipsoids with different shapes.

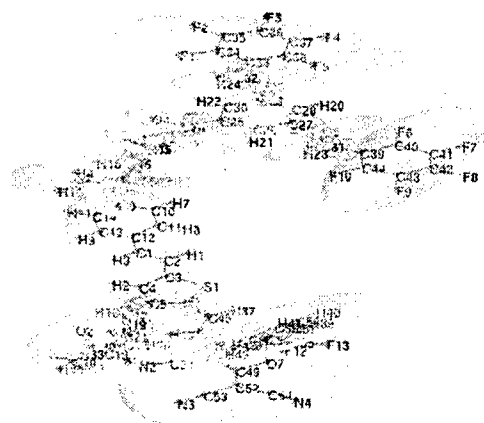


Nielsen, R. D., Rommel, H. L. and Robinson, B. H. "Simulation of the Loading Parameter in Organic Nonlinear Optical Materials". *Journal of Physical Chemistry B* 2004; **108**: 8659-8667.

The following discussion about the order in condensed matter systems simulated by Monte Carlo methods has not been published. Therefore a rather lengthy discussion of the newest results will be given. We have continued to examine the effects of the intermolecular potential on the total acentric ordering that is generated by the presence of a poling field. In particular we now carry out off-lattice calculations (which means the ellipsoids are allowed to both translate and rotate) and NPT as well as NVT calculations that determine the natural density of the chromophore system. We have found a surprising result: When the ellipsoids are allowed to move off lattice the effect of the shape of the ellipsoids on the order is nearly nonexistent. The figure to the right illustrates that for spherical, oblate and prolate ellipsoids with the same volume, the loading parameter (which is the product of the order parameter and the number density) are all very similar.

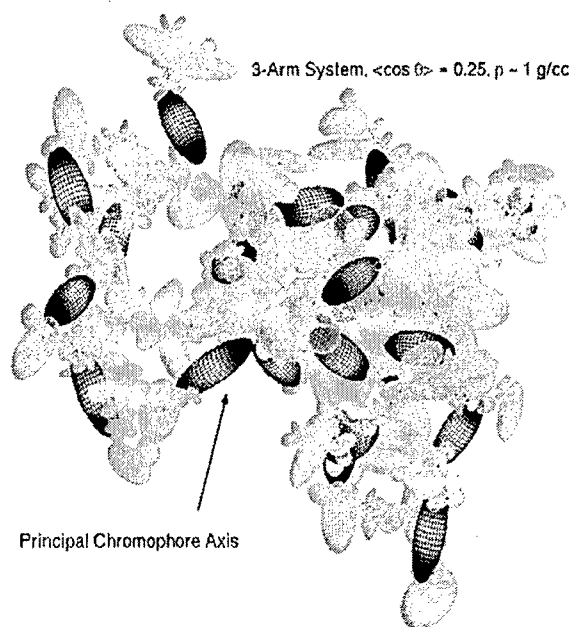


Since the early theory (illustrated in the above figure), the Robinson group has made many



advances and improvements on the theory. In particular we have modeled the detailed molecular structure of the molecules by a set of ellipsoids that map rotations of ellipsoids directly to bonds. Therefore, after moving the ellipsoids about the connections between them (where the small green circles are on the molecules), it is possible to reconstruct the molecule. Moreover, the extrapolation of molecules to ellipsoids does not allow molecularly rigid entities to rotate. To illustrate how the ellipsoids are constructed we show a simple chromophore-containing molecule with the ellipsoids overlaid on it. The chromophore part (that is molecularly rigid) is represented by two ellipsoids that cannot move with respect to each other. However,  $\text{CH}_2$  moieties are able to move with respect to their neighbors but only about the bonds connecting them. In this way the complex nature of the molecule is reduced to a simplified united-atom or coarse grained approach.

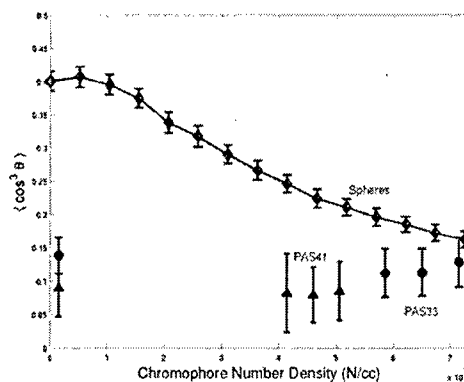
The Dalton group has made several tri-chromophore containing molecules (synthesized using the principles of dendritic synthesis). We have recently modeled the EO activity and now compare the theoretical results with those of experiment. The figure shows the structure of the system containing over thirty tri-chromophoric molecules at the density expected for this system (which is around 1 gram/cc). There is order in this system due to the presence of the poling field. In the absence of a poling field order is never



generated.

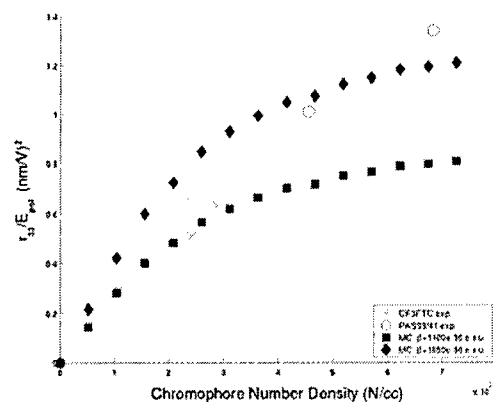
The rainbow colored parts of the molecules are the chromophores. The blue end represents the donor end of the chromophore. There is net order (around 0.25) due to the poling field. At this density the chromophore interactions (through the inter-chromophore dipole-dipole interactions) reduce the overall order.

The order of these tri-chromophore containing systems is compared to that of simple (off lattice) spheres at comparable



chromophore density. One can see that even at low density the tri-chromophore molecules have low order. That order does not change (substantially) with density. This happens because three chromophores are always in close proximity even at low density. Both molecules (PAS41 and PAS33), using the same root chromophore, have very similar order. PAS33 has a slightly higher chromophore density (at 1 gram/cc) because the molecule contains less additional non-chromophore material. The theory predicts that the more densely packed molecule will have about twice the EO activity. The experimental results, shown below, are that the more densely packed tri-chromophore system is about 50% more active. This is surprising because an increase in molecular density usually causes an increase in intermolecular interactions which reduces the loading. Here however the loading is increased by about 80% theoretically and 50% experimentally. The details of the molecular architecture appear to be important causing this reversal in the general trend. The error bars shown in the figure are not experimental error as these are theoretical results. They represent the range of values of the order parameters encountered amongst all of the replicate runs (about 50,000 such runs at each density). The individual Monte Carlo runs yield individual results because the organization is determined by different random (technically, pseudo-random) numbers.

To the right, the EO activity of the fundamental chromophore in APC (shown as Xs) is plotted as a function of the density of chromophores. The fit of the model (solid squares) to the data has no adjustable parameters. The hyperpolarizability has been measured by HRS. The agreement with the system using the polymer, APC, as a host is excellent. The agreement with the tri-chromophore systems (Os) is not as good. As shown, the general trend of the two tri-chromophore molecules is about 50% larger than that predicted by the spherical ellipsoids and about twice that predicted using the tri-chromophore molecules (see the previous figure). The fact that our results are within a factor of two of the experimental system is really quite remarkable. The details of the intermolecular interactions have been replaced by very simple rules about the van der Waals interactions and simple dipoles at the center of the chromophores. It is possible that the actual dipole moments and hyperpolarizability are somewhat different in the systems that are purely tri-chromophore molecules as opposed to the case where the individual chromophores are doped into APC. Overall, the ability to simulate large complicated systems is really very gratifying. By contrast, one cannot obtain similar results using atomistic force fields and commercially available codes: the forces are so large in those systems and codes that the chromophores do not align or move under experimental conditions.



The codes to do the Monte Carlo simulations are written in Matlab and are available upon request.

Papers that cite the support of AFOSR (some are included in the above discussion):

Liao, Y.; Firestone, K. A.; Bhattacharjee, S.; Luo, J.; Haller, M.; Hau, S.; Anderson, C. A.; Lao, D.; Eichinger, B. E.; Robinson, B. H.; Reid, P. J.; Jen, A. K.-Y.; Dalton, L. R. "Linear and Nonlinear Optical Properties of a Macrocyclic Trichromophore Bundle with Parallel-Aligned Dipole Moments". *J. Phys. Chem. B.*; (Article); 2006; 110(11); 5434-5438.

Nielsen, R. D., Rommel, H. L. and Robinson, B. H. "Simulation of the Loading Parameter in Organic Nonlinear Optical Materials". *Journal of Physical Chemistry B* 2004; **108**: 8659-8667.

Christine M. Isborn, Ernest R. Davidson, Bruce H. Robinson, "Ab Initio Diradical/Zwitterionic Polarizabilities and Hyperpolarizabilities in Twisted Double Bonds". *J. Phys. Chem. A.*; (Article); 2006; 110(22); 7189-7196

Kinnibrugh, T.; Bhattacharjee, S.; Sullivan, P.; Isborn, C.; Robinson, B. H.; Eichinger, B. E., "Influence of Isomerization on Nonlinear Optical Properties of Molecules", *J. Phys. Chem. B.*; (Article); 2006; 110(27); 13512-13522.

Liao, Y.; Eichinger, B. E.; Firestone, K. A.; Haller, M.; Luo, J.; Kaminsky, W.; Benedict, J. B.; Reid, P. J.; Jen, A. K.-Y.; Dalton, L. R.; Robinson, B. H. "Systematic Study of the Structure-Property Relationship of a Series of Ferrocenyl Nonlinear Optical Chromophores". *J. Am. Chem. Soc.*; (Article); 2005; 127(8); 2758-2766.

Liao, Y.; Bhattacharjee, S.; Firestone, K. A.; Eichinger, B. E.; Paranj, R.; Anderson, C. A.; Robinson, B. H.; Reid, P. J.; Dalton, L. R., "Antiparallel-Aligned Neutral-Ground-State and Zwitterionic Chromophores as a Nonlinear Optical Material", *J. Am. Chem. Soc.*; (Article); 2006; 128(21); 6847-6853.

"Real time approach for non-linear optical response of photonic molecules", Y. Takimoto, J. J. Rehr, F. D. Vila, and B. E. Eichinger, *Phys. Rev. B* 2006, in preparation.

C. Isborn, A. LeClercq, F. D. Vila, J. L. Brédas, B. E. Eichinger B. H. Robinson, "Comparison of Hyperpolarizabilities Calculated with Various Quantum Mechanical Methods". Under Review *J. Phys. Chem. A.*

E. R. Davidson, B. E. Eichinger, B. H. Robinson, "Hyperpolarizability: Calibration of Theoretical Methods for Chloroform, Water, Acetonitrile, and p-Nitroaniline"; *Optical Materials, In Press, Corrected Proof, Available online 8 May 2006*



To: Prof. Paras PRASAD, University at Buffalo  
Subject: DURINT Final Report  
From: Prof. Jean Frechet University of California, Berkeley

#### A. Technical Report Information

Working in close collaboration with the Wright Patterson team led by Dr. Loon-Seng Tan, of the Polymer Branch, AFRL/MLBP, Materials & Manufacturing Directorate, Air Force Research Laboratory and the Buffalo group led by Professor Paras Prasad, we have designed and prepared a variety of photoactive compounds including novel multiphoton absorbing chromophores systems based on a dendritic framework as well as micellar laser responsive systems. The multi-photon light harvesting systems can harvest and reprocess the light energy received and transform it in another form of energy making them useful in a variety of technological applications and medical applications. Therefore, the energy absorbed by the multiple 2-photon chromophores present in the system can be focused onto a single "receiver" core where it is reprocessed. We have also studied the fundamental photophysical behavior of these systems as well as their uses in applications such as up-conversion of energy, two-photon pumped lasing, optical power limiting, photocatalytic deactivation of chemical agents, targeted photodynamic therapy, and laser induced release of active compounds. Other potential applications not studied under this program due to time and funding limitations involve sensing and field-use power sources. In order to make the systems we developed practical for use with inexpensive methods of application we have made our multiphoton antennae and related functional and light triggered systems soluble in common organic solvents, thus enabling their use with standard spin-coating equipment.

For example we have prepared a novel fully modular system consisting of a energy-harvesting system containing a porphyrin (or phthalocyanin) moiety, 2-photon absorbers and solubilizing moieties for use in optical power limiting or in the generation of highly reactive singlet oxygen. This modular system is designed to be powered by IR laser excitation of peripheral two-photon chromophores; it also includes solubilizing groups since both the core porphyrin and the two-photon chromophores tend to exhibit very low solubilities. We have explored metallation of the central porphyrin to tune the properties of this system and optimize its photophysical properties depending on the metal. For example, the porphyrin-silver complex performs well in optical power limiting applications, as it is capable of converting high intensity red laser light to heat via non-radiative decay. A schematic representation of a porphyrin centered optical power limiting dendrimer is shown in Figure 1. In contrast if palladium is used in the porphyrin core, the resulting light harvesting complex becomes a remarkable photocatalyst capable of near 100% efficient production of singlet oxygen upon two-photon irradiation. A water-soluble version of this system with AF608-341 two-photon chromophores was designed and synthesized in order to also demonstrate two-photon excited FRET in aqueous medium; such a system is shown in Figure 2. Extending nonlinear optical phenomena to aqueous media can broaden the scope of our modular energy harvesting antennae to biologically or field-relevant applications and other aqueous-based applications.

We have also designed novel materials for two-photon pump lasing, but much of

this work had to be discontinued to the limited manpower available and a focus on newly designed optical power limiting materials.

Laser technology has resulted in a myriad of applications both in the civilian and military markets. The development of a portable laser system capable of inflicting severe retinal and electronic sensor damage for use in military applications has been reported. Therefore there is an increased need for protection from such high energy, frequency agile lasers to even simple laser systems such as hand-held laser pointers. Optical power limiting materials (OPL) offer the possibility of maintaining high transparency at ambient light intensities while maintaining efficient and instantaneous protection against the intense energy delivered by high power lasers.

Exploring a new design in a proof-of-concept study, we have synthesized a novel OPL organic material 1 (Figure 3), which contains a two-photon absorbing chromophore (TPAC) and a charge separation (CS) component comprised of perylene tethered to poly(3-hexyl thiophene) (P3HT). The design of this system allows for fluorescence resonance energy transfer (FRET) from the TPAC to the CS component resulting in a charge-separated state localized on perylene and P3HT. It is known that when perylene and P3HT derivatives are covalently bound they undergo rapid ( $\sim 2$  ps) photoinduced electron transfer resulting in a charge separated species when either chromophore is excited, followed by a charge recombination that is more than an order of magnitude slower ( $\sim 50$  ps). Evidence for this process can be observed in the quenched fluorescence emission of both chromophores. Transient absorption of this charge-separated species occurs within the NIR region. In order to enhance the OPL ability of this charge separation dimer for two-photon excitation within the NIR spectral region, we utilized the concept of two-photon excited FRET from a known TPAC to access this transient charge separated species. In this way we can harness the two-photon absorption efficiency of the AF-341 derivative and funnel its excited state energy into producing the transient charge separated species required for reverse saturable absorption (RSA) and ultimately OPL of the input laser pulse. Both charge separation components and two-photon absorbing chromophores have been utilized independently for optical power limiting (OPL), but we have found that combining these in a single macromolecule provides enhanced OPL behavior relative to the individual components. This work has demonstrated the synthesis of a novel optical power limiting material containing O-alkylated AF-341 as the two-photon absorbing chromophore covalently appended to a perylene-P3HT charge-separation dimer. This system is transparent within the NIR region under low power intensities and then becomes strongly absorbing at high laser intensities. Such optical properties may offer protection of NIR sensors/heat sensors against damage from high intensity light. One- and two-photon excitation studies indicate that FRET occurs from the TPAC to the perylene-P3HT dimer resulting in charge separation. To our knowledge, this is the first reported organic material capable of TP excited FRET to a CS dimer. It is believed that a mechanism of absorption derived from a rapidly photogenerated charge separated state is what gives rise to the excellent observed optical power limiting behavior.

Similar approach could be used to design novel multichromophoric light harvesting molecules that absorb and convert UV and visible radiation.

During the course of this study, numerous samples of active materials have been

exchanged with Dr. Loon Seng Tan of the Air Force Research Laboratories at Wright Patterson AFB and numerous measurements and model applications have been carried out in his laboratory.

Finally, we have carried out studies that have unambiguously demonstrated the feasibility of stimuli-responsive micellar systems capable of releasing an active payload upon IR laser excitation. This is normally very difficult to achieve since the energy of IR photons is generally much too low to enable chemical transformations. However, the combination of multiphoton chromophores than can “pool” energy to achieve sufficient energy levels (e.g. pool the energy of 2 or more IR photons to achieve an energy level equivalent to that of a UV photon) with a moiety capable of undergoing a drastic structural change upon irradiation has allowed us to demonstrate the feasibility of this approach with a family of diazo-1,2-napthoquinones. Micelles produced from appropriately designed polymeric versions of this 2-photon absorbing chromophore have been shown to be capable of a photoinduced molecular rearrangement, which drastically alter their physical properties, while enabling the IR triggered release of a payload (Figure 4). This concept of multiphoton induced rearrangement and payload release shows promise for light triggered stimuli-responsive systems for field use.

B. Provide program statistics as outlined below:

-----  
(1) Number of PI and Co-PI involved in the research project :   1    
(list on an attached page)

(2) Number of Post Doc Supported under AFOSR:  
  3    
(list on an attached page)

(3) Number of graduate students supported by AFOSR:   6    
(list on an attached page)

(4) Other researchers supported by AFOSR:  
            
(list on an attached page)

(5) Number of publications by PI's in the last 3 year period (2003-06) in refereed journals  110 

(6) Number of publications in the last 12 months (in refereed journals only) that acknowledge AFOSR supports:   29    
(list on an attached page)

(7) Awards and Honors received by the PI (life-time received): 18  
(list on an attached page)

-----  
C. Report transitions in the format outlined below. A transition item is

defined as some research results that were used by technology developers for specific technology development.

a) J.M.J. Fréchet, University of California, Berkeley.

b) 2-photon absorbing/converting molecular assemblies

c) transition to: Loon-Seng Tan, Ph.D., Materials & Manufacturing Directorate  
Air Force Research Laboratory, Wright-Patterson AFB, OH 45433-7750, Phone:  
(937)255-9141

d) application: Optical limiting, laser light conversion, singlet oxygen production, decontamination, laser light triggered release of payload in field use.

a) J.M.J. Fréchet, University of California, Berkeley.

b) Multiphoton harvesting dendritic molecules

c) Prof. Paras N. Prasad, University at Buffalo, Phone: (716) 645-6800 ext. 2099,

d) application: uphill energy conversion, generation of reactive molecules, 2-photon lasing

### **(1) (2) (3) Detailed lists**

(1) PI: Jean M.J. FRECHET

(2) Postdocs: Dr. Darryl Brousmiche, Dr. Katya Kadnikova, Dr. Jinsong Liu

(3) Graduate Students: Dr. Jason Serin, Dr. William Dichtel, Dr. Paul Furuta; Mr. Michael Oar, Mr. Justin Mynar, Mr. Andrew Goodwin.

### **(6) List of 2003-6 publications with AFOSR support**

\* Dichtel, W.R.; Baek, K-Y.; Fréchet, J.M.J.; Rietveld, I.B.; Vinogradov, S.A.;  
Amphiphilic Diblock Star Polymer Catalysts via Atom Transfer Radical Polymerization.  
J. Poly. Sci. A 2006 in press.

\* DeLongchamp, D.M.; Sambasivan, S.; Fischer, D. A.; Lin, E. K.; Chang, P.; Murphy,  
A. R.; Fréchet, J. M. J.; Subramanian, V. Direct correlation of organic semiconductor  
film structure to field-effect mobility. Adv. Mat. 2005, 17(19), 2340-2344.

\* Subramanian, V.; Fréchet, J. M. J.; Chang, P. C.; de la Fuente Vornbrock, A.; Huang,  
D. C.; Lee, J. B.; Mattis, B. A.; Moles, S.; Murphy, A. R.; Redinger, D. R.; Volkman, S.  
K. Printed organic transistors for low-cost RFID applications. Proceedings of SPIE-  
The International Society for Optical Engineering 2005, 5940, (594013/1-594013/9)  
170-178.

\* Dichtel, W.R.; Hecht, S.; Fréchet, J.M.J. Functionally Layered Dendrimers: A New  
Building Block and its Application to the Synthesis of Multichromophoric Light-  
Harvesting Systems. Org. Lett. 2005, 7, 4451-4454.

\* Goh, Chiatzun; Kline, R. Joseph; McGehee, Michael D.; Kadnikova, Ekaterina N.;  
Fréchet, Jean M. J.. Molecular-weight-dependent mobilities in regioregular poly(3-  
hexyl-thiophene) diodes. Applied Physics Letters (2005), 86(12), 122110/1-122110/3.

\* Amanda R. Murphy, Jinsong Liu, Christine Luscombe, David Kavulak, Jean M. J.  
Fréchet, R. Joseph Kline, and Michael D. McGehee. Synthesis, Characterization, and  
Field-Effect Transistor Performance of Carboxylate-Functionalized Polythiophenes with  
Increased Air Stability. Chem Mater. 2005, 17, 4892-99.

- \* Oar, M. A.; Serin, J. M.; Dichtel, W. R.; Fréchet, J. M. J.; Ohulchanskyy, T. Y.; Prasad, P. N.; Photosensitization of Singlet Oxygen via Two-Photon-Excited Fluorescence Resonance Energy Transfer in a Water-Soluble Dendrimer. *Chem. Mater.* 2005; 17, 2267-2275
- \* Goodwin, Andrew P.; Mynar, Justin L.; Ma, Yingzhong; Fleming, Graham R.; Fréchet, Jean M. J.. Synthetic Micelle Sensitive to IR Light via a Two-Photon Process. *J. Am. Chem. Soc.* 2005 127(28), 9952-9953
- \* Fréchet, J.M.J. Functional Polymers: from Plastic Electronics to Polymer-

assisted Therapeutics. *Progress in Polymer Science* 2005, 30, 844-857

- \* Furuta, P.T.; Deng, L.; Garon, S.; Thompson, M.E.; Fréchet, J.M.J.;

Platinum Functionalized Random Copolymers for use in Solution

Processible Efficient White Organic Light Emitting Diodes. *J. Am. Chem.*

*Soc.* 2004, 126, 15388-9

- \* Chang, P.C.; Lee, J.; Huang, D.; Subramanian, V.; Murphy, A. R.; Fréchet, J.M.J. Film Morphology and Thin Film Transistor Performance of Solution Processed Oligothiophenes. *Chem. Mater.* 2004; 16, 4783-4789
- \* Liu, J; Kadnikova, E.N.; Liu, Y; McGehee, M.D.; Fréchet, J.M.J. Polythiophene Containing Thermally Removable Solubilizing Groups Enhances the Interface and the Performance of Polymer-Titania Hybrid Solar Cells. *J. Am. Chem. Soc.* 2004, 126, 9486-9487
- \* Brousmiche, D. W.; Serin, J. M.; Fréchet, J. M. J.; He, G. S.; Lin, T-C.; Chung, S.-J.; Prasad, P. N.; Kannan, R.; Tan, L.-S.; Fluorescence Resonance Energy Transfer in Novel Multiphoton Absorbing Dendritic Structures. *J. Phys. Chem. B.* 2004; 108, 8592-8600
- \* Liu, J.; Tanaka, T.; Sivula, K.; Alivisatos, A.P.; Fréchet, J.M.J. Employing End-Functional Polythiophene to Control the Morphology of Nanocrystal-Polymer composites in Hybrid Solar Cells. *J. Am. Chem. Soc.* 2004, 126, 6550-6551
- \* Dichtel, William R.; Serin, Jason M.; Edder, Carine; Fréchet, Jean M. J.; Matuszewski, Michael; Tan, Loon-Seng; Ohulchanskyy, Tymish Y.; Prasad, Paras N. Singlet Oxygen Generation via Two-Photon Excited FRET. *Journal of the American Chemical Society* (2004), 126(17), 5380-5381
- \* Murphy, A.R.; Fréchet, J.M.J.; Chang, P.; Lee, J.; Subramanian, V. Organic Thin Film Transistors from a Soluble Oligothiophene Derivative Containing Thermally Removable Solubilizing Groups. *J. Am. Chem. Soc.*, 2004, 126(6), 1596-1597
- \* Liu, J; Kadnikova, E.N.; Liu, Y; McGehee, M.D.; Fréchet, J.M.J. Polythiophene Containing Thermally Removable Solubilizing Groups Enhances the Interface and the Performance of Polymer-Titania Hybrid Solar Cells. *J. Am. Chem. Soc.* 2004 ASAP edition
- \* Brousmiche, D. W.; Serin, J. M.; Fréchet, J. M. J.; He, G. S.; Lin, T-C.; Chung, S.-J.; Prasad, P. N.; Kannan, R.; Tan, L.-S.; Fluorescence Resonance Energy Transfer in Novel Multiphoton Absorbing Dendritic Structures. *J. Phys. Chem. B.* 2004; ASAP Edition

- \* Liu, J.; Tanaka, T.; Sivula, K.; Alivisatos, A.P.; Fréchet, J.M.J. Employing End-Functional Polythiophene to Control the Morphology of Nanocrystal-Polymer composites in Hybrid Solar Cells. *J. Am. Chem. Soc.* 2004, 126, 6550-6551
- \* Dichtel, William R.; Serin, Jason M.; Edder, Carine; Frechet, Jean M. J.; Matuszewski, Michael; Tan, Loon-Seng; Ohulchanskyy, Tymish Y.; Prasad, Paras N. Singlet Oxygen Generation via Two-Photon Excited FRET. *Journal of the American Chemical Society* (2004), 126(17), 5380-5381
- \* Murphy, A.R.; Fréchet, J.M.J.; Chang, P.; Lee, J.; Subramanian, V. Organic Thin Film Transistors from a Soluble Oligothiophene Derivative Containing Thermally Removable Solubilizing Groups. *J. Am. Chem. Soc.*, 2004, 126(6), 1596-1597
- \* Furuta, P.; Brooks, J.; Thompson, M.E.; Fréchet, J.M.J. Simultaneous Light Emission from a Mixture of Dendrimer Encapsulated Chromophores: a Model for Single-Layer Multichromophoric Organic Light-Emitting Diodes. *J. Am. Chem. Soc.* 2003, 125, 13165-72
- \* Furuta, P.; Fréchet, J.M.J. Controlling Solubility and Modulating Peripheral Function in Dendrimer Encapsulated Dyes. *J. Am. Chem. Soc.* 2003, 125, 13173-13181.
- \* Pyun, Jeffrey; Rees, Ian; Frechet, Jean M. J.; Hawker, Craig J. Evaluating the Effect of Termination by Chain-Chain Coupling in Living Free-Radical Polymerizations. *Australian Journal of Chemistry* (2003), 56(8), 775-782.
- \* Fréchet, J. M. J. Dendrimers and other Dendritic Macromolecules: from Building Blocks to Functional Assemblies in Nanoscience and Nanotechnology. *J Polym Sci. A.* 2003, 41, 3713-25.
- \* Brousmiche, D.; Serin, J.M.; Fréchet, J.M.J.; He, G.S.; Lin, T.C.; Chung, S.J.; Prasad, P.N.; Fluorescence Resonance Energy Transfer in a Novel Two-photon Absorbing System. *J. Am. Chem. Soc.* 2003, 125, 1448-9.
- \* Lee, L. F.; Adronov, A.; Schaller, R. D.; Frechet, J. M. J.; Saykally, R. J. Intermolecular Coupling in Nanometric Domains of Light-Harvesting Dendrimer Films Studied by Photoluminescence Near-Field Scanning Optical Microscopy (PL NSOM). *Journal of the American Chemical Society* 2003, 125, 536-540.
- \* Fréchet, J.M.J. Dendritic Macromolecules at the Interface of Nanoscience and Nanotechnology. *Macromol. Symp.* 2003, 201, 11-22.
- \* He, G.S.; Lin, T.C.; Cui, Y.; Prasad, P.N.; Brousmiche, D.; Serin, J.M.; Fréchet, J.M.J.; Two-photon excited intramolecular energy transfer and light harvesting effect in novel dendritic systems. *Optics Letters* 2003, 28, 768-770

**(7) List of Awards and Honors received by the PI (life-time received): 25+**

*(a) Awards*

IUPAC Canadian National Committee Award, 1983.  
 Polymer Society of Japan Lecture Award, 1986.  
 American Chemical Society, Doolittle Award in Polymer Materials Science & Eng., 1986.  
 American Chemical Society, Cooperative Research Award in Polymer Science 1994.  
 American Chemical Society, ACS Award in Applied Polymer Science, 1996  
 Society of Imaging Science and Technology, Kosar Memorial Award, 1999  
 American Chemical Society, ACS Award in Polymer Chemistry, 2000  
 Elected Member of the National Academy of Sciences, 2000

Elected Fellow of the American Association for the Advancement of Science, 2000  
 Elected Fellow of the PMSE Division of the American Chemical Society, 2000  
 Elected Member National Academy of Engineering, 2000  
 Elected Fellow of the American Academy of Art and Sciences, 2000  
 American Chemical Society, Cope Scholar Award, 2001  
 American Chemical Society, 2001 Salute to Excellence Award.  
 Honorary doctorate, University of Lyon (France) 2002  
 Honorary Doctorate, University of Ottawa (Canada) 2004  
 Esselen Award for Chemistry in the service of the public 2005  
 Royal Society for Chemistry Macro Group UK 2006 Medal for Outstanding Achievement

**Figure 1. AF608-341 and metallated derivatives that demonstrate efficient energy transfer and enhanced photophysical properties for Optical Power Limiting.**

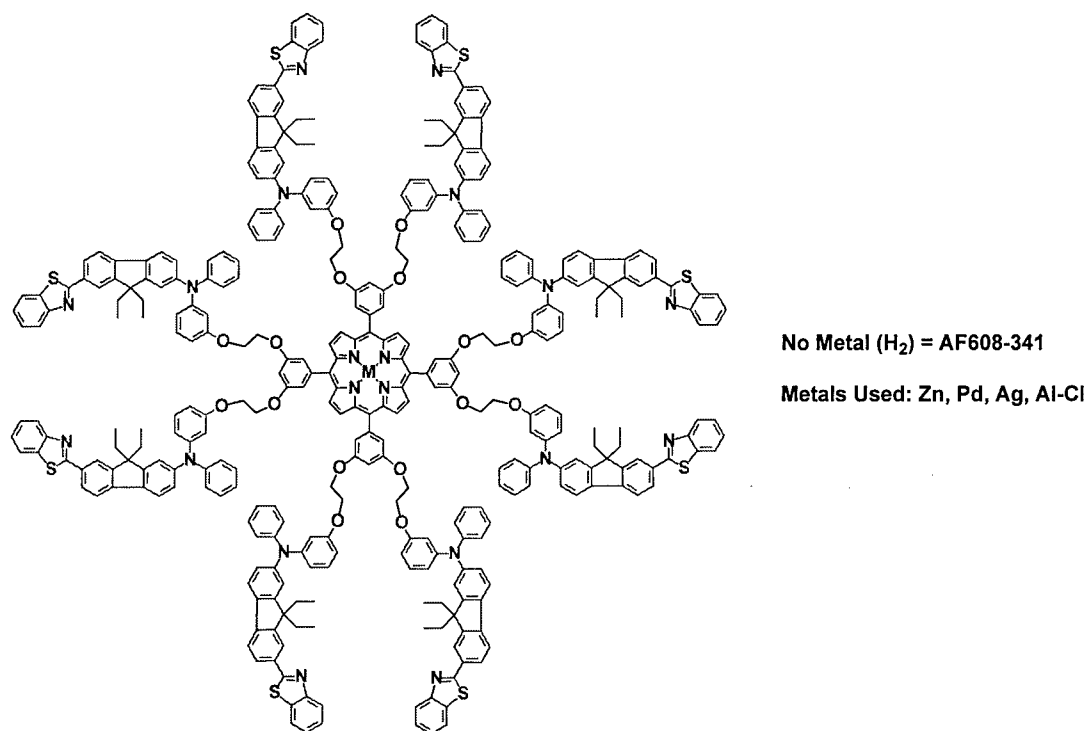






**Figure 2. Water-Soluble system capable of multi-photon excited FRET**

**and singlet oxygen**

**production.**

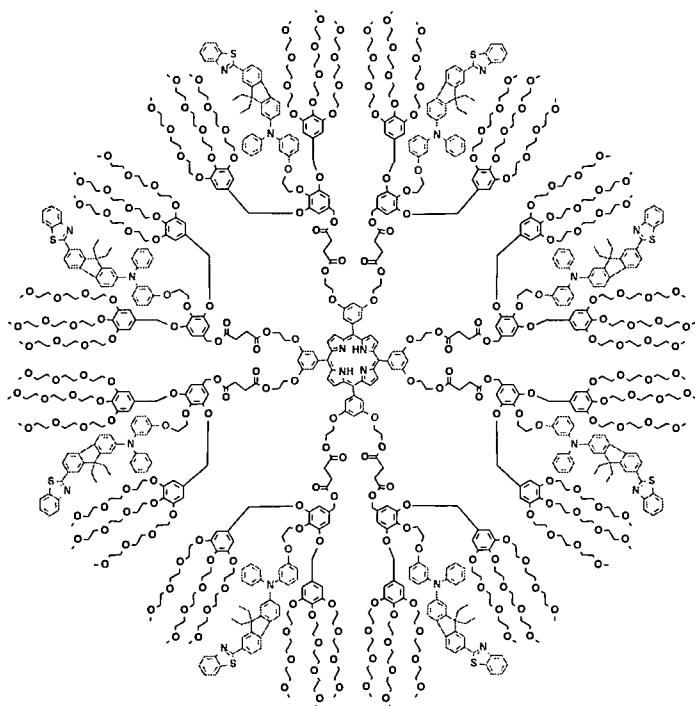


**Figure 3. Optical power limiting via 1 or 2-photon process.**

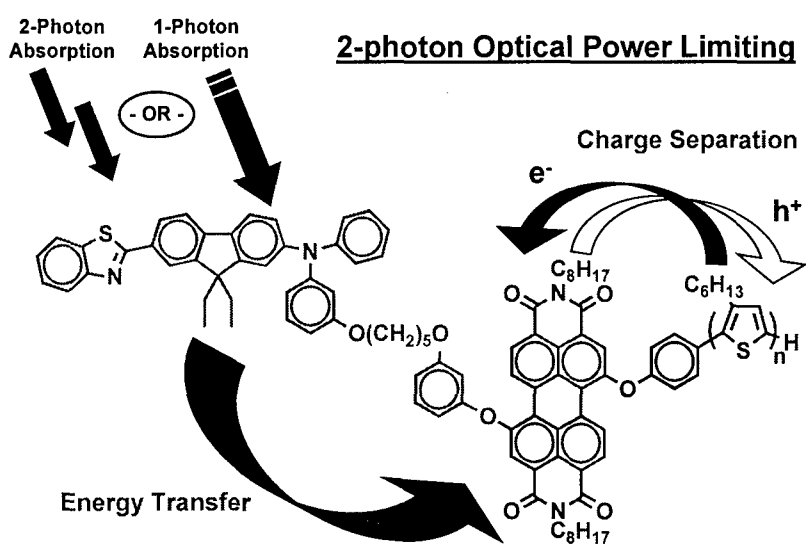
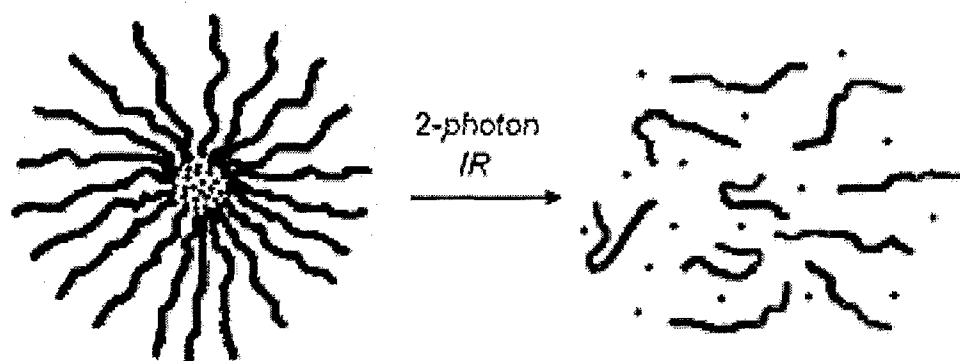


**Figure 4. Laser multiphoton induced degradation of a robust polymeric micelle with release of a active compound (shown as green dots).**



## **Objectives**

The objective of this effort was to explore electronic transport in molecular systems.

## **Status**

We elucidated the major transport mechanisms in these structures, and developed a new spectroscopic technique for analyzing these devices. We also discovered a new sub-wavelength optical effect in metallic nanowires as a result of the collaboration through this grant. The progress is detailed in the next section

## **Accomplishments/New Findings**

### **Background**

In recent years, investigators have made tremendous strides in demonstrating the basic capabilities of molecular-based electronics. However, this work consists largely of simple circuits, fabricated under carefully controlled laboratory conditions, by extremely well trained investigators. The goal of this program is to develop a hybrid molecular/solid-state circuit configuration that will be fabricated by a more scaleable and production-worthy vapor phase fabrication process. The hybrid approach builds on and combines existing capabilities of molecular and solid-state circuits: The functional unit is a bistable molecular gate consisting of either a stacked negative differential resistive (NDR) or memory molecular device. This device has already been successfully demonstrated. These active molecular gates will then be mated with a MOS-based post-processing circuit to make dense, high-performance cells. This union will be facilitated by new vapor phase deposition process will allow vastly more controlled fabrication of the fully stacked molecular gates upon a MOS-based substrate template.

Current work on molecular electronics relies, almost entirely, on liquid phase processing. Liquid phase processing is simple, it is inexpensive, and it builds upon a large body of experience with self-assembled molecular monolayers (SAMs). We now want to drive molecular circuits to a complexity that will match (and eventually exceed) that of solid-state microelectronics. Early microelectronic processing was also based on the use of liquids. However, as circuit complexity and area increased, liquid-based processing could not deliver the uniformity and reproducibility required for successful fabrication. Thus, virtually all modern semiconductor tools are based on the use of gases. Gas phase processing offers far superior uniformity and reproducibility. Indeed, when surface reactions dominate, it is possible to simultaneously deposit or etch the surfaces of dozens of stacked wafers. More subtly, gases (and ions) allow for very precise and shallow etching. This is essential in the fabrication of a circuit of microprocessor-level complexity: microprocessors cannot be fabricated in a single deposition step. The operation of the device cell, and interconnection of cells, inevitably requires a complex multi-level structure. It is thus essential that the technology allow for repeated reinsertion into deposition systems. For such a sequence of depositions to work, one must be able to clean and prepare underlying structures, in-situ, for the deposition of new materials. Controlled deposition *and* etching are thus essential.

This project is a collaboration between University of Virginia and Yale University.

Yale's responsibility was the fabrication and characterization of molecular devices; UVA had the responsibility of vapor phase molecular deposition. This report focuses on the fabrication and transport data.

### Progress and Accomplishments

The suggestion<sup>1</sup> and demonstration<sup>2</sup> of utilizing molecules as the active region of electronic devices has recently generated considerable interest in both the basic transport physics and potential technological applications of "molecular electronics".<sup>3,4</sup> However some reports of molecular mechanisms in electronic devices<sup>5,6</sup> have been shown to be premature and due to filamentary conduction,<sup>7</sup> highlighting the fabrication sensitivity of molecular structures and the need to institute reliable controls and methods to validate true molecular transport.<sup>8</sup> A related problem is the characterization of molecules in the active device structure, including their configuration, bonding, and indeed even their very presence. Here we present results on well-understood molecular assemblies, which exhibit an understood classical transport behavior, and which can be used as a control for eliminating (or understanding) fabrication variables. Utilizing tunneling spectroscopic methods, we present the first unambiguous evidence of the presence of molecules in the junction, and further confirm the charge transport mechanism obtained by standard current-voltage characterizations.

A molecular system whose structure and configuration are sufficiently well-characterized such that it can serve as a standard is the extensively studied alkanethiol ( $\text{CH}_3(\text{CH}_2)_n\text{-SH}$ ) self-assembled monolayer (SAM).<sup>9</sup> This system is useful as a control since properly prepared SAMs form single van der Waals crystals,<sup>9,10</sup> and presents a simple classical metal-insulator-metal (M-I-M) tunnel junction when fabricated between metallic contacts due to the large HOMO-LUMO gap (HOMO: highest occupied molecular orbital, LUMO: lowest unoccupied molecular orbital) of approximately 8 eV.<sup>11-13</sup>

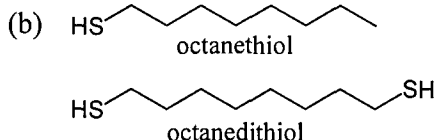
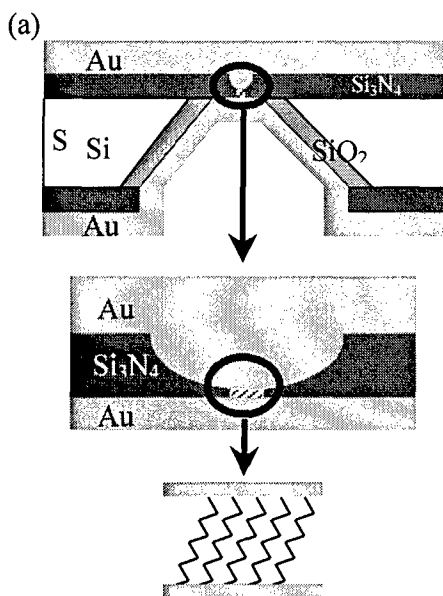
Various surface analytical tools have been utilized to investigate the surface and bulk properties of the alkanethiol SAMs, such as X-ray photoelectron spectroscopy,<sup>14</sup> Fourier transform infrared spectroscopy (FTIR),<sup>15</sup> Raman spectroscopy,<sup>16</sup> scanning tunneling microscopy (STM)<sup>10</sup> etc. For example, studies have shown that the bonding of the thiolate group to the gold surface is strong with a bonding energy of  $\sim 1.7$  eV.<sup>9</sup> STM topography examinations revealed that alkanethiols adopt the commensurate crystalline lattice characterized by a  $c(4 \times 2)$  superlattice of a  $(\sqrt{3} \times \sqrt{3})R30^\circ$ .<sup>10,17</sup> FTIR investigation showed that the orientation of the alkanethiol SAMs on Au(111) surfaces are tilted  $\sim 30^\circ$  from the surface normal.<sup>18</sup>

Electronic transport through alkanethiol SAMs have also been characterized by STM,<sup>19,20</sup> conducting atomic force microscopy,<sup>21-24</sup> mercury-drop junctions,<sup>25-28</sup> cross-wire junctions,<sup>29</sup> and electrochemical methods.<sup>30-32</sup> These investigations are exclusively at ambient temperature – clearly useful – but insufficient for an unambiguous claim that the transport mechanism is tunneling (of course expected, assuming that the Fermi levels

of the contacts lie within the large HOMO-LUMO gap). However in the absence of temperature-dependent current-voltage ( $I(V,T)$ ) characteristics, other conduction mechanisms (such as thermionic, hopping, or filamentary conduction) cannot be excluded complicate the analysis, and thus such a claim is premature.

Utilizing a nanometer scale device structure that incorporates alkanethiol SAMs, we demonstrate devices that allow  $I(V,T)$  and structure-dependent measurements<sup>33,34</sup> with results that can be compared with accepted theoretical models of M-I-M tunneling. The use of this fabrication approach is not special in any way (other than that we have so far found it to be successful) – indeed we stress that any successful device fabrication method should yield the results described below if one is characterizing the intrinsic molecular transport properties.

The electronic transport is further investigated with the technique of inelastic electron tunneling spectroscopy (IETS).<sup>34</sup> IETS was developed in the 1960's as a powerful spectroscopic tool to study the vibrational spectrum of organic molecules confined inside metal-oxide-metal junctions.<sup>35-39</sup> In our study IETS is utilized for the purpose of molecule identification, chemical bonding and conduction mechanism investigations of the "control" SAMs. The exclusive presence of well-known vibrational modes of the alkanes used are direct evidence of the molecules in the device structure, something that has to date only been inferred (with good reason, but nonetheless not unambiguously). The vibrational modes, exclusively identified as alkanes (as well as contact modes) are difficult to interpret in any other way other than as components in the active region of the device. The inelastic tunneling spectra also demonstrate that electronic tunneling occurs through the molecules, confirming the conduction mechanism obtained by  $I(V,T)$  characterizations. The specific spectral lines also yield intrinsic linewidths that may give insight into molecular conformation, and may prove to be a powerful tool in future molecular device characterization.



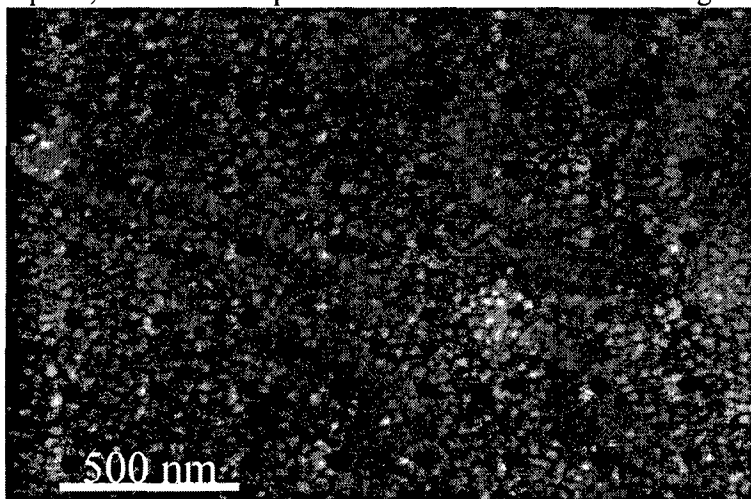
Electronic transport measurements on alkanethiol SAMs were performed using a device structure similar to one reported previously.<sup>33,34,40-42</sup> In this device, as illustrated in Figure 1(a) (not drawn to scale in the relative thickness), a number of molecules (~ several thousands) are sandwiched between two metallic contacts. This technique provides a stable device structure and makes cryogenic measurements possible. The device fabrication starts with a high resistivity silicon wafer with low stress  $\text{Si}_3\text{N}_4$  film deposited on both sides by low pressure chemical vapor deposition (LPCVD). By standard photolithography processing, a suspended  $\text{Si}_3\text{N}_4$  membrane (size of  $40\text{ }\mu\text{m} \times 40\text{ }\mu\text{m}$  and thickness of  $\sim 70\text{ nm}$ ) is fabricated on the topside of the wafer. Subsequent e-beam

lithography and reactive ion etching creates a single pore with a diameter of tens of nanometers through the membrane. As the next step, 150 nm gold is thermally evaporated onto the topside of the wafer to fill the pore and form one of the metallic contacts.

Figure 1. Schematics of a nanometer scale device used in this study (not drawn to scale in the relative thickness). (a) Top schematic is the cross section of a silicon wafer with a nanometer scale pore etched through a suspended silicon nitride membrane. Middle and bottom schematics show a Au/SAM/Au junction formed in the pore area. (b) The structures of octanethiol and octanedithiol are shown as examples.

The device is then transferred into a molecular solution to deposit the SAM layer. For our experiments, a  $\sim 5$  mM alkanethiol solution is prepared by adding  $\sim 10$   $\mu$ L alkanethiols into 10 mL ethanol.<sup>43</sup> The deposition is done in solution for 24 hours inside a nitrogen filled glove box with an oxygen level of less than 100 ppm. Three alkanemonthiol molecules of different molecular lengths—octanethiol [ $\text{CH}_3(\text{CH}_2)_7\text{SH}$ ; denoted as C8, for the number of alkyl units], dodecanethiol [ $\text{CH}_3(\text{CH}_2)_{11}\text{SH}$ , denoted as C12], and hexadecanethiol [ $\text{CH}_3(\text{CH}_2)_{15}\text{SH}$ , denoted as C16] and one alkanedithiol molecule—octanedithiol [ $\text{HS}(\text{CH}_2)_8\text{SH}$ , denoted as C8-dithiol] were used to form the active molecular components.<sup>43</sup> As representative examples, the chemical structures of octanethiol and octanedithiol are shown in Figure 1(b).

In order to statistically determine the pore size, test patterns (arrays of pores) were created under similar fabrication conditions. Figure 2 shows a scanning electron microscope (SEM) image of such test pattern arrays. This indirect measurement of device size is done since SEM examination of the actual device can cause hydrocarbon contamination of the device and subsequent contamination of the monolayer. From regression analysis of 298 pores, the device sizes of the C8, C12, C16, and C8-dithiol samples are determined as  $50 \pm 8$ ,  $45 \pm 2$ ,  $45 \pm 2$ , and  $51 \pm 5$  nm in diameters, respectively. A more ideal (less parasitic) C8 sample supercedes that of previous reports,<sup>33</sup> and derived parameters from the two data sets agree to within a standard error.



We will use these device areas as the effective contact areas. Although one could postulate that the actual area of metal that contacts the molecules may be different, there is little reason to propose it would be different as a function of length over the range of alkanethiols used, and at most would

be a constant systematic error.

Figure 2. A scanning electron microscope image of a representative array of pores used to calibrate device size. The scale bar is 500 nm.

The sample is then transferred in ambient conditions to an evaporator that has a cooling stage to deposit the opposing Au contact. During the thermal evaporation (under the pressure of  $\sim 10^{-8}$  Torr), liquid nitrogen is kept flowing through the cooling stage in order to avoid thermal damage to the molecular layer.<sup>33,44</sup> This technique reduces the kinetic energy of evaporated Au atoms at the surface of the monolayer, thus preventing Au atoms from punching through the monolayer. For the same reason the evaporation rate is kept very low. For the first 10 nm gold evaporated, the rate is less than 0.1 Å/s. Then the rate is increased slowly to 0.5 Å/s for the rest of the evaporation and a total of 200 nm gold is deposited to form the contact.

The device is subsequently packaged and loaded into a low temperature cryostat. The sample temperature is varied from 300 to 4.2 K by flowing cryogen vapor onto the sample (and thermometer) using a closed loop temperature controller. Two-terminal dc  $I(V)$  measurements are performed using a semiconductor parameter analyzer. Inelastic electron tunneling spectra are obtained via a standard lock-in second harmonic measurement technique.<sup>35,36</sup> A synthesized function generator is used to provide both the modulation and the lock-in reference signal. The second harmonic signal (proportional to  $d^2I/dV^2$ ) is directly measured using a lock-in amplifier, which is checked to be consistent with a numerical derivative of the first harmonic signal (proportional to  $dI/dV$ ). Various modulation amplitudes and frequencies are utilized to obtain the spectra. The ac modulation is added to a dc bias using operational amplifier-based custom circuitry.<sup>45</sup>

In Table 1, possible conduction mechanisms are listed with their characteristic current, temperature- and voltage-dependencies<sup>46</sup> (We do not discuss filamentary tunneling mechanisms, which are easier to categorize<sup>47</sup>). Based on whether thermal activation is involved, the conduction mechanisms fall into two distinct categories: (i) thermionic or hopping conduction which has temperature-dependent  $I(V)$  behavior and (ii) direct tunneling or Fowler-Nordheim tunneling which does not have temperature-dependent  $I(V)$  behavior. For example, thermionic and hopping conductions have been observed for 4-thioacetylphenyl SAMs<sup>40</sup> and 1,4-phenylene diisocyanide SAMs.<sup>41b</sup> On the other hand, the conduction mechanism is expected to be tunneling when the Fermi levels of contacts lie within the large HOMO-LUMO gap for short length molecule, as for the case of alkanethiol molecular system.<sup>11-13</sup> Previous work on Langmuir-Blodgett alkane monolayers<sup>48</sup> exhibited a significant impurity-dominated transport component, complicating the analysis.  $I(V)$  measurements on self-assembled alkanethiol monolayers have also been reported;<sup>19-29,49</sup> however all of these measurements were performed at fixed temperature (300 K) which is insufficient to prove tunneling as the dominant mechanism.

TABLE 1. Possible conduction mechanisms. Adapted from Ref. 46.

Conduction Mechanism	Characteristic Behavior	Temperature Dependence	Voltage Dependence
Direct Tunneling*	$J \sim V \exp(-\frac{2d}{\hbar} \sqrt{2m}\Phi)$	none	$J \sim V$
Fowler-Nordheim Tunneling	$J \sim V^2 \exp(-\frac{4d\sqrt{2m}\Phi^{3/2}}{3q\hbar V})$	none	$\ln(\frac{J}{V^2}) \sim \frac{1}{V}$
Thermionic Emission	$J \sim T^2 \exp(-\frac{\Phi - q\sqrt{qV/4\pi\epsilon d}}{kT})$	$\ln(\frac{J}{T^2}) \sim \frac{1}{T}$	$\ln(J) \sim V^{\frac{1}{2}}$
Hopping Conduction	$J \sim V \exp(-\frac{\Phi}{kT})$	$\ln(\frac{J}{V}) \sim \frac{1}{T}$	$J \sim V$

\* This characteristic of direct tunneling is valid for the low bias regime [see Eq. (3a)].

To describe the transport through a molecular system having HOMO and LUMO energy levels, one of the applicable models is the Franz two-band model.<sup>50-53</sup> This model provides a non-parabolic energy-momentum  $E(k)$  dispersion relationship by considering the contributions of both the HOMO and LUMO energy levels:<sup>50</sup>

$$k^2 = \frac{2m^*}{\hbar^2} E (1 + \frac{E}{E_g}) \quad (1)$$

where  $k$  is the imaginary part of wave vector of electrons,  $m^*$  is the electron effective mass,  $\hbar$  ( $= 2\pi\hbar$ ) is Planck's constant,  $E$  is the electron energy, and  $E_g$  is the HOMO-LUMO energy gap. From this non-parabolic  $E(k)$  relationship, the effective mass of the electron tunneling through the SAM can be deduced by knowing the barrier height of the metal-SAM-metal junction.



When the Fermi level of the metal is aligned close enough to one energy level (either HOMO or LUMO), the effect of the other distant energy level on the tunneling transport is negligible, and the widely used Simmons model<sup>54</sup> is an excellent approximation.<sup>55</sup> Simmons model expressed the tunneling current density through a barrier in the tunneling regime of  $V < \Phi_B/e$  as<sup>25,54</sup>

$$J = \left( \frac{e}{4\pi^2 \hbar d^2} \right) \left\{ \left( \Phi_B - \frac{eV}{2} \right) \exp \left[ - \frac{2(2m)^{1/2}}{\hbar} \alpha \left( \Phi_B - \frac{eV}{2} \right)^{1/2} d \right] - \left( \Phi_B + \frac{eV}{2} \right) \exp \left[ - \frac{2(2m)^{1/2}}{\hbar} \alpha \left( \Phi_B + \frac{eV}{2} \right)^{1/2} d \right] \right\} \quad (2)$$

where  $m$  is the electron mass,  $d$  is the barrier width,  $\Phi_B$  is the barrier height, and  $V$  is the applied bias. For molecular systems, the Simmons model has been modified with a parameter  $\alpha$ .<sup>25,33</sup>  $\alpha$  is a unitless adjustable parameter that is introduced to provide either a way of applying the tunneling model of a rectangular barrier to tunneling through a nonrectangular barrier,<sup>25</sup> or an adjustment to account for the effective mass ( $m^*$ ) of the tunneling electrons through a rectangular barrier,<sup>25,33,53,56</sup> or both.  $\alpha = 1$  corresponds to the case for a rectangular barrier and bare electron mass. By fitting individual  $I(V)$  data using Eq. (2),  $\Phi_B$  and  $\alpha$  values can be obtained.

Eq. (2) can be approximated in two limits: low bias and high bias as compared with the barrier height  $\Phi_B$ . For the low bias range, Eq. (2) can be approximated as<sup>54</sup>

$$J \approx \left( \frac{(2m\Phi_B)^{1/2} e^2 \alpha}{h^2 d} \right) V \exp \left[ - \frac{2(2m)^{1/2}}{\hbar} \alpha (\Phi_B)^{1/2} d \right] \quad (3a)$$

To determine the high bias limit, we compare the relative magnitudes of the first and second exponential terms in Eq. (2). At high bias, the first term is dominant and thus the current density can be approximated as

$$J \approx \left( \frac{e}{4\pi^2 \hbar d^2} \right) \left( \Phi_B - \frac{eV}{2} \right) \exp \left[ - \frac{2(2m)^{1/2}}{\hbar} \alpha \left( \Phi_B - \frac{eV}{2} \right)^{1/2} d \right] \quad (3b)$$

The tunneling currents in both bias regimes are exponentially dependent on the barrier width  $d$ . In the low bias regime the tunneling current density is  $J \propto \frac{1}{d} \exp(-\beta_0 d)$ , where  $\beta_0$  is bias-independent decay coefficient:

$$\beta_0 = \frac{2(2m)^{1/2}}{\hbar} \alpha (\Phi_B)^{1/2} \quad (4a)$$

while in the high bias regime,  $J \propto \frac{1}{d^2} \exp(-\beta_V d)$ , where  $\beta_V$  is bias-dependent decay coefficient:

$$\beta_V = \frac{2(2m)^{1/2}}{\hbar} \alpha \left( \Phi_B - \frac{eV}{2} \right)^{1/2} = \beta_0 \left( 1 - \frac{eV}{2\Phi_B} \right)^{1/2} \quad (4b)$$

At high bias  $\beta_V$  decreases as bias increases, which results from barrier lowering effect due to the applied bias.

In order to determine the conduction mechanism of self-assembled alkanethiol molecular systems I(V) measurements in a sufficiently wide temperature range (300 to 80 K) and resolution (10 K) were performed. Figure 3(a) shows a representative I(V,T) characteristic of dodecanethiol (C12) measured with the device structure as shown in Figure 1(a). Positive bias corresponds to electrons injected from the physisorbed Au contact [bottom contact in Figure 1(a)] into the molecules. By using the contact area of  $45 \pm 2$  nm in diameter determined from SEM study, a current density of  $1,500 \pm 200$  A/cm<sup>2</sup> at 1.0 Volt is determined. No significant temperature dependence of the characteristics (from V = 0 to 1.0 Volt) is observed over the range from 300 to 80 K. An Arrhenius plot (ln(I) versus 1/T) of this is shown in Figure 3(b), exhibiting little temperature dependence in the slopes of ln(I) versus 1/T at different bias and thus indicating the absence of thermal activation. Therefore, we conclude that the conduction mechanism through alkanethiol is tunneling contingent on demonstrating a correct molecular length dependence. The tunneling through alkanethiol SAMs has been assumed as “through-bond” tunneling, i.e., along the tilted molecular chains between the metal contacts.<sup>22,23,32,57</sup> Based on the applied bias as compared with the barrier height ( $\Phi_B$ ), the tunneling through a SAM layer can be categorized into either direct ( $V < \Phi_B/e$ ) or Fowler-Nordheim ( $V > \Phi_B/e$ ) tunneling. These two tunneling mechanisms can be distinguished due to their distinct voltage dependencies (see Table 1). Analysis of  $\ln(I/V^2)$  versus  $1/V$  [in Figure 3(c)] shows no significant voltage dependence, indicating no obvious Fowler-Nordheim transport behavior in this bias range (0 to 1.0 Volt) and thus determining that the barrier height is larger than the applied bias, i.e.,  $\Phi_B > 1.0$  eV. This study is restricted to applied biases  $\leq 1.0$  Volt and the transition from direct to Fowler-Nordheim tunneling requires higher bias.

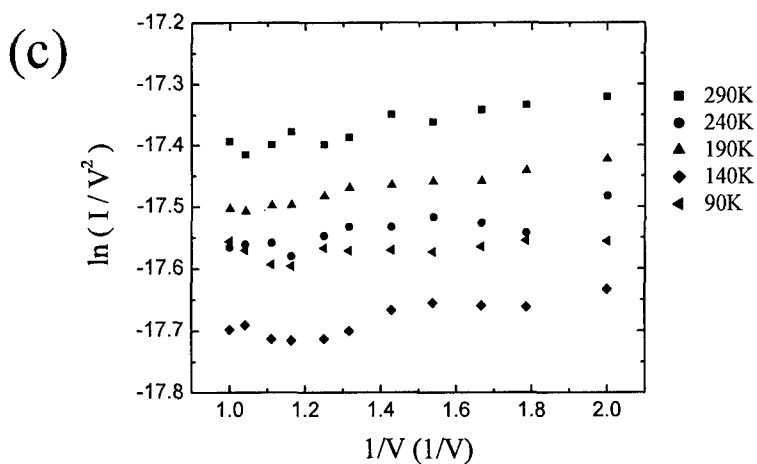
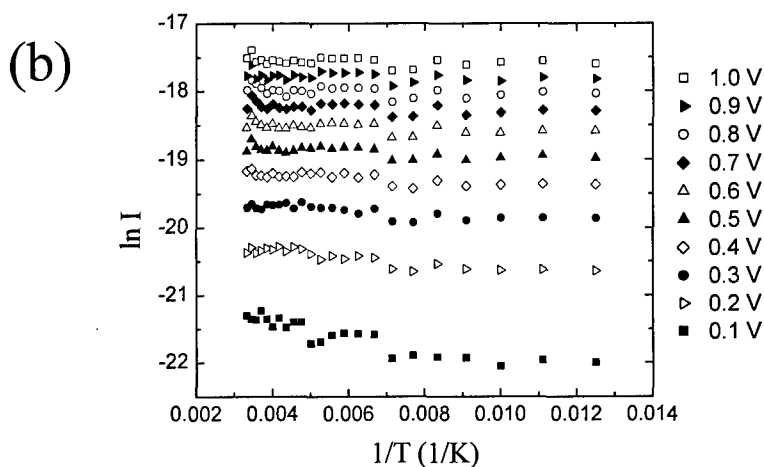
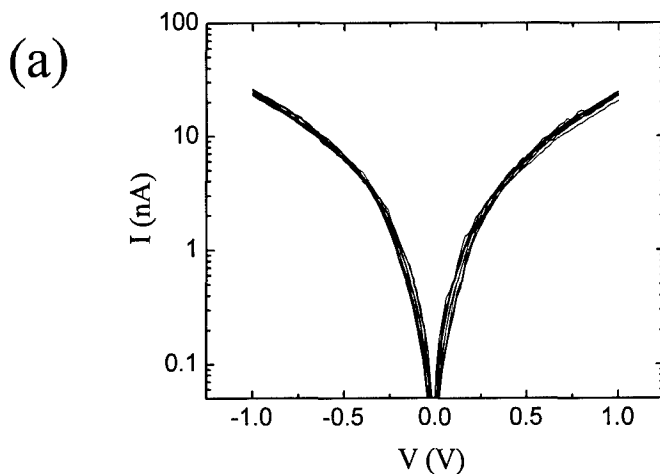


Figure 3. (a) Temperature-dependent  $I(V)$  characteristics of dodecanethiol (C12).  $I(V)$  data at temperatures from 300 to 80 K with 20 K steps are plotted on a log scale. (b) Arrhenius plot generated from the  $I(V)$  data in (a), at voltages from 0.1 to 1.0 Volt with 0.1 Volt steps. (c) Plot of  $\ln(I/V^2)$  versus  $1/V$  at selected temperatures.

The importance of variable temperature measurements to validate tunneling is demonstrated in Figure 4. Here the  $I(V)$  of an octanethiol (C8) device is shown (Figure 4(a)), whose  $I(V)$  shape looks very similar to Figure 3 (i.e., direct tunneling), and indeed can be fit to a Simmons model. However, further  $I(V,T)$  measurements display an obvious temperature dependence (Figure 4(b)), which can be fit well to a hopping

conduction model (Table 1) with a well-defined activation energy of 190 meV (Figure 4(c)). This and other similar impurity-mediated transport phenomena (such as Coulomb blockade) are observed in a subset of devices and is indicative of the unintentional incorporation of a trap or defect level in those devices. This study instead focuses on devices which do not show any defect-mediated transport and probes the intrinsic behavior of the molecular layer.

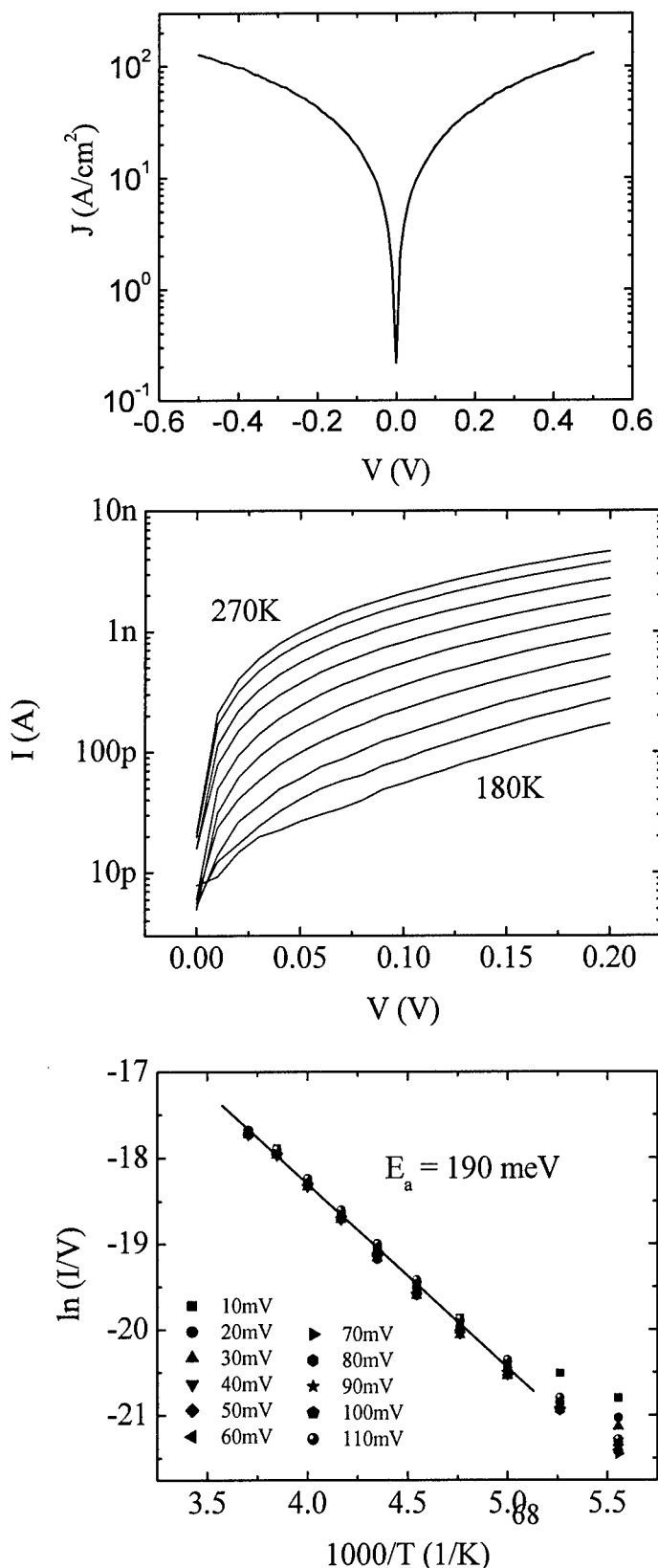


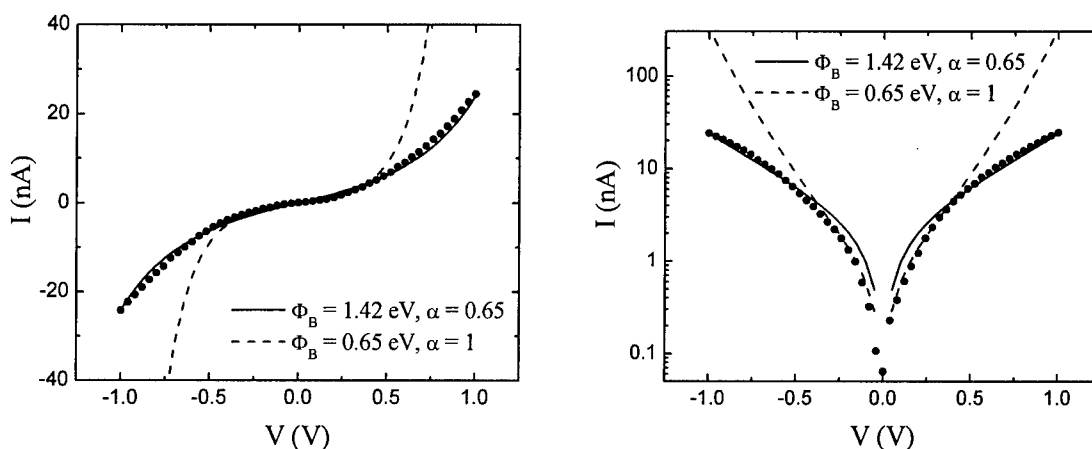
Figure 4. (a)  $I(V)$  characteristics of an octanethiol (C8) device at 270K. (b) Temperature dependence of the device from 270K to 180K (in 10K increments). (c) Plot of  $\ln(I/V)$  versus  $1/T$  at various voltages. The activated behavior is bias voltage independent, thus the behavior is hopping (in this device) due to incorporation of a defect of energy 190 meV. This class of device is not suitable for investigation of the intrinsic transport mechanism in the SAM as it is dominated by a defect.

Having established tunneling as the

conduction mechanism in a device, we will now obtain the barrier height by comparing experimental I(V) data with theoretical calculations from tunneling models.

From the modified Simmons model [Eq. (2)] by adjusting two parameters  $\Phi_B$  and  $\alpha$ , a nonlinear least squares fitting can be performed to fit the measured C12 I(V) data (calculation assuming  $\alpha = 1$  has been previously shown not to fit I(V) data well for some alkanethiol measurements at fixed temperature (300 K)).<sup>25</sup> By using a device size of 45 nm in diameter, the best fitting parameters (minimizing  $\chi^2$ ) for the room temperature C12 I(V) data were found to be  $\Phi_B = 1.42 \pm 0.04$  eV and  $\alpha = 0.65 \pm 0.01$ , where the error ranges of  $\Phi_B$  and  $\alpha$  are dominated by potential device size fluctuations of 2 nm. Likewise, data sets were obtained and fittings were done for octanethiol (C8) and hexadecanethiol (C16), which yielded values  $\{\Phi_B = 1.83 \pm 0.10$  eV and  $\alpha = 0.61 \pm 0.01\}$  and  $\{\Phi_B = 1.40 \pm 0.03$  eV,  $\alpha = 0.68 \pm 0.01\}$ , respectively.

Using  $\Phi_B = 1.42$  eV and  $\alpha = 0.65$ , a calculated I(V) for C12 is plotted as a solid curve in a linear scale [Figure 5(a)] and in a semi-log scale [Figure 5(b)]. A calculated I(V) for  $\alpha = 1$  and  $\Phi_B = 0.65$  eV (which gives the best fit at low bias range) is shown as the dashed curve in the same figure, illustrating that with  $\alpha = 1$  only limited regions of the I(V) can be fit (specifically here, for  $V < 0.3$  Volt). For the case of a rectangular barrier, the  $\alpha$  parameter fit presented above corresponds to an effective mass  $m^*$  ( $= \alpha^2$



m) of 0.42 m.

Figure 5. Measured C12 I(V) data (circular symbols) is compared with calculation (solid curve) using the optimum fitting parameters of  $\Phi_B = 1.42$  eV and  $\alpha = 0.65$ . The calculated I(V) from a simple rectangular model ( $\alpha = 1$ ) with  $\Phi_B = 0.65$  eV is also shown as the dashed curve. Current is plotted (a) on linear scale and (b) on log scale.

In order to investigate the dependency of the Simmons model fitting on  $\Phi_B$  and  $\alpha$ , a fitting minimization analysis was undertaken on the individual  $\Phi_B$  and  $\alpha$  values as well as their product form of  $\alpha\Phi_B^{1/2}$  in Eq. (4a).  $\Delta(\Phi_B, \alpha) = (\sum |I_{\text{exp},V} - I_{\text{cal},V}|^2)^{1/2}$  was calculated and plotted where  $I_{\text{exp},V}$  is the experimental current-voltage values and  $I_{\text{cal},V}$  is calculated using Eq. (2). 7,500 different  $\{\Phi_B, \alpha\}$  pairs were used in the fittings with  $\Phi_B$  ranging from 1.0 to 2.5 eV (0.01 eV increment) and  $\alpha$  from 0.5 to 1.0 (0.01 increment). Figure 6(a) is a representative contour plot of  $\Delta(\Phi_B, \alpha)$  versus  $\Phi_B$  and  $\alpha$  values generated for the C12 I(V) data where darker regions correspond to smaller  $\Delta(\Phi_B, \alpha)$  and various shades represent half order of magnitude  $\Delta(\Phi_B, \alpha)$  steps. The darker regions represent better fits of Eq. (2) to the measured I(V) data. In the inset in Figure 6(a) one can see there is a range of possible  $\Phi_B$  and  $\alpha$  values yielding minimum fitting parameters. Although the tunneling parameters determined from the previous Simmons tunneling fitting  $\{\Phi_B = 1.42 \text{ eV and } \alpha = 0.65\}$  lie within this minimum region in this figure, there is a distribution of other possible values.

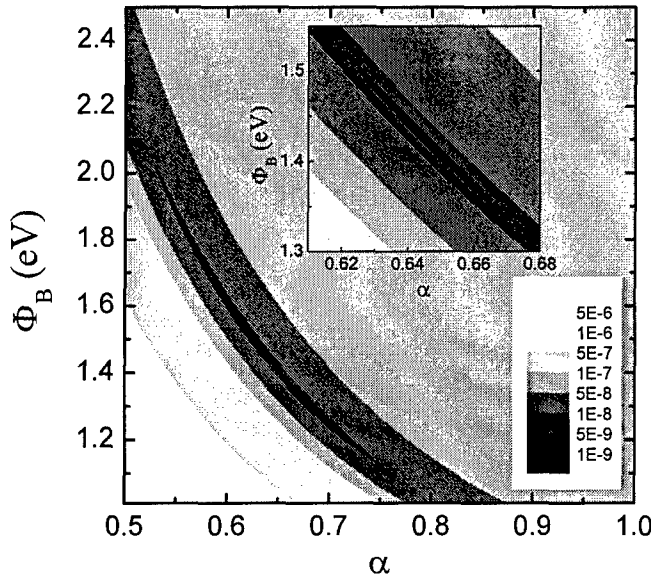
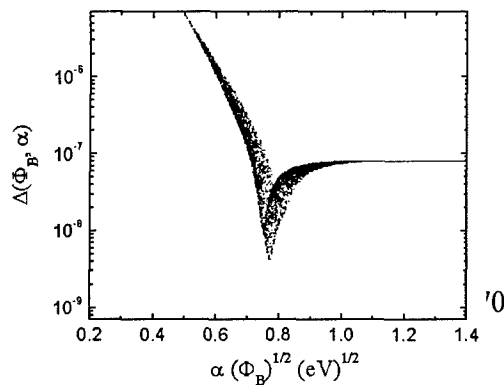


Figure 6. (a) Contour plot of  $\Delta(\Phi_B, \alpha)$  values for C12 nanopore device as a function of  $\Phi_B$  and  $\alpha$ , where the darker region corresponds to a better fitting. Inset shows detailed minimization fitting regions. (b) A plot of  $\Delta(\Phi_B, \alpha)$  as a function of  $\alpha\Phi_B^{1/2}$ .



A plot of  $\Delta(\Phi_B, \alpha)$  versus  $\alpha\Phi_B^{1/2}$  for the same device reveals a more pronounced dependence, and is shown in Figure 6(b). This plot indicates the fitting to the Simmons model sharply depends on the product of  $\alpha\Phi_B^{1/2}$ . For this plot the  $\Delta(\Phi_B, \alpha)$  is minimized at  $\alpha\Phi_B^{1/2}$  of  $0.77 (\text{eV})^{1/2}$

corresponding to a  $\beta_0$  value of  $0.79 \text{ \AA}^{-1}$  from Eq. (4a). The C8 and C16 devices showed similar results, indicating the Simmons tunneling model has a strong  $\alpha\Phi_B^{1/2}$  dependence. For the C8 device, although  $\Phi_B$  obtained from the fitting is a

little larger, combined  $\alpha$  and  $\Phi_B$  gives a similar  $\beta_0$  value within the error range as the C12 and C16 devices (Table 2).

TABLE 2. Summary of alkanethiol tunneling parameters in this study

Molecules	J at 1 V (A/cm <sup>2</sup> )	$\Phi_B$ (eV)	$\alpha$	$m^*$ (m)	$\beta_0$ (Å <sup>-1</sup> )*
C8	31,000 ± 10,000	1.83 ± 0.10	0.61 ± 0.01	0.37	0.85 ± 0.04
C12	1,500 ± 200	1.42 ± 0.04	0.65 ± 0.01	0.42	0.79 ± 0.02
C16	23 ± 2	1.40 ± 0.03	0.68 ± 0.01	0.46	0.82 ± 0.02
C8-dithiol	93,000 ± 18,000	1.20 ± 0.03	0.59 ± 0.01	0.35	0.66 ± 0.02

\*  $\beta_0$  values were calculated using Eq. (4a).

Three alkanethiols of different molecular length, C8, C12, and C16 were investigated to study length-dependent tunneling behavior. Figure 7 is a semi-log plot of tunneling current densities multiplied by molecular length ( $Jd$  at low bias and  $Jd^2$  at high bias) as a function of the molecular length for these alkanethiols. The molecular lengths used in this plot are 13.3, 18.2, and 23.2 Å for C8, C12, and C16, respectively. Each molecular length was determined by adding an Au-thiol bonding length to the length of molecule<sup>22</sup>. Note that these lengths assume through-bond tunneling.<sup>22,23,32,57</sup> The high and low bias regimes are defined somewhat arbitrarily by comparing the relative magnitudes of the first and second exponential terms in Eq. (2). Using  $\Phi_B = 1.42$  eV and  $\alpha = 0.65$  obtained from nonlinear least squares fitting of the C12 I(V) data, the second term becomes less than ~ 10 % of the first term at ~ 0.5 Volt that is chosen as the boundary of low and high bias ranges.

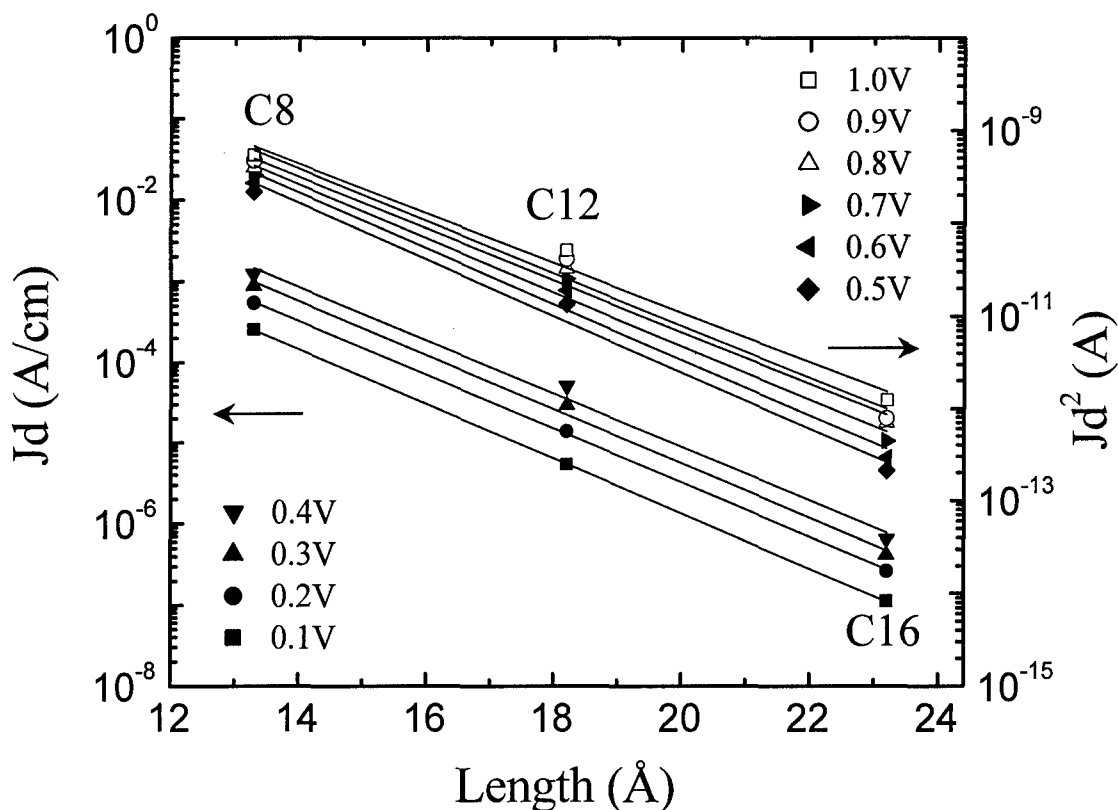


Figure 7. Log plot of tunneling current densities multiplied by molecular length  $d$  at low bias and by  $d^2$  at high bias (symbols) versus molecular lengths. The lines through the data points are linear fittings.

As seen in Figure 7, the tunneling current shows exponential dependence on molecular length, which is consistent with the Simmons tunneling model [Eq. (3)]. The  $\beta$  values can be determined from the slope at each bias and are plotted in Figure 8. The error bar of an individual  $\beta$  value in this plot was obtained by considering both the device size uncertainties and the linear fitting errors.



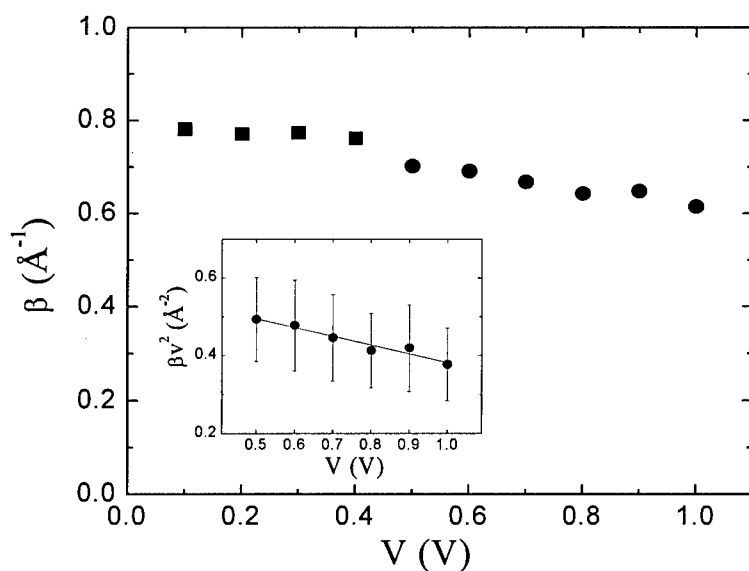


Figure 8. Plot of  $\beta$  versus bias in the low bias range (square symbols) and high bias ranges (circular symbols). The inset shows a plot of  $\beta^2 V$  versus bias with a linear fitting.

The determined  $\beta$  values are almost independent of bias in the low

bias range ( $V < \sim 0.5$  V), and an average  $\beta$  of  $0.77 \pm 0.06 \text{ \AA}^{-1}$  in this region (from 0 to 0.5 V) can be calculated from Figure 8. Table 3 is a summary of previously reported alkanethiol transport parameters obtained by different techniques. The current densities (J) listed in Table 3 are for C12 monothiol or dithiol devices at 1 V, which are extrapolated from published results of other length alkane molecules. The large variation of J of these reports can be attributed to the uncertainties in device contact geometry and junction area, as well as complicating inelastic or defect contributions. The  $\beta$  value ( $0.77 \pm 0.06 \text{ \AA}^{-1} \approx 0.96 \pm 0.08$  per methylene) for alkanethiols reported here is comparable to previously reported values as summarized in Table 3. This  $\beta$  value agrees with the value of  $0.79 \text{ \AA}^{-1}$  ( $\beta_0$ ) calculated via Eq. (4a) from fitting individual I(V) characteristic of the C12 device. The calculated  $\beta_0$  of C8 and C16 devices also have similar values, as summarized in Table 2.

TABLE 3. Summary of alkanethiol tunneling characteristic parameters

Junction	$\beta$ ( $\text{\AA}^{-1}$ )	J ( $\text{A}/\text{cm}^2$ ) at 1 V	$\Phi_B$ (eV)	Technique	Ref.
(bilayer) monothiol	$0.87 \pm 0.1$	$25\text{-}200^{\text{a}}$	$2.1^{\text{e}}$	Hg-junction	25
(bilayer) monothiol	$0.71 \pm 0.08$	$0.7\text{-}3.5^{\text{a}}$		Hg-junction	27
monothiol	$0.79 \pm 0.01$	$1500 \pm 200^{\text{b}}$	$1.4^{\text{e}}$	Solid M-I-M	33
monothiol	1.2			STM	19
dithiol	$0.8 \pm 0.08$	$3.7\text{-}5 \times 10^5^{\text{c}}$	$5 \pm 2^{\text{f}}$	STM	20
monothiol	0.73-0.95	$1100\text{-}1900^{\text{d}}$	$2.2^{\text{e}}$	CAFM	21

monothiol	0.64-0.8	10-50 <sup>d)</sup>	2.3 <sup>e)</sup>	CAFM	23
dithiol	0.46±0.02	3-6 × 10 <sup>5</sup> <sup>e)</sup>	1.3-1.5 <sup>e)</sup>	CAFM	24
monothiol	1.37±0.03		1.8 <sup>d)</sup>	Tuning fork AFM	49
monothiol	0.97±0.04			Electrochemical	30
monothiol	0.85			Electrochemical	31
monothiol	0.91±0.08			Electrochemical	32
monothiol	0.76	2×10 <sup>4</sup> (at 0.1 V) <sup>e)</sup>	1.3-3.4 <sup>e)</sup>	Theory	58
monothiol	0.76			Theory	59
monothiol	0.79			Theory	56

Note:

Some decay coefficients  $\beta$  were converted into the unit of  $\text{\AA}^{-1}$  from the unit of per methylene.

The junction areas were estimated by optical microscope<sup>a)</sup>, SEM<sup>b)</sup>, assuming single molecule<sup>c)</sup>, and Hertzian contact theory<sup>d)</sup>.

Current densities (J) for C12 monothiol or dithiol at 1 V are extrapolated from published results for other length molecules by using conductance  $\propto \exp(-\beta d)$  relationship.

Barrier height  $\Phi_B$  values were obtained from Simmons equation<sup>e)</sup>, bias-dependence of  $\beta^\eta$ , and a theoretical calculation<sup>f)</sup>.

According to Eq. (4b),  $\beta^2_V$  depends on bias V linearly in the high bias range. The inset in Figure 8 is a plot of  $\beta^2_V$  versus V in this range (0.5 to 1.0 Volt) along with linear fitting of the data. From this fitting,  $\Phi_B = 1.35 \pm 0.20$  eV and  $\alpha = 0.66 \pm 0.04$  were obtained from the intercept and the slope, respectively, consistent with the values  $\{\Phi_B = 1.42$  eV and  $\alpha = 0.65\}$  obtained from the nonlinear least squares fitting in the previous section.

$\beta$  values for alkanethiols obtained by various experimental techniques have previously been reported and are summarized in Table 3.<sup>19-33,49</sup> In order to compare with these reported  $\beta$  values, we also performed length-dependent analysis on our experimental data according to the generally used equation:<sup>20-28,33</sup>

$$G = G_0 \exp(-\beta d) \quad (5)$$

This gives a  $\beta$  value from 0.84 to 0.73  $\text{\AA}^{-1}$  in the bias range from 0.1 to 1.0 volt, which is comparable to results reported previously. For example, Holmlin, *et. al*, reported a  $\beta$  value of 0.87  $\text{\AA}^{-1}$  by mercury drop experiments,<sup>25</sup> and Wold, *et. al*, have reported  $\beta$  of 0.94  $\text{\AA}^{-1}$  and Cui, *et. al*, reported  $\beta$  of 0.64  $\text{\AA}^{-1}$  for various alkanethiols by using a conducting atomic force microscope technique.<sup>21,23</sup> These reported  $\beta$  were treated as bias-independent quantities, contrary to the results reported here and that observed in a slightly different alkane system (ligand-encapsulated nanoparticle/alkane-dithiol molecules).<sup>24</sup> We also caution against the use of parameters that have not been checked with a temperature-dependent analysis, since small non-tunneling components can dramatically affect derived values of  $\beta$ .

We have analyzed our experimental data using a Franz two-band model.<sup>50-53</sup> Since there is no reliable experimental data on the Fermi level alignment in these metal-SAM-metal systems,  $\Phi_B$  and  $m^*$  are treated as adjustable parameters. We performed a least squares fit on our data with the Franz non-parabolic  $E(k)$  relationship [Eq. (1)] using an alkanethiol HOMO-LUMO gap of 8 eV.<sup>12,13</sup> Figure 9 shows the resultant  $E(k)$  relationship and the corresponding energy band diagrams. The zero of energy in this plot was chosen as the LUMO energy. The best fitting parameters obtained by minimizing  $\chi^2$  were  $\Phi_B = 1.49 \pm 0.51$  eV and  $m^* = 0.43 \pm 0.15$  m, where the error ranges of  $\Phi_B$  and  $m^*$  are dominated by the error fluctuations of  $\beta$  [ $k^2 = -(\beta/2)^2$ ]. Both electron tunneling near the LUMO and hole tunneling near the HOMO can be described by these parameters.  $\Phi_B$

$= 1.49$  eV indicates that the Fermi level is aligned close to one energy level in either case, therefore the Simmons model is a valid approximation. The  $\Phi_B$  and  $m^*$  values obtained here are in reasonable agreement with the previous results obtained from the Simmons model.

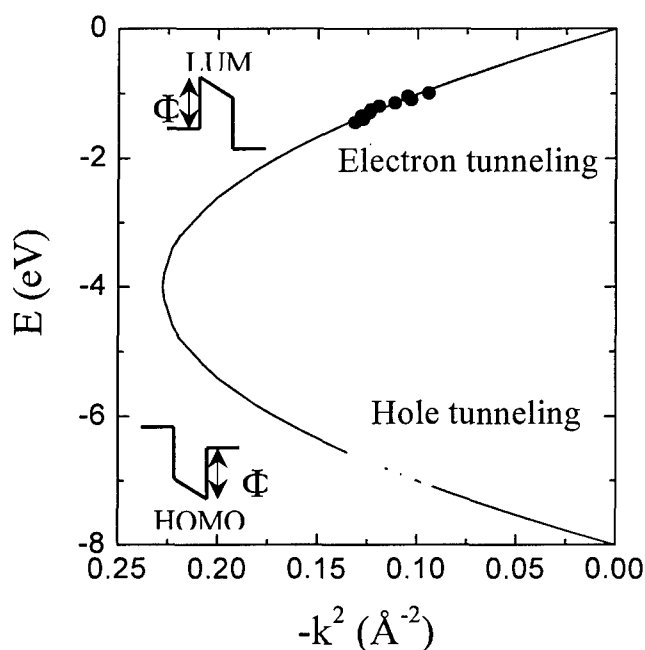


Figure 9.  $E(k)$  relationship (symbols) generated from the length-dependent measurement data for alkanethiols. Solid and open symbols correspond to electron and hole tunneling, respectively. The insets show the corresponding energy band diagrams. The solid curve is the Franz two-band

expression for  $m^* = 0.43$  m.

Electronic transport through alkanethiol SAMs is further investigated with the technique of inelastic electron tunneling spectroscopy,<sup>34</sup> such as the works of 1966 by Jaklevic and Lambe who studied the conductance of a tunnel junctions with encased organic molecules.<sup>35</sup> Since then it has become a powerful spectroscopic tool for chemical identification, chemical bonding investigation, and surface chemistry and physics studies.<sup>38</sup> In an inelastic tunneling process the electron loses energy to a localized vibrational mode with a frequency  $\nu$  when the applied bias satisfies the condition of  $eV =$

hv. As a result, an additional tunneling channel is opened for the electron, resulting in an increase in the total current at the applied bias corresponding to the vibrational mode energy.<sup>37</sup> Typically only a small fraction of tunneling electrons are involved in the inelastic tunneling process (determined by the electron – vibronic mode coupling coefficient), resulting in a small conductance change, which is commonly measured in the second harmonics of a phase-sensitive detector that yields the characteristic frequencies of the corresponding vibrational modes as well as other information.<sup>36-38</sup>

I(V,T) measurements and additional IETS studies have been performed on an octanedithiol (C8-dithiol) SAM using the aforementioned device structure shown in Figure 1(a).<sup>34</sup> Figure 10(a) is the I(V,T) data for this device obtained from 300 to 4.2 K. An Arrhenius plot shown in Figure 10(b) exhibits little temperature dependence, verifying that tunneling is the main transport mechanism for C8-dithiol SAM. This result is in good agreement with the tunneling transport characteristics observed previously. Figure 10(c) shows the room temperature I(V) measurement result. Using a junction area of  $51 \pm 5$  nm in diameter (obtained from statistical studies of the nanopore size with SEM), a current density of  $(9.3 \pm 1.8) \times 10^4$  A/cm<sup>2</sup> at 1.0 Volt is calculated. As a comparison, the current density of  $(3.1 \pm 1.0) \times 10^4$  A/cm<sup>2</sup> at 1.0 Volt was observed for C8 monothiol SAM. Using the modified Simmons model [Eq. (2)], the transport parameters of  $\Phi_B = 1.20 \pm 0.03$  eV and  $\alpha = 0.59 \pm 0.01$  ( $m^* = 0.34 m$ ) were obtained for this C8-dithiol SAM.

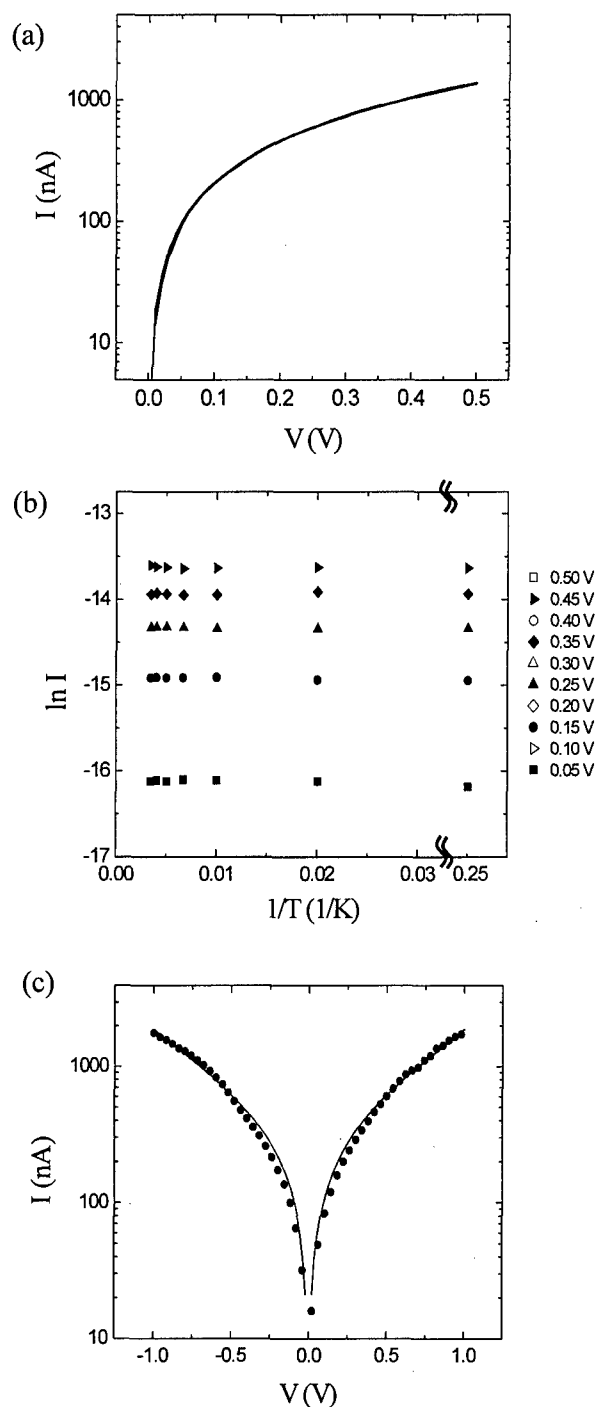


Figure 10. (a) I(V,T) characteristics of C8 dithiol SAM at selected temperatures (4.2, 50, 100, 150, 200, 250, and 290 K). (b) Arrhenius plot generated from the data in (a), at voltages from 0.1 to 0.5 Volt with 0.05 Volt steps. (c) Measured C8-dithiol I(V) data at room temperature (circular symbols) is compared with calculation (solid

curve) using the optimum fitting parameters of  $\Phi_B = 1.20$  eV and  $\alpha = 0.59$ .

Figure 11 shows the IETS spectrum of the same C8-dithiol SAM device obtained at  $T = 4.2$  K. An ac modulation of 8.7 mV (rms value) at a frequency of 503 Hz was applied to the sample to acquire the second harmonic signals. The spectra are stable and repeatable upon successive bias sweeps. The spectrum at 4.2 K is characterized by three pronounced peaks in the 0 to 200 mV region at 33, 133, and 158 mV. From comparison with previously reported infrared (IR), Raman, and high resolution electron energy loss (HREEL) spectra of SAM covered gold surfaces (Table 4), these three peaks are assigned to  $\nu(\text{Au-S})$ ,  $\nu(\text{C-C})$ , and  $\gamma_w(\text{CH}_2)$  modes of a surface bound alkanethiolate.<sup>60-63</sup> The absence of a strong  $\nu(\text{S-H})$  signal at  $\sim 329$  mV suggests that most of the thiol groups have reacted with the gold bottom and top contacts. Peaks are also reproducibly observed at 80, 107 mV, and 186 mV. They correspond to  $\nu(\text{C-S})$ ,  $\delta_r(\text{CH}_2)$ , and  $\delta_s(\text{CH}_2)$  modes. The stretching mode of the  $\text{CH}_2$  groups,  $\nu(\text{CH}_2)$ , appears as a shoulder at 357 meV. The peak at 15 mV is due to vibrations from either Si, Au, or  $\delta(\text{C-C-C})$ .<sup>64</sup> We note that all alkanethiolate peaks without exception or omission occur in the spectra. Peaks at 58, 257, 277, and 302, as well as above 375 mV are likely to originate from Si-H and N-H vibrations related to the silicon nitride membrane,<sup>64a,65</sup> which forms the SAM encasement. To the best of our knowledge alkanethiols have no vibrational signatures in these regions. Measurement of the background spectrum of an “empty” nanopore device with only gold contacts to obtain background contributions from  $\text{Si}_3\text{N}_4$  is hampered by either too low (open circuit) or too high (short circuit) currents in such a device. Similar IETS result has also been obtained using a different test structure recently.<sup>66</sup>

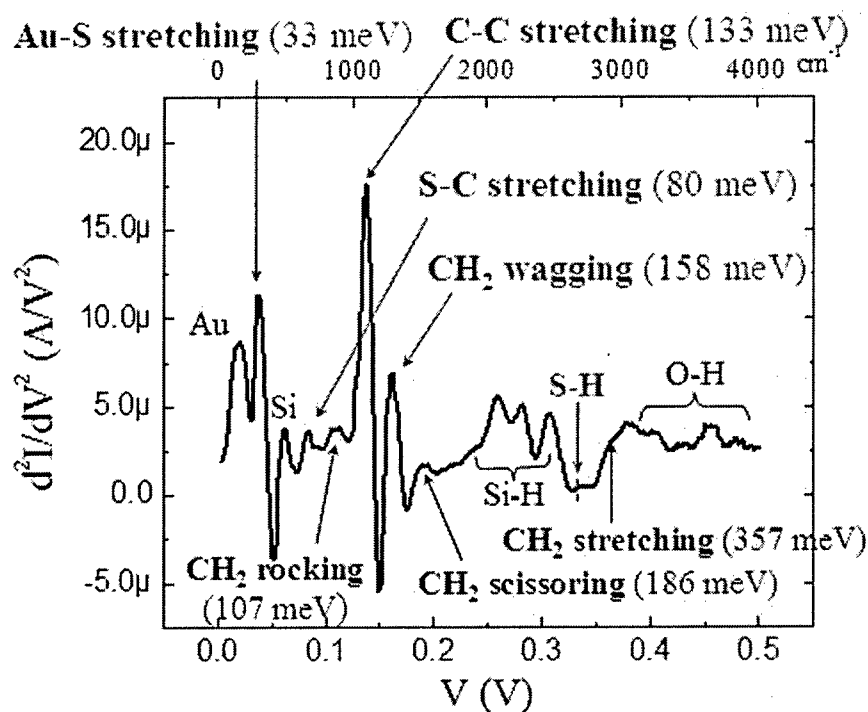


Figure 11. Inelastic electron tunneling spectrum of C8 dithiol SAM obtained from lock-in second harmonic measurement with an ac modulation of 8.7 mV (rms value) at a frequency of 503 Hz ( $T = 4.2$  K). Peaks labeled with Si are most probably background due to the encasing  $\text{Si}_3\text{N}_4$ .

TABLE 4: Summary\* of the major vibrational modes of alkanethiolates. Taken from Ref. 60-62.

Modes	Methods	Wavenumber ( $\text{cm}^{-1}$ )	(meV)
$\nu(\text{Au-S})$	HREELS <sup>61</sup>	225	28
	Raman <sup>60</sup>	641	79
	Raman <sup>60</sup>	706	88
	HREEL <sup>61</sup>	715	89
	IR <sup>62</sup>	720	89
	IR <sup>62</sup>	766	95
	IR <sup>62</sup>	925	115
	HREEL <sup>61</sup>	1050	130

$\nu(\text{C-C})$	Raman <sup>60</sup>	1064	132
	Raman <sup>60</sup>	1120	139
	IR <sup>62</sup>	1230	152
	HREELS <sup>61</sup>	1265	157
	IR <sup>62</sup>	1283	159
IR <sup>62</sup>		1330	165
$\delta_s(\text{CH}_2)$	HREELS <sup>61</sup>	1455	180
$\nu(\text{S-H})$	Raman <sup>60</sup>	2575	319
	Raman <sup>60</sup>	2854	354
HREELS <sup>61</sup>		2860	355
Raman <sup>60</sup>		2880	357
Raman <sup>60</sup>		2907	360
HREELS <sup>61</sup>		2925	363

\* There is a vast amount of literature with spectroscopic assignments for alkanethiols. The references given are representative for IR, Raman, and HREELS assignments.

Although there are no selection rules in IETS as there are in IR and Raman spectroscopy, certain selection preferences have been established. According to the IETS theory,<sup>67</sup> molecular vibrations with net dipole moments perpendicular to the interface of the tunneling junction have stronger peak intensities than vibrations with net dipole moments parallel to the interface (for dipoles close to the electrodes). Thus vibrations perpendicular to the electrode interface, i.e.,  $\nu(\text{Au-S})$ ,  $\nu(\text{C-S})$ ,  $\nu(\text{C-C})$ , and  $\gamma_w(\text{CH}_2)$ , dominate the IETS spectrum while modes parallel to the interface, i.e.,  $\delta_{r,s}(\text{CH}_2)$  and  $\nu(\text{CH}_2)$ , are weak, as clearly shown in Figure 11.

In order to verify that the observed spectra are indeed valid IETS data, the peak width broadening was examined as a function of temperature and modulation voltage. IETS was performed with different ac modulations at a fixed temperature, and at different temperatures with a fixed ac modulation. Figure 12(a) shows the modulation dependence of the IETS spectra obtained at 4.2 K, and Figure 12(b) shows the modulation broadening of the C-C stretching mode at 133 meV. The circular symbols are the full widths at half maximum (FWHMs) of the experimental peak at  $T = 4.2$  K with various modulation voltages. A Gaussian distribution function was utilized to obtain a FWHM and the error range.<sup>68</sup> The square symbols are calculated FWHM values ( $W_{\text{theoretical}}$ ) taking into account both a finite temperature effect ( $W_{\text{thermal}} \sim 5.4 \text{ k}_B T$ )<sup>36</sup> and a finite voltage modulation effect ( $W_{\text{modulation}} \sim 1.7 V_{\text{ac-rms}}$ ).<sup>69</sup> These two broadening contributions add as the squares:  $W_{\text{theoretical}}^2 = W_{\text{thermal}}^2 + W_{\text{modulation}}^2$ . The agreement is excellent over most of the

modulation range, but we note a saturation of the linewidth at low modulation bias indicating the influence of a non-negligible intrinsic linewidth. Taking into account the known thermal and modulation broadenings, and including the intrinsic linewidth ( $W_I$ )<sup>70</sup> as a fitting parameter, the measured peak width ( $W_{exp}$ ) is given by

$$W_{exp} = \sqrt{W_I^2 + W_{thermal}^2 + W_{modulation}^2} \quad (6)$$

$W_I$  can be determined by using a nonlinear least squares fit to the ac modulation data (Figure 12) with Eq. (6), giving an intrinsic linewidth of  $3.73 \pm 0.98$  meV for this line. This is shown (with the error range) in Figure 12(b) as a shaded bar, including the thermal contribution.

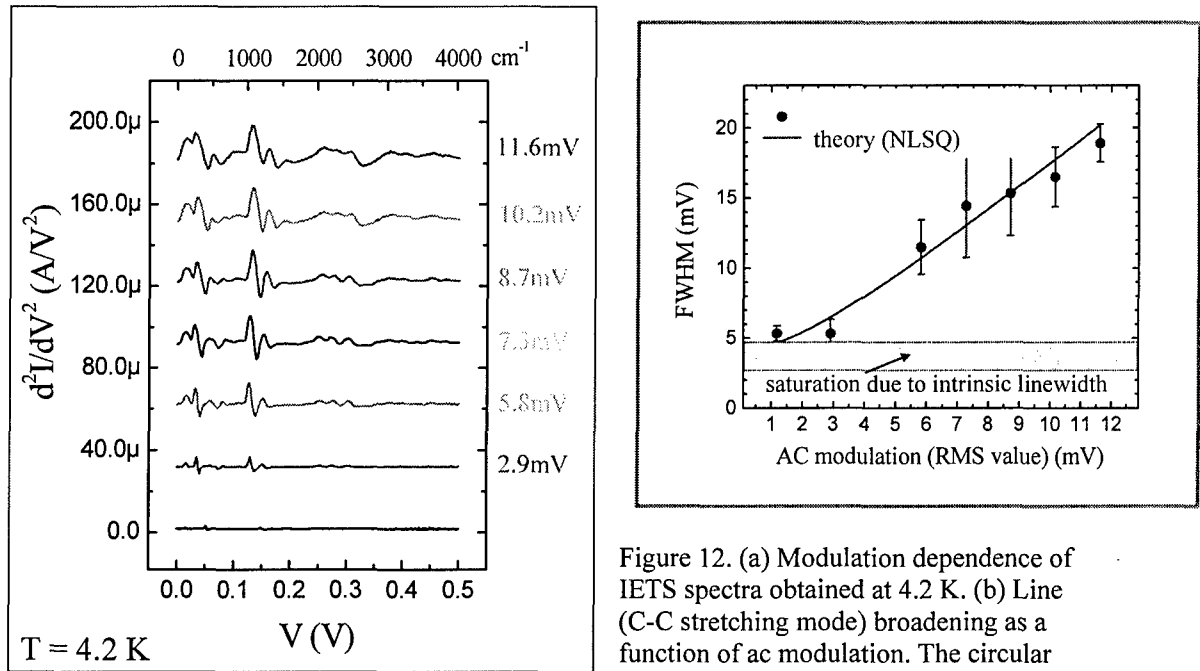


Figure 12. (a) Modulation dependence of IETS spectra obtained at 4.2 K. (b) Line (C-C stretching mode) broadening as a function of ac modulation. The circular symbols are experimental FWHMs and the square symbols are theoretical

calculations considering both modulation and thermal contributions. The shaded bar denotes the expected saturation due to the derived intrinsic linewidth (including a  $5.4 k_B T$  thermal contribution) of  $3.73 \pm 0.98$  meV.

We can independently check the thermal broadening of the line at fixed modulation. Figure 13(a) shows the temperature dependence of the IETS spectra obtained with an ac modulation of 8.7 mV (rms value). In Figure 13(b) the circular symbols (and corresponding error bars) are experimental FWHM values of the C-C stretching mode from Figure 13(a), determined by a Gaussian fit (and error of the fit) to the experimental lineshape. For simplicity we have only considered Gaussian lineshapes<sup>68</sup> resulting in increased error bars for the lower temperature range due to an asymmetric lineshape. The square symbols are theoretical calculations considering thermal broadening, modulation



broadening, and the intrinsic linewidth determined above. The error ranges of the calculation (due to the intrinsic linewidth error) are approximately the size of the data points. The agreement between theory and experiment is very good, spanning a

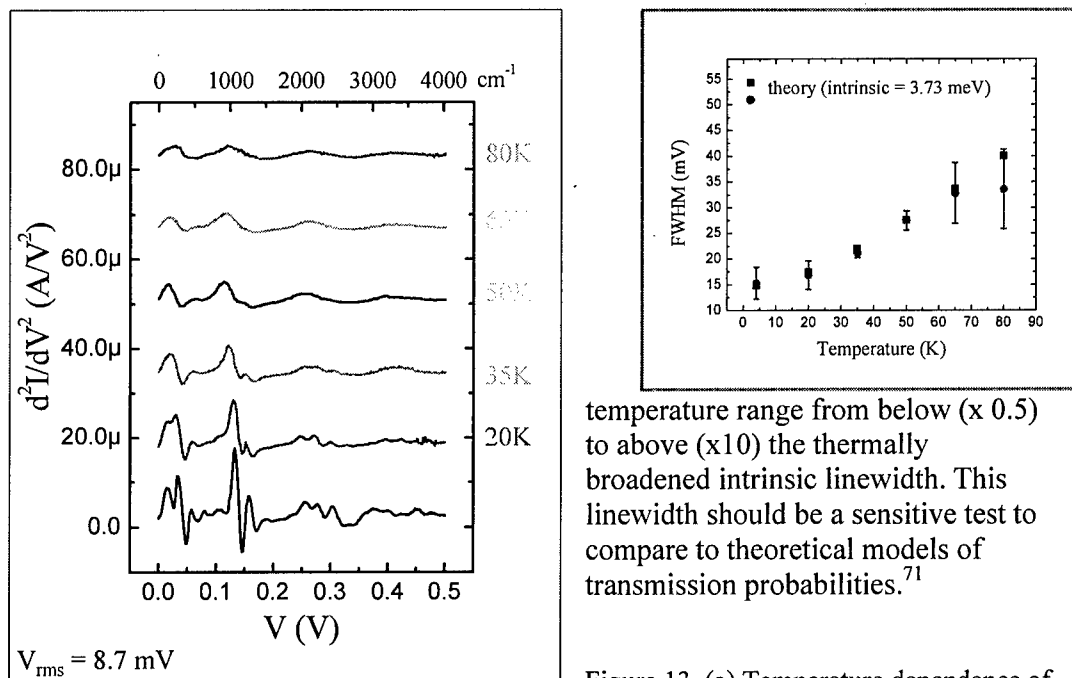
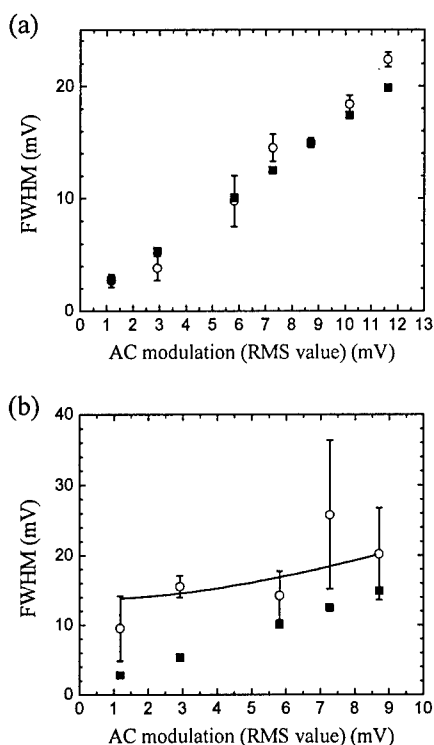


Figure 13. (a) Temperature dependence of IETS spectra obtained at a fixed ac modulation of 8.7 mV (rms value). (b) Line (C-C stretching mode) broadening as a function of temperature. The circular symbols are experimental FWHMs and the square symbols are theoretical calculations considering thermal broadening, modulation broadening, and the intrinsic linewidth. .



Similar intrinsic linewidths have been determined for the Au-S stretching mode (33 meV) and the CH<sub>2</sub> wagging mode (158 meV), and the results are shown in Figure. 14. For the Au-S stretching mode, the deviation of experimental data from calculated values (thermal and modulation width only) is little (Fig. 14(a)), indicating that its intrinsic linewidth is small. A linewidth upper limit of 1.69 meV is determined for this vibrational mode. For the CH<sub>2</sub> wagging mode, a nonlinear least squares fit to Eq. (6) (solid curve in Fig. 14(b)) gave an intrinsic linewidth of  $13.5 \pm 2.4$  meV. The linewidths and their variation throughout the molecule are potentially due to inhomogeneous configuration of the molecular constituents, and a more detailed understanding

may give detailed structural information of these device structures.

Figure. 14. Line broadenings as function of AC modulation for IETS spectra obtained at 4.2 K for (a) the Au-S stretching mode and (b) the CH<sub>2</sub> wagging mode. The circular symbols are experimental FWHMs and the square symbols are theoretical calculations considering modulation and thermal contributions. Nonlinear least squares fitting to determine intrinsic linewidth is shown as the solid curve in (b). The intrinsic linewidths obtained for the Au-S stretching mode is  $< 1.69$  meV, and for the CH<sub>2</sub> wagging mode is  $13.5 \pm 2.4$  meV.

## References

1. Reed, M. A.; Tour, J. M. *Scientific American* **2000**, June 86-93.
2. Reed, M. A.; Zhou, C.; Muller, C. J.; Burgin, T. P.; Tour, J. M. *Science* **1997**, 278, 252-254.
3. Reed, M. A.; Lee, T. Eds. *Molecular Nanoelectronics*; American Scientific Publishers: Stevenson Ranch, 2003.
4. (a) Heath, J. R.; Ratner, M. A. *Physics Today* **2003**, May 43-49. (b) Nitzan, A.; Ratner, M. A. *Science* **2003**, 300, 1384-1389.
5. (a) Chen, Y.; Jung, G.-Y.; Ohlberg, D. A. A.; Li, X.; Stewart, D. R.; Jeppesen, J. O.; Nielsen, K. A.; Stoddart, J. F.; Williams, R. S. *Nanotechnology*, **2003**, 14, 462-468. (b) Beyond Silicon: Breakthroughs in Molecular Electronics, <http://www.hpl.hp.com/research/qsr/> (Hewlett-Packard Quantum Science Research)
6. (a) Luo, Y.; Collier, C. P.; Jeppesen, J. O.; Nielsen, K. A.; DeIonno, E.; Ho, G.; Perkins, J.; Tseng, H.-R.; Yamamoto, T.; Stoddart, J. F.; Heath, J. R. *Chem. Phys. Chem.* **2002**, 3, 519-525. (b) Collier, C. P.; Mattersteig, G.; Wong, E. W.; Luo, Y.; Beverly, K.; Sampaio, J.; Raymo, F. M.; Stoddart, J. F.; Heath, J. R. *Science* **2000**, 289, 1172-1175.
7. (a) Stewart, D. R.; Ohlberg, D. A. A.; Beck, P. A.; Chen, Y.; Williams, R. S.; Jeppesen, J. O.; Nielsen, K. A.; Stoddart, J. F. *Nano Lett.* **2004**, 4, 133-136. (b) Lau, C. N.; Stewart, D. R.; Williams, R. S.; Bockrath, M. *Nano Lett.* **2004**, 4, 569-572.
8. Lee, T.; Wang, W.; Klemic, J. F.; Zhang, J. J.; Su, J.; Reed, M. A. *J. Phys. Chem. B* **2004**, 108, 8742-8750.
9. Ulman, A. *An Introduction to Ultrathin Organic Films from Langmuir-Blodgett to Self-Assembly*; Academic Press: Boston, 1991.
10. Poirier, G. E. *Chem. Rev.* **1997**, 97, 1117-1127.
11. Ratner, M. A.; Davis, B.; Kemp, M.; Mujica, V.; Roitberg, A.; Yaliraki, S. in *Molecular Electronics: Science and Technology, The Annals of the New York Academy of Sciences*, Aviram, A.; Ratner, M. Eds.; The New York Academy of Sciences: Vol. 852, New York, 1998.
12. Although the HOMO-LUMO gap of alkyl chain type molecules has been reported (see ref 13), there is no experimental data on the HOMO-LUMO gap for Au/alkanethiol SAM/Au system. 8 eV is commonly used as HOMO-LUMO gap of alkanethiol.
13. (a) Boulas, C.; Davidovits, J. V.; Rondelez, F.; Vuillaume, D. *Phys. Rev. Lett.* **1996**, 76, 4797-4800. (b) Fujihira, M.; Inokuchi, H. *Chem. Phys. Lett.* **1972**, 17, 554-556. (c) Lias, S. G.; Bartmess, J. E.; Liebman, J. F.; Holmes, J. L.; Levin, R. D.; Mallard, W. G. *Gas-Phase Ion and Neutral Thermochemistry, J. Phys. Chem. Ref. Data*, **1998**, 17(1), 24. (d) Yang, H.-H.; McCreery, R. L. *Anal. Chem.* **1999**, 71, 4081.
14. Walczak, M. W.; Chung, C.; Stole, S. M.; Widrig, C. A.; Porter, M. D. *J. Am. Chem. Soc.* **1991**, 113, 2370-2378.
15. Nuzzo, R. G.; Zegarski, B. R.; Dubois, L. H. *J. Am. Chem. Soc.* **1987**, 109, 733-740.
16. Widrig, C. A.; Chung, C.; Porter, M. D. *J. Electroanal. Chem.* **1991**, 310, 335-359.
17. Poirier, G. E.; Tarlov, M. J. *Langmuir* **1994**, 10, 2853-2856.
18. Porter, M. D.; Bright, T. B.; Allara, D. L.; Chidsey, C. E. D. *J. Am. Chem. Soc.* **1987**, 109, 3559-3568.
19. Bumm, L. A.; Arnold, J. J.; Dunbar, T. D.; Allara, D. L.; Weiss, P. S. *J. Phys. Chem. B* **1999**, 103, 8122-8127.
20. Xu, B.; Tao, N. J. *Science* **2003**, 301, 1221-1223.

21. Wold, D. J.; Frisbie, C. D. *J. Am. Chem. Soc.* **2001**, *123*, 5549-5556.
22. Wold, D. J.; Haag, R.; Rampi, M. A.; Frisbie, C. D. *J. Phys. Chem. B* **2002**, *106*, 2813-2816.
23. Cui, X. D.; Zarate, X.; Tomfohr, J.; Sankey, O. F.; Primak, A.; Moore, A. L.; Moore, T. A.; Gust, D.; Harris, G.; Lindsay, S. M. *Nanotechnology* **2002**, *13*, 5-14.
24. Cui, X. D.; Primak, A.; Zarate, X.; Tomfohr, J.; Sankey, O. F.; Moore, A. L.; Moore, T. A.; Gust, D.; Nagahara, L. A.; Lindsay, S. M. *J. Phys. Chem. B* **2002**, *106*, 8609-8614.
25. Holmlin, R.; Haag, R.; Chabinyc, M. L.; Ismagilov, R. F.; Cohen, A. E.; Terfort, A.; Rampi, M. A.; Whitesides, G. M. *J. Am. Chem. Soc.* **2001**, *123*, 5075-5085.
26. Rampi, M. A.; Whitesides, G. M. *Chem. Phys.* **2002**, *281*, 373-391.
27. Slowinski, K.; Fong, H. K. Y.; Majda, M. *J. Am. Chem. Soc.* **1999**, *121*, 7257-7261.
28. York, R. L.; Nguyen, P. T.; Slowinski, K. *J. Am. Chem. Soc.* **2003**, *125*, 5948-5953.
29. Kushmerick, J. G.; Holt, D. B.; Pollack, S. K.; Ratner, M. A.; Yang, J. C.; Schull, T. L.; Naciri, J.; Moore, M. H.; Shashidhar, R. *J. Am. Chem. Soc.* **2002**, *124*, 10654-10655.
30. Smalley, J. F.; Feldberg, S. W.; Chidsey, C. E. D.; Linford, M. R.; Newton, M. D.; Liu, Y. *J. Phys. Chem.* **1995**, *99*, 13141-13149.
31. Weber, K.; Hockett, L.; Creager, S. *J. Phys. Chem. B* **1997**, *101*, 8286-8291.
32. Slowinski, K.; Chamberlain, R. V.; Miller, C. J.; Majda, M. *J. Am. Chem. Soc.* **1997**, *119*, 11910-11919.
33. Wang, W.; Lee, T.; Reed, M. A. *Phys. Rev. B* **2003**, *68*, 035416.
34. Wang, W.; Lee, T.; Kretzschmar, I.; Reed, M. A. *Nano Lett.* **2004**, *4*, 643-646.
35. Jaklevic, R. C.; Lambe, J. *Phys. Rev. Lett.* **1966**, *17*, 1139-1140.
36. Lambe, J.; Jaklevic, R. C. *Phys. Rev.* **1968**, *165*, 821-832.
37. Adkins, C. J.; Phillips, W. A. *J. Phys. C: Solid State Phys.* **1985**, *18*, 1313-1346.
38. Hansma, P.K., Ed. *Tunneling Spectroscopy: Capabilities, Applications, and New Techniques*; Plenum: New York, 1982.
39. Stipe, B. C.; Rezaei, M. A.; Ho, W. *Science* **1998**, *280*, 1732-1735.
40. Zhou, C.; Deshpande, M. R.; Reed, M. A.; Jones II, L.; Tour, J. M. *Appl. Phys. Lett.* **1997**, *71*, 611-613.
41. (a) Chen, J.; Reed, M. A.; Rawlett, A. M.; Tour, J. M. *Science* **1999**, *286*, 1550-1552. (b) Chen, J.; Calvet, L. C.; Reed, M. A.; Carr, D. W.; Grubisha, D. S.; Bennett, D. W. *Chem. Phys. Lett.* **1999**, *313*, 741-748.
42. Ralls, K. S.; Buhrman, R. A.; Tiberio, R. C. *Appl. Phys. Lett.* **1989**, *55*, 2459-2461.
43. Ethanol and alkane molecules were purchased from Sigma-Aldrich.
44. Metzger, R. M.; Chen, B.; Holpfner, U.; Lakshmikantham, M. V.; Vuillaume, D.; Kawai, T.; Wu, X.; Tachibana, H.; Hughes, T. V.; Sakurai, H.; Baldwin, J. W.; Hosch, C.; Cava, M. P.; Brehmer, L.; Ashwell, G. J. *J. Am. Chem. Soc.* **1997**, *119*, 10455-10466.
45. Horowitz, P.; Hill, W. *The Art of Electronics*; Cambridge University Press: New York, 1989.
46. Sze, S. M. *Physics of Semiconductor Devices*; Wiley: New York, 1981.
47. (a) Thurstans, R. E.; Oxley, D. P. *J. Phys. D: Appl. Phys.* **2002**, *35*, 802-809. (b) Simmons, J. G.; Verderber, R. R. *Prof. Roy. Soc. A* **1967**, *301*, 77-102. (c) Dearnaley, G.; Stoneham, A. M.; Morgan, D. V. *Rep. Prog. Phys.* **1970**, *33*, 1129-1191.
48. (a) Mann, B.; Kuhn, H. *J. Appl. Phys.* **1971**, *42*, 4398-4405. (b) Polymeropoulos, E. E.; Sagiv, J. *J. Chem. Phys.* **1978**, *69*, 1836-1847.

49. Fan, F. F.; Yang, J.; Cai, L.; Price, D. W.; Dirk, S. M.; Kosynkin, D. V.; Yao, Y.; Rawlett, A. M.; Tour, J. M.; Bard, A. J. *J. Am. Chem. Soc.* **2002**, *124*, 5550-5560.
50. Franz, W. in *Handbuch der Physik*, edited by Flugge, S; Springer-Verlag: Berlin, 1956, Vol. 17, p. 155.
51. (a) Lewicki, G.; Mead, C. A. *Phys. Rev. Lett.* **1966**, *16*, 939-941. (b) Stratton, R.; Lewicki, G.; Mead, C. A. *J. Phys. Chem. Solids.* **1966**, *27*, 1599-1604. (c) Parker, G. H.; Mead, C. A. *Phys. Rev. Lett.* **1968**, *21*, 605-607.
52. Brar, B.; Wilk, G. D.; Seabaugh, A. C. *Appl. Phys. Lett.* **1996**, *69*, 2728-2730.
53. Joachim, C.; Magoga, M. *Chem. Phys.* **2002**, *281*, 347-352.
54. Simmons, J. G. *J. Appl. Phys.* **1963**, *34*, 1793-1803.
55. (a) Simmons, J. G. *J. Phys. D* **1971**, *4*, 613-657. (b) Maserjian, J.; Petersson, G. P. *Appl. Phys. Lett.* **1974**, *25*, 50-52.
56. Tomfohr, J. K.; Sankey, O. F. *Phys. Rev. B* **2002**, *65*, 245105.
57. (a) Yamamoto, H.; Waldeck, D. H. *J. Phys. Chem. B* **2002**, *106*, 7469-7473. (b) Napper, A. M.; Liu, Haiying.; Waldeck, D. H. *J. Phys. Chem. B* **2001**, *105*, 7699-7707.
58. Kaun, C.-C.; Guo, H. *Nano Lett.* **2003**, *3*, 1521-1525.
59. Piccinin, S.; Selloni, A.; Scandolo, S.; Car, R.; Scoles, G. *J. Chem. Phys.* **2003**, *119*, 6729-6735.
60. Bryant, M. A.; Pemberton, J. E. *J. Am. Chem. Soc.* **1991**, *113*, 8284-8293.
61. Kato, H. S.; Noh, J.; Hara, M.; Kawai, M. *J. Phys. Chem. B* **2002**, *106*, 9655-9658.
62. Castiglioni, C.; Gussoni, M.; Zerbi, G. *J. Chem. Phys.* **1991**, *95*, 7144-7149.
63. The symbols  $\delta$ ,  $\gamma$ , and  $\nu$  denote in-plane rocking (r) and scissoring (s), out-of-plane wagging (w) and twisting (t), and stretching modes, respectively.
64. a) Molinari, M.; Rinnert, H.; Vergnat, M.; Weisbecker, P. *Mat. Sci. Eng. B* **2003**, *101*, 186. b) Bogdanoff, P. D.; Fultz, B.; Rosenkranz, S. *Phys. Rev. B* **1999**, *60*, 3976-3981. c) Mazur, U.; Hipps, K. W. *J. Phys. Chem.* **1982**, *86*, 2854-2860.
65. a) Mazur, U.; Hipps, K. W. *J. Phys. Chem.* **1981**, *85*, 2244-2249. b) Kurata, H.; Hirose, M.; Osaka, Y. *Jap. J. Appl. Phys.* **1981**, *20*, L811.
66. Kushmerick, J. G.; Lazorcik, J.; Patterson, C. H.; Shashidhar, R.; Seferos, D. S.; Bazan, G. C. *Nano Lett.* **2004**, *4*, 639-642.
67. Kirtley, J.; Hall, J. T. *Phys. Rev. B* **1980**, *22*, 848-856.
68. Lauhon, I. J.; Ho, W. *Phys. Rev. B* **1999**, *60*, R8525-R8528.
69. Klein, J.; Léger, A.; Belin, M.; Défourneau, D.; Sangster, M. J. L. *Phys. Rev. B* **1973**, *7*, 2336-2348.
70. Lauhon, L. J.; Ho, W. *Rev. Sci. Instrum.* **2001**, *72*, 216-223.
71. Kastner, M. A. *Physics Today* **1993**, January 24-31.
72. Aviram, A.; Ratner, M. Eds. *Molecular Electronics: Science and Technology, The Annals of the New York Academy of Sciences*; The New York Academy of Sciences: Vol. 852, New York, 1998.
73. Reimers, J.; Picconatto, C.; Ellenbogen, J.; Shashidhar, R, *Molecular Electronics III, The Annals of the New York Academy of Sciences*; The New York Academy of Sciences: Vol. 1006, New York, 2003.

#### Personnel supported

Prof. Mark Reed, PI  
Dr. Takhee Lee (postdoc)  
Dr. Wenyong Wang (graduate student)

#### Publications

##### **Book chapters:**

1. W. Wang, T. Lee, and M.A. Reed, "Electronic Transport Through Self-Assembled Monolayers", *Nanoscale Assembly*, edited by Wilhelm Huck, (Kluwer Academic/Plenum Publishers, 2005).
2. W. Wang, T. Lee, and M.A. Reed, "Intrinsic Electronic Conduction Mechanisms in Self-Assembled Monolayers", *Introducing Molecular Electronics*, Proceedings of the Dresden ADMOL Conference, *Lect. Notes Phys.* **680**, 275-300 (2005).

##### **Journal articles**

1. W. Wang, T. Lee, I. Kretzschmar, and M.A. Reed, "Inelastic Electron Tunneling Spectroscopy of Alkanedithiol Self-Assembled Monolayers", *Nano Lett.* **4**, 643 (2004).
2. Reed, M.A., "Molecular Electronics – Back under control", *Nature Materials* **3**, 286 (2004).
3. Lee, T.; Wang, W.; Klemic, J. F.; Zhang, J. J.; Su, J.; Reed, M. A., "Comparison of Electronic Transport Characterization Methods for Alkanethiol Self-Assembled Monolayers", *J. Phys. Chem. B.* **108**, 8742 (2004).
4. W. Wang, T. Lee, and M.A. Reed, "Elastic and Inelastic Electron Tunneling in Alkane Self-Assembled Monolayers", *J. Phys. Chem. B.* **108**, 18398 (2004). (**cover, feature article**).
5. T. Lee, W. Wang, and M. A. Reed, "Intrinsic Electronic Transport through Alkanedithiol Self-Assembled Monolayer", *J. Jour. Appl. Phys.* **44**, 523 (2005).
6. W. Wang, T. Lee, and M.A. Reed, "Electron Tunneling in Alkane Self-Assembled Monolayers", *Rep. Prog. Phys.* **68**, 523 (2005).
7. T. Lee, W. Wang, J. J. Zhang, J. Su, J. F. Klemic, and M. A. Reed, "Cross-platform characterization of electron tunneling in molecular self-assembled monolayers", *Curr. Appl. Phys.* **5**, 213 (2005).
8. W. Wang, T. Lee, and M.A. Reed, "Electronic Transport in Molecular Self-Assembled Monolayer Devices", *Proc. IEEE* **93** (2005).

#### Interactions/Transitions

**Numerous talk and seminars. No consultations or transitions**

**New discoveries, patents**

**none**

**Addendum: Collaboration with Xia, U. Washington**

Through this DURINT, we obtained samples from Xia et al, to investigate electrical and optical effects. As a result of this collaboration, we had a serendipitous and important discovery.

We have looking at simple approaches for both coupling to propagating plasmon modes and their observation in metallic nanowires. Specifically, our experiment couples to propagating modes in a radially symmetric nanowire by using one end as a scattering center. This scattering center creates an overlap between the incident radiation (focused laser) and the propagating plasmon mode. Focused laser light excites plasmons that propagate along the length of silver nanowires and couple to free space photons, radiating at the ends. Plasmons are also observed to couple between overlapping nanowires and fan-out from one wire into multiple nanowires.

The wires used in this study have a mean diameter of ~100 nm and lengths that vary from 3-20  $\mu\text{m}$ . The nanowires were synthesized in a mixture of ethylene glycol (EG) and poly(vinyl pyrrolidone) (PVP)[1] The wires were washed once in acetone to remove the EG, four times with ethanol to remove the PVP, and once with water. The final aqueous suspension consisted of silver nanowires, a small fraction of silver nanoparticles, and trace amounts of PVP and ethanol. The structure of the nanowires was characterized by transmission electron microscopy (TEM), as seen in Figure 1. The nanowires are observed to have tapered ends (Figure 1A), and are smooth to within the resolution of the TEM micrographs (~1nm ). Additionally, a thin layer of PVP surfactant (2-5 nm) can be resolved in many of the micrographs. An electron diffraction pattern shows that the bulk of the wire is highly crystalline (see Figure 1B) and has face centered cubic (FCC) lattice symmetry.

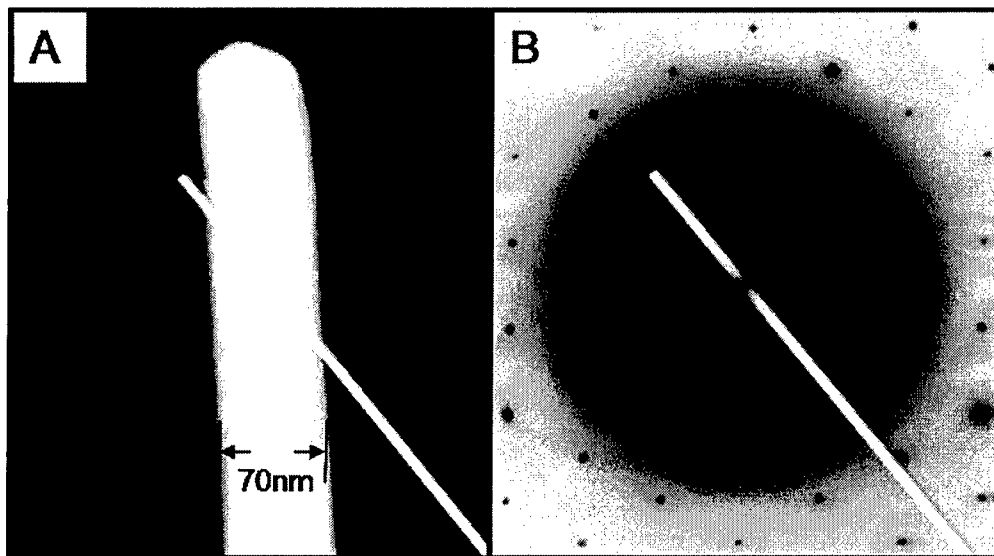


**Figure 1.** Structure of silver nanowires. A) Transmission electron micrograph (TEM) of the silver nanowires. B) Electron diffraction pattern of the same nanowire, showing FCC crystalline structure.

Aqueous nanowire suspensions were deposited on No.1 ½ cover glasses (Corning No. 0211 zinc titania glass) and allowed to dry in open air. Dried nanowires were then mounted on an inverted optical microscope (Nikon Eclipse TE-2000). A 100x oil immersion objective (N.A. = 1.4) lens was used to focus the laser light and to collect a bright field image. The laser illumination was coupled into the microscope via a dichroic mirror that selectively reflects 96% of light at 830nm. The microscope objective focuses the collimated laser light to a diffraction limited spot in its focal plane. Images were collected with either a CCD (Hitachi, 8 bit, 480X640) or a high-speed CMOS (Photron FastCam 1024-PCI), which both received roughly 4% of the light from the sample at the laser frequency (see supporting information). To eliminate the possibility of evanescent waves propagating along the glass surface and preferentially scattering from the tips of the silver nanowires, we immersed all samples with index-matching oil (Nikon Type A immersion oil,  $n=1.515$ ). Even though scattering from the glass surface disappeared, light continued to strongly radiate from the distal end of the nanowire.

We launch plasmons by illuminating an end of a single nanowire with a diffraction limited laser spot as shown in Figure 2. Plasmons can be launched from either end of the nanowire (Figures 2A and 2B); thus, plasmon propagation is reversible. In contrast, plasmon modes are not observed to be launched when the laser is focused on the mid-section of a smooth wire (see Figure 2C and 2D). Since the momentum of the incoming photon ( $k_{\text{photon}}$ ) is not matched to that of the propagating plasmon ( $k_{\text{plasmon}}$ ), there needs to be a scattering mechanism to provide an additional wavevector ( $\Delta k_{\text{scatter}}$ ). At the midsection of the wire, the nanowire is cylindrically symmetric over the extent of the diffraction limited spot, and therefore cannot scatter in the axial direction. However, this symmetry is broken at the tapered end of the nanowire where light is scattered into propagating axial plasmon modes. A similar strategy has been implemented for thin film



surface plasmons utilizing gratings or dots [2] Likewise, propagating plasmon modes incident upon a sharp discontinuity (e.g., the tapered end of the nanowire) can re-emit as photons.

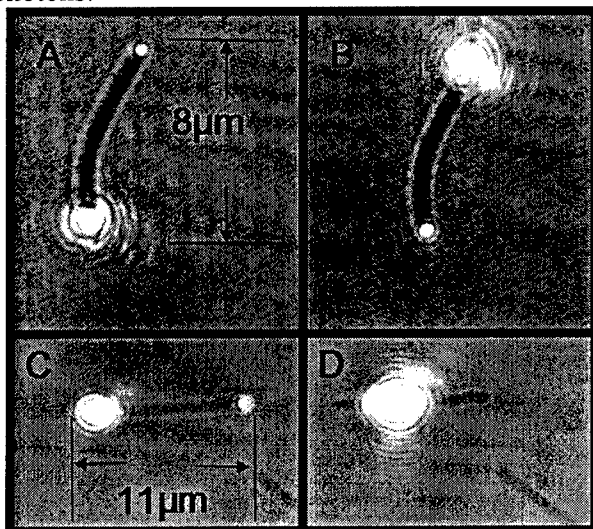


**Figure 2.** Micrographs showing the spatial sensitivity of launching plasmons. A) Nanowire with excitation at the bottom end. B) Same nanowire when excited from top end. C) Nanowire excited at left end. D) Same nanowire with laser positioned at the middle of the nanowire. Notice that the plasmon is not excited in this geometry.

If the symmetry is gently broken over longer length scales, plasmon propagation is unaffected. This can be seen in Figures 2A and 2B, where plasmons propagate around the bend of the nanowire with no observed radiative loss. The smallest naturally occurring optically resolvable bend found in these nanowires is shown in Figure 3A. This nanowire, with a radius of curvature of  $4\mu\text{m}$ , guides plasmons with no observed radiative loss. However, extremely sharp bends in the nanowire will behave like the end of nanowires, scattering propagating plasmons into photons. This effect is demonstrated in Figure 3B, where a nanowire shows emission at two “kinks” (radius of curvature below the diffraction limit). The kinks are spontaneous defects that form during the growth process, and occur in a small fraction of wires. Scanning electron micrographs reveal that typical kinks are discontinuities in the wire direction. Figure 3C is representative of the structure of these kinks; i.e., sharp interior angles and flat exterior faces, with characteristic size  $\sim 100\text{nm}$ .

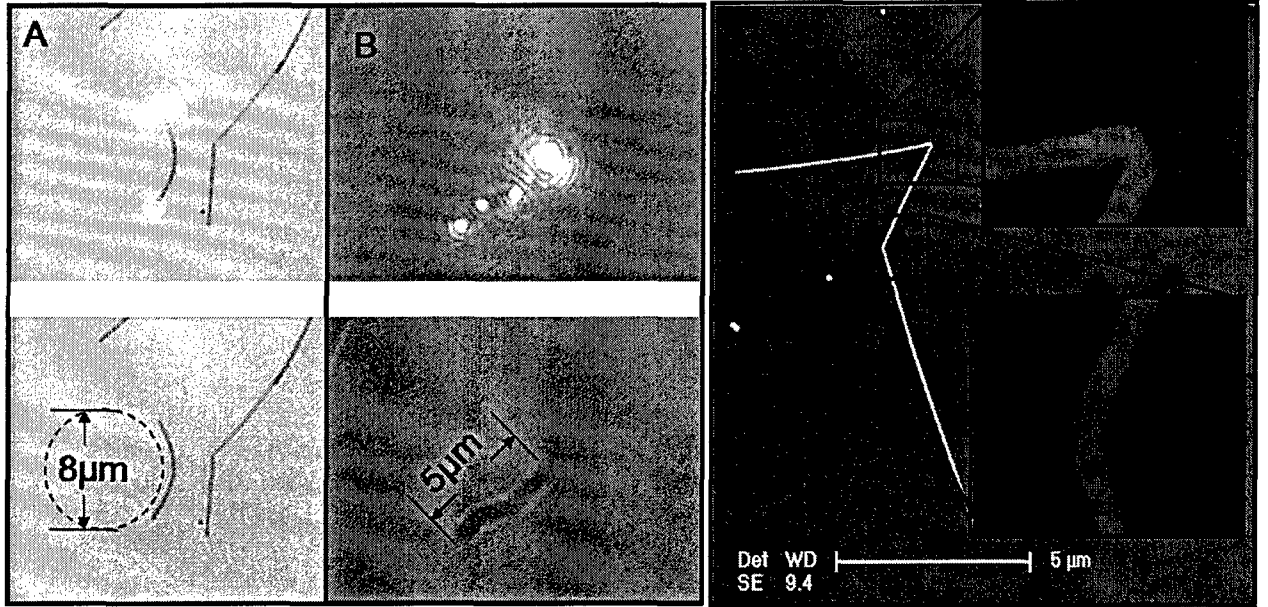


**Figure 3.** Micrographs of plasmon propagation in silver nanowires and emission (top), control with no laser excitation (bottom). Brightest point in image is scattering from incident beam. A) A 7 $\mu\text{m}$  wire (excitation top) with a radius of curvature of 4 $\mu\text{m}$ , a wire not radiating is in close proximity. Inset is a circle of radius of 4 $\mu\text{m}$  for comparison. B) A 5 $\mu\text{m}$  wire (excitation top right) with both the opposite end and two additional points of high curvature that radiate (radius of curvature less than the diffraction limit.) C) An electron micrograph of a typical wire with kinks, with insets of increased magnification.

A nanowire with multiple kinks can be used to estimate the plasmon propagation length. Each kink is used dually as a plasmon launching site and photon radiating site. We sequentially irradiate each kink and measure the radiated intensity from all the other kinks, as illustrated in Figure 4A. We find that the radiated intensity is strongly correlated to the distance between points along the nanowire, as shown in Figure 4B.

These data are well described by an exponential decay,  $I(x) = I_0 e^{-\frac{x}{L}}$ , with a characteristic length of  $L = 3 \pm 1 \mu\text{m}$ . If one makes the assumptions that i) the photon-plasmon coupling strengths are the same at each junction, and that ii) radiative losses (at kinks) are insignificant compared to dissipative losses (along the nanowire length), then  $L$  represents the plasmon propagation length. Even when these assumptions are not true, this simple far-field measurement provides a practical lower limit for the propagation length.

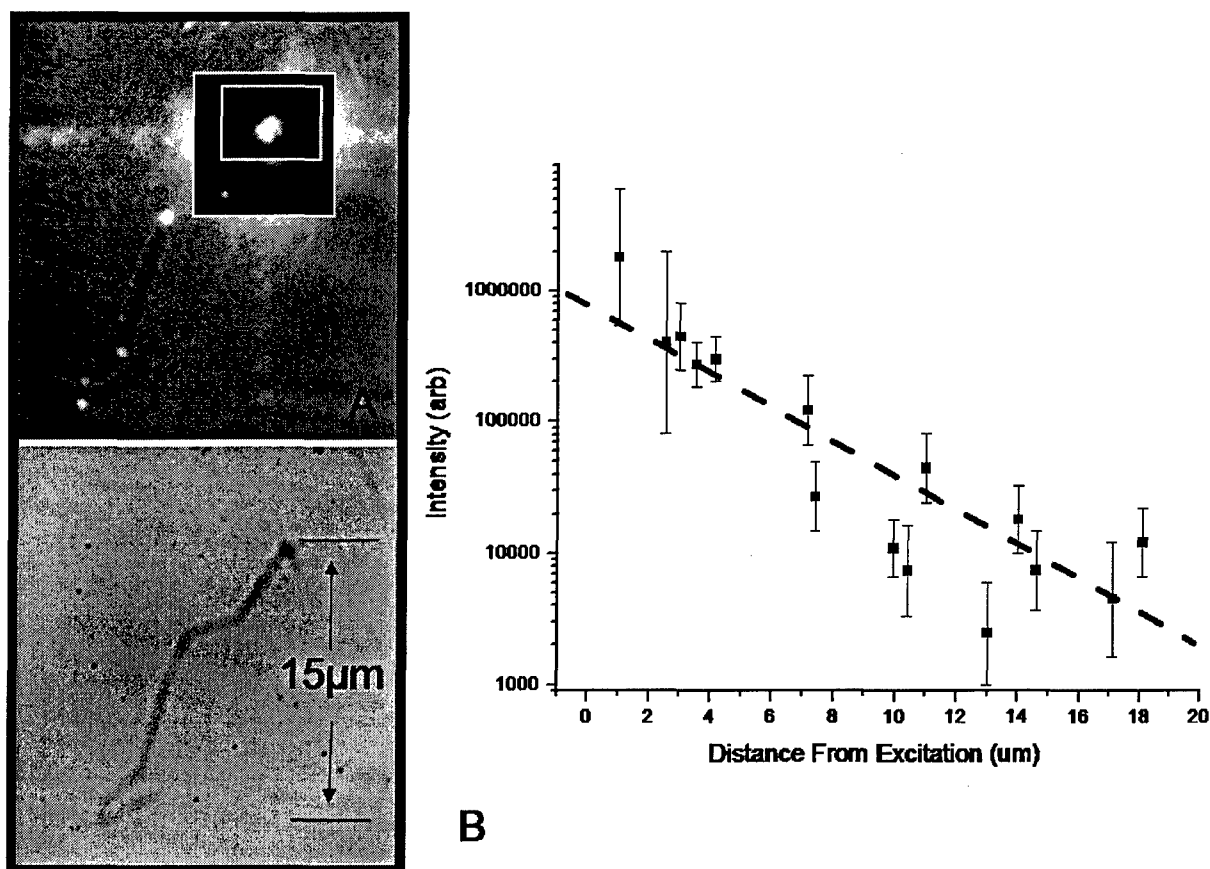


**Figure 4.** A) Micrographs of plasmon propagation in a silver nanowire with multiple emission points (top) control with no laser excitation (bottom). Camera shutter speed and laser intensity were varied to increase total dynamic range. The unsaturated images of the excitation and brightest emission points at shorter exposure times (high shutter speeds) are overlaid for clarity. B) Semi-log plot of intensity versus distance from excitation source. The dashed line is a fit of the data to an exponential. Six distinct points were probed (15 unique combinations). The uncertainty is arrived at by taking the standard deviation of all exposures with unsaturated pixels.

Propagating modes are also seen to couple between overlapping nanowires. In Figure 5 we present an image and an intensity profile from three overlapping nanowires, which form naturally during solvent evaporation. When one of these nanowires is excited, two observations are seen. First, visible radiation is emitted at the intersection of the overlapping nanowires. Second, visible radiation is emitted at the ends of nanowires that overlap the illuminated nanowire. This is reminiscent of the interwire coupling seen in sub-wavelength silica and semiconductor nanowire. While coupling for dielectric guides decreases with increasing diameter since less energy is available in the evanescent wave, metallic nanowire coupling should not have this diameter dependence since plasmons remain confined to the surface.

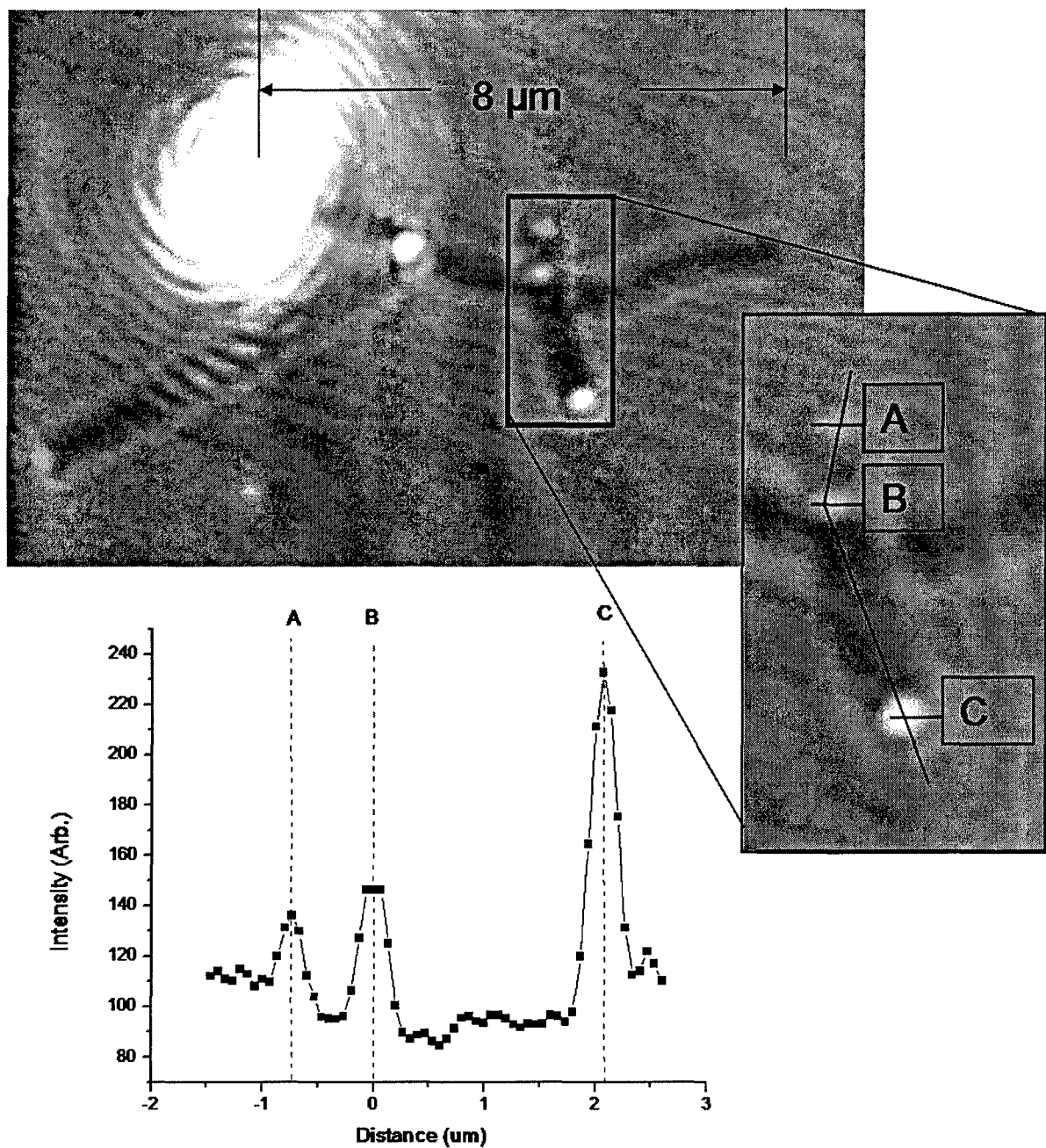


**Figure 5.** Group of overlaying nanowires that illustrates inter-wire plasmon coupling. The excitation at the far left nanowire end produces reemission at both the nanowire junctions and reemission from the coupled nanowires as well. The inset shows an intensity line cut showing the reemission intensity profile along wire.

In conclusion, we demonstrate the selective launch and propagation of plasmons along silver nanowires using a simple far-field excitation and detection method. We have also observed that these propagating plasmon modes can couple between adjacent

nanowires. The phenomena are not specific to nanowire material or excitation wavelength – we have observed similar results in gold and copper nanowires. Technological applications require the positioning of nanowires into a deterministic network which can be accomplished by a variety of methods, such as flow alignment<sup>17</sup>, biologically derived templates<sup>18</sup>, dielectrophoretic alignment<sup>19</sup> or holographic optical tweezers<sup>20,21</sup>. The current study represents a new approach in the observation and manipulation of plasmons in nanoscale structures.

1. Sun, Y.; Yin, Y.; Mayers, B. T.; Herricks, T.; Xia, Y. *Chemistry of Materials* **2002**, *14*, 4736-4745.
2. Ditlbacher, H.; Krenn, J. R.; Schider, G.; Leitner, A.; Aussenegg, F. R. *Applied Physics Letters* **2002**, *81*, 1762.

# HOLOGRAPHIC INTERFERENCE LITHOGRAPHY

## FOR PHOTONIC AND PHONONIC CRYSTALS

Chaitanya Ullal and Edwin Thomas

Our broad goal of this area of the DURINT is the use of holographic interference lithography for the fabrication of two-dimensional periodic and three dimensional periodic bicontinuous structures. Previously, work in this area had concentrated on the establishment of symmetries, the application of these structures as photonic crystals, and as microlenses. The research work over the past review period has built on these efforts and also introduced some new thrust areas. The recent work has been in three areas:

1. Photonic Crystals:
  - a. Development and fabrication of architectures relevant to on chip photonic crystals
  - b. Writing of defects using 2-photon lithography. (collaboration with SUNY-Buffalo)
  - c. Development of characterization for specific 3d bicontinuous structures (collaboration with WPAFB)
2. 2D holographic patterns as phase masks.
3. Phononic crystals: development of a complete tool set for the study of hypersonic phononic crystals

### 1. HOLOGRAPHIC INTERFERENCE LITHOGRAPHY FOR PHOTONIC CRYSTALS

In previous work in this DURINT we had examined the effect of symmetries on the photonic band gap for various structures. We had found that structures with simple low Fourier terms tend to support gaps. This work subsequently led to a deeper, more physical insight, by viewing these low Fourier term structures as possessing "dielectric mirrors" in principal directions. In order to arrive at experimentally *fabricable* structures that support band gaps, we restricted ourselves to structures that have sinusoidal modulations in real space that are along reciprocal lattice vectors that are the closest to the origin. We were thus, interested in targeting three such structures: viz. the level set approximations to the Schwartz Simple Cubic (P), Gyroid (G), and Diamond (D). As previously demonstrated these structures are theoretically accessible. However from the point of view of their use as structures to be made on chip, given the opacity of the substrate, we required all the interfering beams to come from the same half space. In order to negotiate this consideration we derived approximations to these structures that retained some of the sinusoidal band gap supporting terms while also being amenable to fabrication. We demonstrated that the level set approximation to the P structure, the 3-FCC-term and 3-BCC-term structures were three such structures. Importantly the 3-FCC-term structure displayed two gaps and the P structure is scalable in terms of unit cell size, for any fixed writing

wavelength. These two structures were then successfully fabricated in an epoxy based negative photoresist.

A more recent area of thrust in terms of photonic crystals has been the controlled introduction of defects via two-photon lithography. In order to introduce defects into the photonic crystal structures being written by interference lithography we add a step to the fabrication procedure. Once the photoresist has been exposed to the interference pattern the sample is taken over to a two-photon direct writing setup. Defects are written into the photoresist by scanning the focal point of an infra red laser beam into the volume of the photoresist. The photoresist is then subjected to the previously established processing steps, viz. post exposure baking, developing and supercritical drying. The net pattern is the sum of both the defects and the large area single crystalline interference lithography pattern. Preliminary results are shown in Figure 1. This work is being done as a collaborative effort between the Thomas group at MIT and the Prasad Group at SUNY-Buffalo.

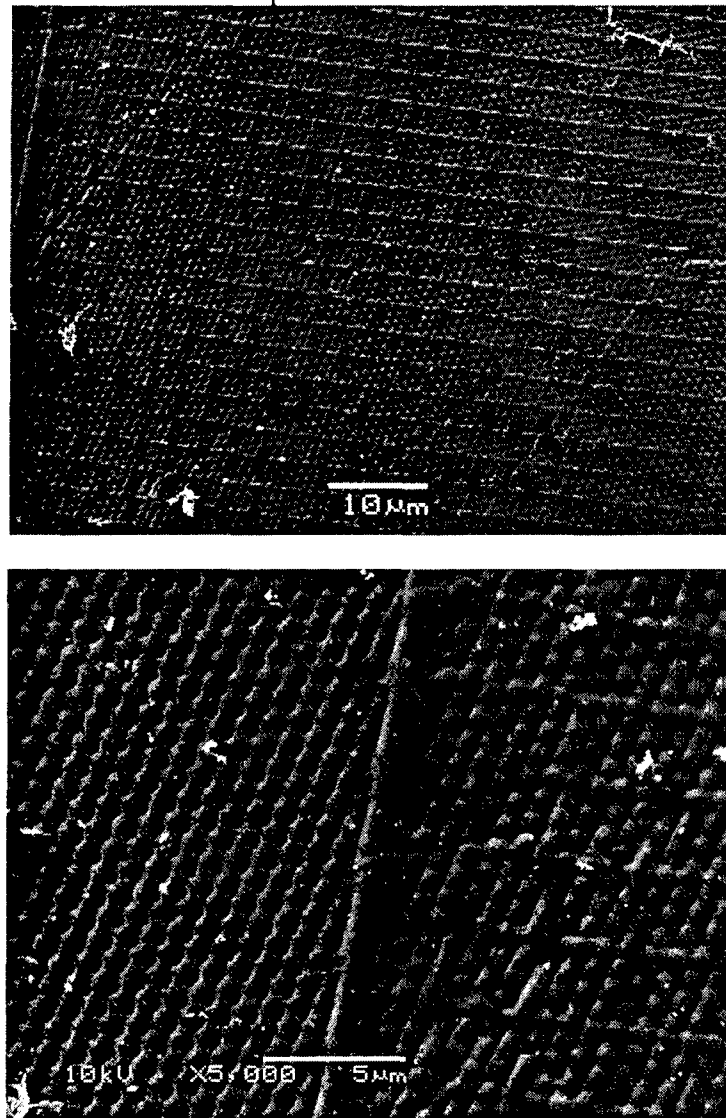


**Figure 1** (a) Defects in large area and (b) defects and structure. The 3D structure is created by

An important area of interest in the fabrication of three dimensional structures via holographic interference lithography is the development of a non destructive characterization technique in the estimation of volume fraction. This is particularly important in the case of photonic crystals since the photonic band gaps are strongly dependent on the volume fraction of the structures. We are currently developing a technique based on diffraction to determine volume fraction of particular structure. This involves the transfer of interference patterns into h-pdlc materials and the subsequent characterization of these materials via diffraction. This work is being done in collaboration with the Bunning group at WPAFB.

## 2. 2D holographic lithographic microlens patterns as phase masks.

In previous work under this DURINT we had examined the potential for using 2d holographic patterns to create biomimetic microlenses. These lenses were further shown to behave as microfluidic elements with integrated pores. We also extended the use of these biomimetic patterns by demonstrating their application as multipattern photomasks; that is, by using the same photomask and simply adjusting (i) the illumination dose, (ii) the distance between the mask and the photoresist film, and (iii) the tone of photoresist, we were able to create a variety of different microscale patterns with controlled sizes, geometries, and symmetries that originated from the lenses, clear windows, or their combination (See Figure 2). Light field calculations were made and found to be close to the experimental results.

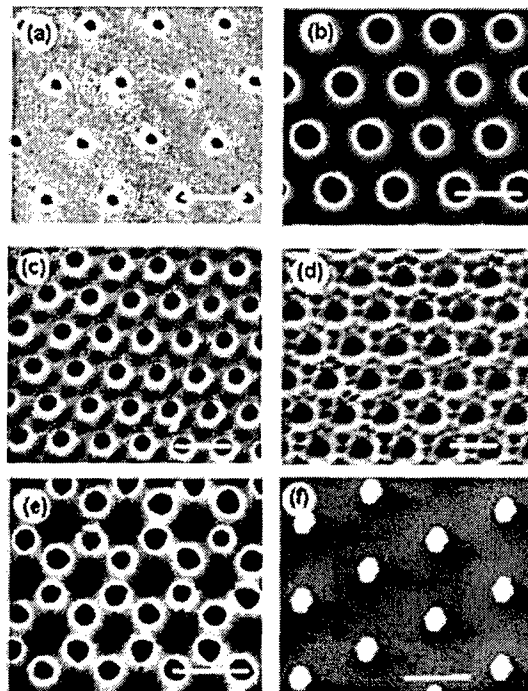
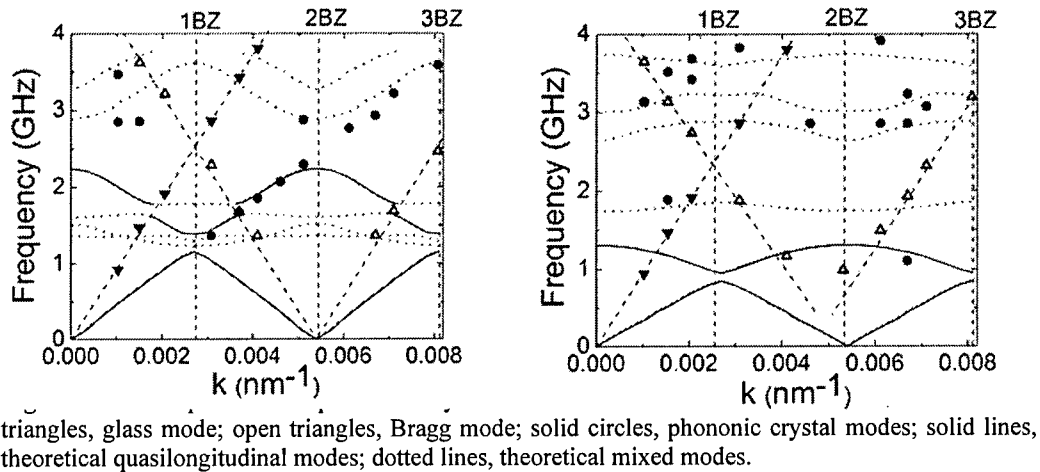


**Figure 2** (a) (b) (c) (d) (e) (f) The patterns are created by using the same photomask and adjusting the illumination dose, the distance between the mask and the photoresist, and the tone of photoresist. (a)



### 3. Hypersonic Phononic crystals.

A new thrust area with this DURINT in the area of holographic structures has been the study of hypersonic phononic crystals. To date the focus of the research in this area has been in the application of the holographic structures as photonic crystals. This is based on the fact that we have periodicities that are on the length scale of visible light. We proposed and demonstrated the use of hypersonic phononic crystals in the control of emission and propagation of high frequency phonons. We reported the fabrication of high quality, single crystalline hypersonic crystals using interference lithography and showed that direct measurement of their phononic band structure (See Figure 3) is possible with Brillouin light scattering. Numerical calculations were employed to explain the nature of the observed propagation modes. This work lays the foundation for experimental studies of hypersonic crystals and, more generally, phonon-dependent processes in nanostructures.



## **POLYMERIC PHOTONIC CRYSTALS FOR LOW-THRESHOLD PHOTONIC BANDGAP LASING**

Jongseung Yoon, Wonmok Lee and Edwin L. Thomas

The objective of this area of the DURINT is the use of polymeric photonic bandgap structures for fabricating low-threshold photonic bandgap laser devices. We pursued the development of defect-mode one-dimensional (1D) photonic bandgap lasers by two different approaches: (1) block copolymer self-assembly and (2) polymer/inorganic nanoparticle hybrid layer-by-layer assembly.

### **1. Optically Pumped Surface-Emitting Lasing using Self-Assembled Block Copolymer Distributed Bragg Reflectors**

With an appropriate domain size that is comparable to optical wavelengths, block copolymers can be used to create periodic dielectric structures which can interact with visible light, i.e. photonic crystals. Over the past years, block copolymers have been considered as a unique materials platform for fabricating large-area, well-ordered photonic bandgap structures. One potential application of such self-assembled polymeric photonic crystals is to use them as a resonator in a photonic microcavity to provide spectrally-selective feedback for lasing. In this work, we fabricated a thin film organic laser cavity using a block copolymer based one-dimensional 1D photonic crystal. Polymeric distributed Bragg reflectors (DBRs) were prepared through the self-assembly of a lamellar-forming poly(styrene-*b*-isoprene) (PS-*b*-PI) diblock copolymer having a 1D photonic stop band overlapping with the fluorescence spectrum of a gain medium. Optically pumped surface-emitting lasing was obtained using polymethylmethacrylate (PMMA) doped with 1,4-di-(2-methylstyryl)benzene (Bis-MSB) as an organic gain medium and the polymeric self-assembled DBR as a spectral-band selective feedback elements (See Figures 4, 5, 6). This block copolymer based photonic structure opens the possibility for creating all-organic, flexible, and self-assembled active photonic devices with fast and low-cost processing, and spectral tunability by various external fields.

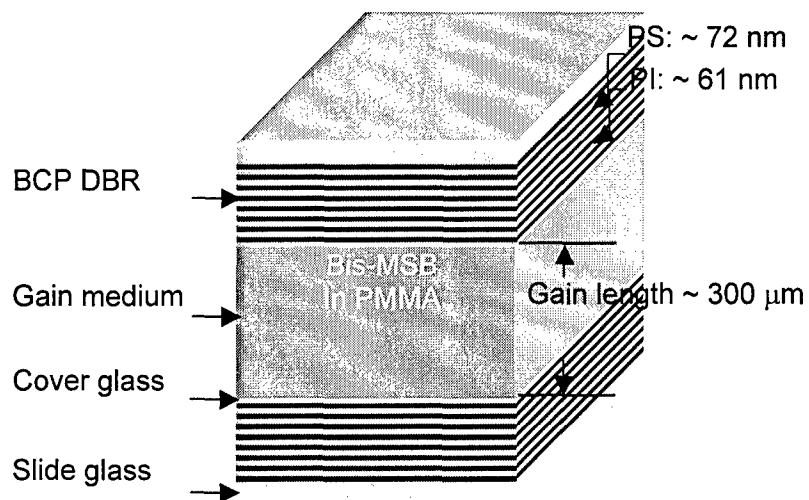


**Figure 4.** Schematic of the block copolymer based laser cavity, comprised of a gain medium, Bis-MSB and PMMA, enclosed between two block copolymer based distributed Bragg reflectors. The thicknesses of PS and PI domains are estimated values at 10 wt % solvent concentration based on the peak position and FWHM of the reflectivity spectrum.

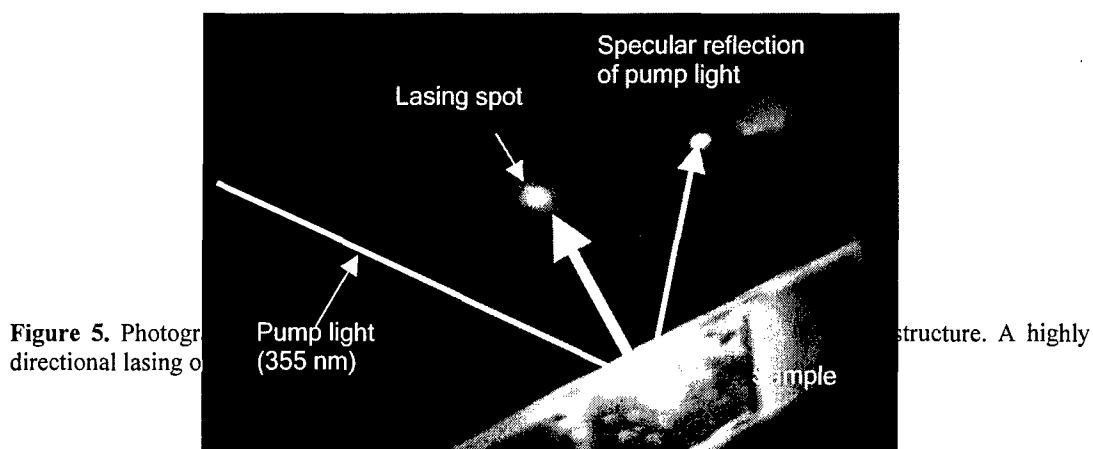


**Figure 5.** Photograph of directional lasing from the sample.

structure. A highly

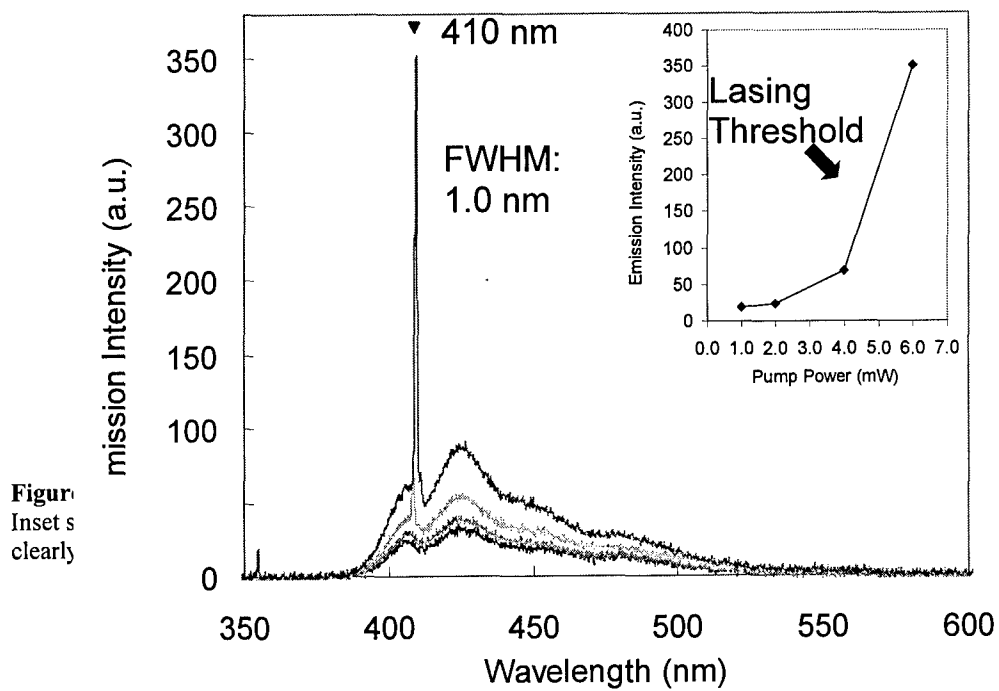
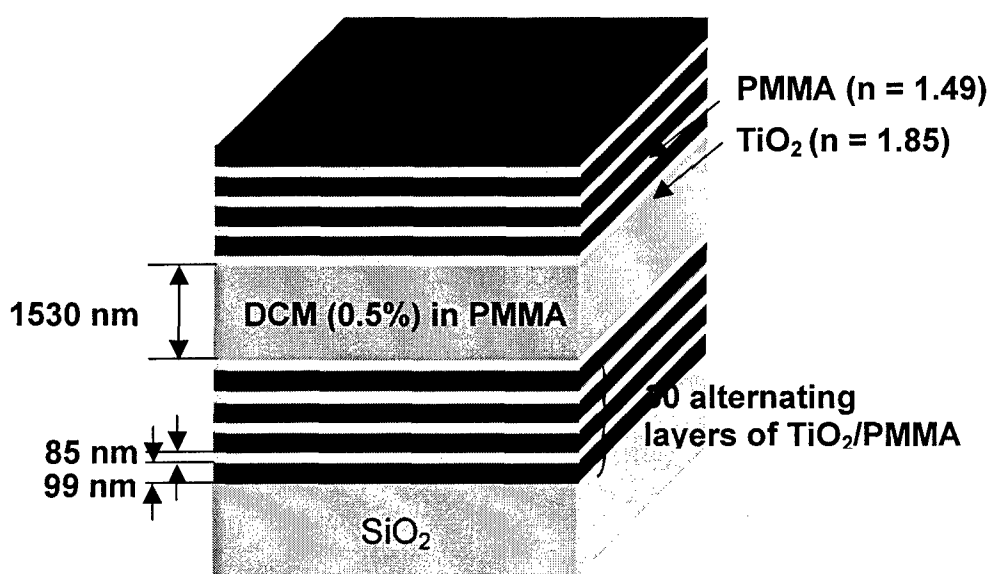


Figure  
Inset s  
clearly

1.  
h

## 2. Defect-mode Mirrorless Lasing in Dye-doped Organic/Inorganic Hybrid 1D Photonic Crystal

We developed a novel dye-doped organic/inorganic hybrid 1D photonic crystal containing a dye-doped defect layer for defect-mode photonic bandgap lasing. The multilayer laser structure consists of alternating layers of titania ( $\text{TiO}_2$ ) nanoparticles and polymethylmethacrylate (PMMA) with an active emission layer of organic dyes (DCM) in PMMA (See Figures 7,8,9). Low threshold lasing has been demonstrated at a single defect-mode wavelength of the 1D photonic bandgap structure resulting from the inhibited density of states of photons within the stop band and the enhanced rates of spontaneous emission at the localized resonant defect mode. This work has been done as a collaborative effort between the Thomas group at MIT and the Prasad Group at SUNY-Buffalo.



**Figure 7.** Schematic of dye-doped defect-mode 1D photonic crystal, glass-(PMMA- $\text{TiO}_2$ )<sup>15</sup>-(DCM/PMMA)-(TiO<sub>2</sub>-PMMA)<sup>15</sup>-air.

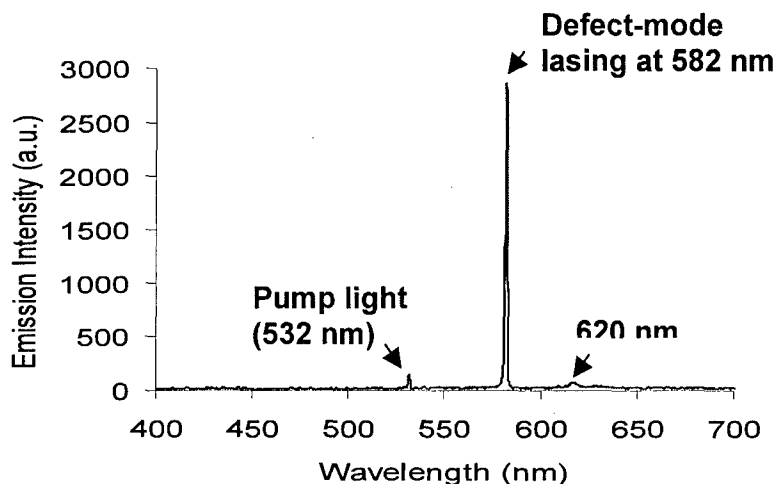


**Figure 8.** The lasing spectrum obtained at a pump power of 1 mW, above the lasing threshold. The two small peaks beside the lasing line at 582 nm correspond to the excitation light (532 nm) and to the low frequency defect mode (at 620 nm, below its lasing threshold for this pump power).

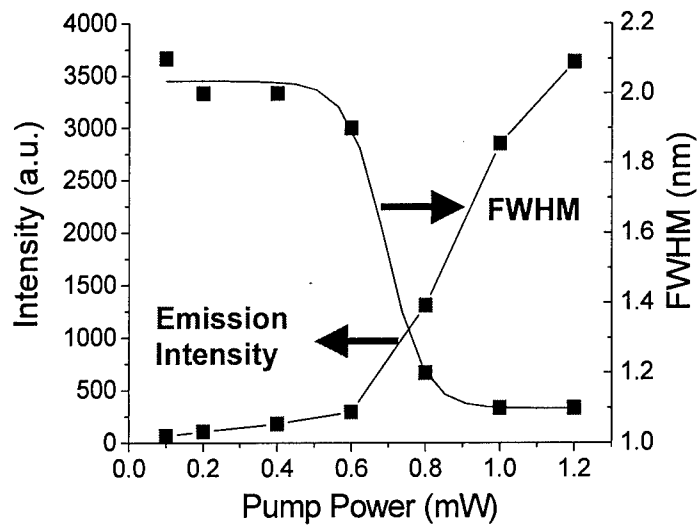


**Figure 9.** Emission intensity and line-width (the full width at half maximum, FWHM) at the lasing wavelength (582 nm) as a function of pump power. The behavior of the intensity and the FWHM clearly demonstrate a threshold for lasing around 0.6 mW pump power (12  $\mu$ J pulse energy).